A Geodynamic Investigation of Continental Rifting and Mantle Rheology: Madagascar and East African Rift case studies

Tahiry Andriantsoa Rajaonarison

Dissertation submitted to the Faculty of the
Virginia Polytechnic Institute and State University
in partial fulfillment of the requirements for the degree of

Doctor of Philosophy
in
Geosciences

D. Stamps, Chair
Scott King
Ying Zhou
Andrew Nyblade

December 2, 2020
Blacksburg, Virginia

Keywords: Asthenospheric flow, edge-driven convection, mantle wind modeling, Lattice Preferred Orientation, seismic anisotropy, dislocation creep rheology, 3D thermo-mechanical modeling, lithospheric buoyancy forces, ∼E-W extension across East Africa, horizontal mantle tractions, African Superplume

A Geodynamic Investigation of Continental Rifting and Mantle Rheology: Madagascar and East African Rift case studies

Tahiry Andriantsoa Rajaonarison

(ABSTRACT)

Continental rifting is an important geodynamic process during which the Earth's outermost rigid shell undergoes continuous stretching resulting in continental break-up and the formation of new oceanic basins. The East African Rift System, which has two continental segments comprising largely of the East African Rift (EAR) to the West and the easternmost segment Madagascar, is the largest narrow rift on Earth. However, the driving mechanisms of continental rifting remain poorly understood due to a lack of numerical infrastructure to simulate rifting, the lack of knowledge of the underlying mantle dynamics, and poor knowledge of mantle rheology. Here, we use state-of-art computational modeling of the upper 660 km of the Earth to: 1) provide a better understanding of mantle flow patterns and the mantle rheology beneath Madagascar, 2) to elucidate the main driving forces of observed present-day ∼E-W opening in the EAR, and 3) to investigate the role of multiple plumes or a superplume in driving surface deformation in the EAR. In chapter 1, we simulate Edge Driven convection (EDC), constrained by a lithospheric thickness model beneath Madagascar. The mantle flow associated with the EDC is used to calculate induced olivine aggregates' Lattice Preferred Orientation (LPO), known as seismic anisotropy. The predicted LPO is then used to calculate synthetic seismic anisotropy, which were compared with observations across the island. Through a series of comparisons, we found that asthenospheric flow resulting from undulations in lithospheric thickness variations is the dominant source of the seismic anisotropy, but fossilized structures from an ancient shear zone may play a role in southern Madagascar. Our results suggest that the rheological conditions needed for the formation

of seismic anisotropy, dislocation creep, dominates the upper asthenosphere beneath Madagascar and likely other continental regions. In chapter 2, we use a 3D numerical model of the lithosphere-asthenosphere system to simulate instantaneous lithospheric deformation in the EAR and surroundings. We test the hypothesis that the ∼E-W extension of the EAR is driven by large scale forces arising from topography and internal density gradients, known as lithospheric buoyancy forces. We calculate surface deformation solely driven by lithospheric buoyancy forces and compare them with surface velocity observations. The lithospheric buoyancy forces are implemented by imposing observed topography at the model surface and lateral density variations in the crust and mantle down to a compensation depth of 100 km. Our results indicate that the large-scale ∼E-W extension across East Africa is driven by lithospheric buoyancy forces, but not along-rift surface motions in deforming zones. In chapter 3, we test the hypothesis that the anomalous northward rift-parallel deformation observed in the deforming zones of the EAR is driven by viscous coupling between the lithosphere and deep upwelling mantle material, known as a superplume, flowing northward. We test two end-member plume models including a multiple plumes model simulated using high resolution shear wave tomography-derived thermal anomaly and a superplume model (African superplume) simulated by imposing a northward mantle-wind on the multiple plumes model. Our results suggest that the horizontal tractions from northward mantle flow associated with the African Superplume is needed to explain observations of rift-parallel surface motions in deforming zones from GNSS/GPS data and northward oriented seismic anisotropy beneath the EAR. Overall, this work yields a better understanding of the geodynamics of Africa.

A Geodynamic Investigation of Continental Rifting and Mantle Rheology: Madagascar and East African Rift case studies

Tahiry Andriantsoa Rajaonarison

(GENERAL AUDIENCE ABSTRACT)

Continental rifting is an important geodynamic process during which the Earth's outermost rigid, known as lithosphere, undergoes continuous stretching resulting in continental break-up and the formation of new oceanic basins. What tectonic forces drive continental rifting is an outstanding question of geophysics. In continental regions far from subduction zones, there are two major tectonic forces: lithospheric buoyancy forces that arise from high topography and density variations and basal shear drag which arise from mantle convection interacting with the lithosphere. The understanding of the driving forces of continental rifting has been limited due to lack of computer modeling capabilities and lack of knowledge of the rheology of the Earth's mantle. In this work done during my PhD studies, I use advanced 3D computer simulation to investigate the driving forces of the East African Rift, the largest narrow rift on Earth, and the mantle convection pattern beneath the nearby island, Madagascar. Mantle convection is mostly characterized by seismologist using a proxy know as seismic anisotropy, which indicate mantle flow direction but can also indicate paste tectonic deformation. In chapter one, we tested the hypothesis that observed seismic anisotropy across the continental island arises from asthenospheric flow drive by variations in lithospheric thickness. We simulated 3D small scale convection driven by lithospheric thickness variations beneath Madagascar and calculated synthetic seismic anisotropy. Comparison of calculated with measured seismic anisotropy reveal that asthenospheric flow resulting from undulations in lithospheric thickness is the dominant source of the seismic anisotropy in Madagascar. In chapter 2, we simulated 3D regional scale lithospheric deformation to investigate the role of lithospheric buoyancy forces in driving the E-W extension of East

Africa. By incorporating observed high resolution surface topography and crustal density model in our model, we found that East Africa is extending in E-W direction because of the topography gradient high associated with the high topography of East Africa and the low topography at the oceanic basin to the East. However, the lithospheric buoyancy due to the topography gradient cannot explain the observed rift parallel deformation. In chapter 3, we investigate the role of mantle plume in driving the rift parallel deformation in East Africa. We test two end-member mantle plume model: a multiple plume model and a superplume model. We find that the anomalous rift parallel motion in the East African Rift may be driven by the underlying mantle flow associated with the African superplume. Overall, this study provides better understanding of continental rifting in East Africa.

Acknowledgments

It is for me an honor to have been the first PhD recruit of Dr. Sarah Stamps and obtain my PhD degree, as a Malagasy student, at Virginia Tech. Few years ago, I would have never imaging myself pursuing a doctorate study in an US institution knowing all the obstacles and barriers that I would face. Yet, when I first met Dr. Stamps in 2012, during a GPS campaign in Madagascar, I felt that she believe in my potential and she has made immeasurable efforts to get me in the US to study. I would like to address my sincere gratitude to Dr. Stamps for the support, guidance, and mentorship throughout my entire graduate studies (Msc and PhD). Dr. Stamps has taught me everything, yes everything in science, from using a computer to modern state-of-art numerical modeling to become an excellent researcher. Dr. Stamps's leadership skills, determination, hard work, generosity, and professionalism have inspired me to follow a similar path for my future career. I would like to thank the entire Geodesy and Tectonophysics Laboratory (GTL) group, lead by Dr. Stamps, a diverse and inclusive environment, for providing me a wonderful and unique PhD experience. A special thanks to my committee members, Dr. Scott King, Dr. Ying Zhou, and Dr. Andrew Nyblade because their support, advice, and counsel have been key to the success of my PhD. A huge thanks to Dr. John Naliboff who was my mentor during the last few years of my PhD, and who also contributed to the last two projects with his expertise in numerical modeling of continental rifting. I am delighted to have had worked with my graduate colleagues and friends at the GTL: Emmanuel Njinju, Josh Jones, Jessica Schobelock, and Karen Williams who have always helped to accomodate my life in the USA. This PhD would not have been achieved without the sacrifices, support, encouragement, and thoughtfulness of my wonderful wife Mamitiana. Despite being miles away from me, she has made me feel not alone and

loved. Mamitiana, I love you. I would like to dedicate this doctoral degree to my son, Ashton, who is my main source of inspiration and who is simply our happiness. Ashton, I hope that when you read this, it will make you believe that you can achieve everything you want to. I have to thank my mom Razafiarivony Honorine and my dad Rajaonarison Florent, for the life and opportunities they have given me. A special thank you to my siblings Rado, John, Nadia, Anthony, and Avoniaina for all the sacrifices they have done for me to achieve my dream. Thank you also to all my family.

Contents

List of Figures

List of Tables

Chapter 1

Numerical Modeling of Mantle Flow Beneath Madagascar to Constrain Upper Mantle Rheology Beneath Continental Regions

Published in Journal of Geophysical Research in 2020, with co-authors: D. Sarah Stamps (Virginia Tech), Stewart Fishwick (University of Leicester), Sascha Brune (GFZ German Research of Geosciences and University of Potsdam), Anne Glerum (GFZ German Research of Geosciences), and Jiashun Hu (California Institute of Technology)

Over the past few decades, azimuthal seismic anisotropy measurements have been widely used proxy to study past and present-day deformation of the lithosphere and to characterize convection in the mantle. Beneath continental regions, distinguishing between shallow and deep sources of anisotropy remains difficult due to poor depth constraints of measurements and a lack of regional-scale geodynamic modeling. Here, we constrain the sources of seismic anisotropy beneath Madagascar where a complex pattern cannot be explained by a single process such as absolute plate motion, global mantle flow, or geology. We test the hypotheses that either Edge-Driven Convection (EDC) or mantle flow derived from mantle

wind interactions with lithospheric topography is the dominant source of anisotropy beneath Madagascar. We, therefore, simulate two sets of mantle convection models using regional-scale 3D computational modeling. We then calculate olive aggregates' Lattice Preferred Orientation that develop along pathlines of the mantle flow models and use them to calculate synthetic splitting parameters. Comparison of predicted with observed seismic anisotropy shows a good fit in northern and southern Madagascar for the EDC model, but the mantle wind case only fits well in northern Madagascar. This result suggests the dominant control of the measured anisotropy may be from EDC, but the role of localized fossil anisotropy in narrow shear zones cannot be ruled out in southern Madagascar. Our results suggests that the asthenosphere beneath northern and southern Madagascar is dominated by dislocation creep. Dislocation creep rheology may be dominant in the upper asthenosphere beneath other regions of continental lithosphere.

1.1 Introduction

The character of mantle convection with respect to flow patterns and rheological composition, particularly in the asthenosphere, remains open to debate varying from locally induced flow to models where global flow dominates (Moucha and Forte, 2011; Schuberth et al., 2009). Locally, one model for inducing small-scale convection in the asthenosphere can be driven by significant variations in lithospheric thickness known as edge-driven convection (EDC) (i.e. King and Anderson, 1995, 1998). The model of EDC assumes a thermomechanical lithosphere such that the lithosphere-asthenospheric boundary (LAB) is in thermal equilibrium. Variations in lithospheric thickness then induce thermal instabilities capable of driving asthenospheric flow. Characterizing EDC has been limited to 2D modeling (e.g. Ballmer et al., 2015; Kaislaniemi and van Hunen, 2014) due to limitations in computational

capabilities, yet newer finite element methods (Bangerth et al., 2018a,b; Heister et al., 2017; Ramsay and Pysklywec, 2011; Rose et al., 2017) have made it possible to model 3D regional mantle flow driven by lateral variations in lithospheric thickness.

Azimuthal seismic anisotropy is a commonly used proxy to characterize the patterns of convective motions of the Earth's interior (e.g. Long and Becker, 2010; Savage, 1999; Silver and Chan, 1991) although it cannot exclusively be associated with mantle flow. Some of the major contributers of seismic anisotropy may arise from 1) weaknesses in the crust (Nishizawa and Kanagawa, 2010), 2) melt lenses (Kendall, 1994), and/or fossil anisotropy (e.g. Silver and Chan, 1991) among other sources, and 3) the alignment of olivine minerals in the upper mantle governed by dislocation creep (Karato and Wu, 1993). Anisotropy in the crust can be from shallow sources due to the alignment of sheet silicates (e.g. Nishizawa and Kanagawa, 2010), faults, cracks, and microcracks in the upper 10-15 km (e.g. Kaneshima et al., 1988). Fossil anisotropy is crystallographic fabric preserved in the crust and/or lithospheric mantle imprinted by past or present-day orogenic processes (e.g. Silver and Chan, 1988; Tian and Santosh, 2015). In the upper mantle, mineral crystal aggregates (dominantly olivine) that are subject to dislocation creep align in the direction of mantle flow and the accumulated strain (Podolefsky et al., 2004). The resulting anisotropic fabrics are known as lattice preferred orientation (LPO) and are commonly mapped using a technique called SKS splitting.

Although the depth resolution of shear wave splitting measurements is poorly constrained, in non-volcanic regions the potential sources reduce to pre-existing weaknesses in the crust, fossil anisotropy and mantle flow. In the simplified setting beneath oceanic lithosphere, seismic anisotropy may be caused by absolute plate motions (Beghein et al., 2014) or asthenospheric flow (Becker et al., 2014). However, limitations arise when interpreting seismic anisotropy in continental regions due to a lack of knowledge about subcontinental rheology and limited information on subcontinental mantle flow patterns.

Madagascar (Figure 1.1) is an ideal natural laboratory to study the sources of anisotropy beneath continental regions and the rheological implications for the lithosphere-asthenosphere system because 1) active volcanism is minimal or absent across most of the continental island, thus limiting the effect of melt lenses (Michon, 2016), 2) there are well-exposed tectonic fabrics for comparison (Collins and Windley, 2002; Schreurs et al., 2010), and 3) numerous geological and geophysical observations provide evidence of present-day tectonic activities potentially linked to viscous coupling to asthenospheric flow (Bertil and Regnoult, 1998; Kusky et al., 2010; Rambolamanana et al., 1997; Rindraharisaona et al., 2013).

Reiss et al. (2016) produced the first SKS splitting observations along the SELASOMA seismic profile (SEismological signatures in the Lithosphere/Asthenosphere System Of Southern Madagascar) that spans southern Madagascar in a NE-SW orientation, while Ramirez et al. (2018) provided additional SKS splitting measurements across the entire continental island (Figure 1.1). Azimuthal seismic anisotropy across Madagascar is quite complex. Along the SELASOMA profile, anisotropy varies from a NW-SE direction in the center of the profile to a SW-NE direction along its eastern and western sections (Figure 1.1, yellow bars). Reiss et al. (2016) interpret seismic anisotropy in the central part of the profile as sourced from the lithosphere in association with Precambrian ductile deformation at an existing narrow Ranotsara shear zone (see Figure 1.1) that strikes ∼NW-SE. In contrast, they attribute the SW-NE oriented observations to asthenospheric flow induced by absolute plate motion. Ramirez et al. (2018) suggest asthenospheric upwelling related to the African superplume explains the homogeneous pattern of seismic anisotropy in northern Madagascar (Figure 1.1 red bars), but they suggest the complex pattern of anisotropy in central Madagascar is due to asthenospheric upwelling driven by delamination of the Malagasy lithosphere. Ramirez et al. (2018) also suggest that, since the observed anisotropy cannot be attributed to a single process such as absolute plate motion, the most likely source of the anisotropy is strain-induced

LPO due to small-scale convective flow, which is poorly understood beneath Madagascar and surroundings.

In this work, we characterize EDC beneath Madagascar and investigate its contribution to the observed seismic anisotropy patterns to infer information about asthenospheric rheology. Previous studies suggest that interactions of mantle wind arising from global mantle flow with highly varying lithospheric thickness can explain small-scale variations of seismic anisotropy (e.g. Conrad and Behn, 2010). Therefore, in addition to the EDC model, we also test the interactions of mantle wind from two global mantle flow models (Behn et al., 2004; Forte et al., 2010) with the lithosphere beneath Madagascar. We use the finite element code Advanced Solver for Problems in Earth′s ConvecTion (ASPECT, (Bangerth et al., 2018a,b; Heister et al., 2017; Rose et al., 2017)) to calculate 3D EDC and mantle wind interactions with the lithosphere beneath Madagascar and surroundings using shear wave tomography-derived lithospheric thickness that incorporates all available seismic data of the region (updated Fishwick (2010, updated)). Based on the modelled flow pattern, we use D-Rex (Kaminski and Ribe, 2001) to calculate LPO following the kinematic model for plastic deformation and dynamic recrystallization originally formulated by Ribe and Yu (1991) and further extended by Kaminski and Ribe (2001, 2002). Finally, we use calculated LPO as input to calculate synthetic splitting parameters (fast splitting direction and delay time) at the locations of seismic anisotropy observations using routines from FSTRACK (Becker et al., 2006), which we compare with observations. We find the majority of seismic anisotropy observations can be explained with EDC and interactions with mantle wind from Behn et al. (2004), which suggests dislocation creep extends into the upper asthenosphere beneath Madagascar.

This work yields new insights into present-day asthenospheric flow patterns beneath Madagascar. In addition, our work provides constraints on the dominant deformation mechanism

of the upper asthenosphere. Our numerical experiments suggest that dislocation creep rheology extends into the upper asthenosphere beneath continental regions and that accounting for dislocation creep flow laws is crucial for studies of sublithospheric mantle dynamics.

1.2 Tectonic History of Madagascar

Madagascar formed during the amalgamation of the Gondwana supercontinent 650 Ma (e.g. de Wit, 2003). The eastern part of Madagascar originated from the Indian Dharwar craton on eastern Gondwana and sutured with the western part of Madagascar, which was linked with the present-day African continent on western Gondwana. After the amalgamation of Gondwana via the subduction of the Mozambique Ocean, western Madagascar separated from the present-day Nubian Plate 160 Ma ago, and 50 Ma later, eastern Madagascar rifted from the Indian plate, resulting in the isolation of Madagascar, La Reunion, and the Comoros islands. During these tectonic events, the Malagasy lithosphere was subjected to collisional and extensional events that shaped the present-day geological features in Madagascar, including a suture in central Madagascar, shear zones, and rifts (Figure 1.2). The geology of Madagascar is distinct from east to west, with Precambrian rocks in the eastern two thirds of the island and Paleozoic to recent sedimentary (Antsiranana, Morondava and Mahajanga basin) and Cretaceous volcanic rocks covering the west.

Eastern Madagascar is the location of an important Neoproterozoic suture zone, known as the Betsimisaraka suture. It separates Mesoarchean rock that is parallel to the east coast and the Precambrian Antananarivo block (West Gondwana) (Collins, 2000; Collins and Windley, 2002; Collins et al., 2003). The Betsimisaraka suture is a highly deformed zone that consists of remnant consumed oceanic crust from the Mozambique Ocean which resulted from the collision between Eastern and Western Gondwana. Roughly trending N-S, the Betsimisaraka

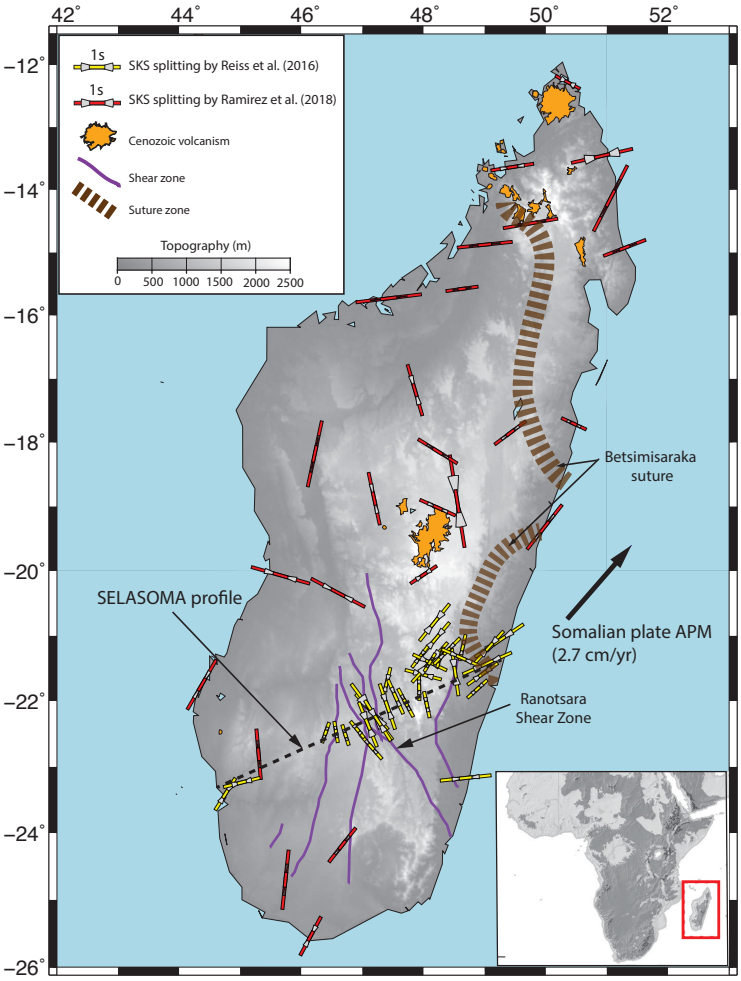

Figure 1.1: SKS splitting measurements across Madagascar. Red bars are splitting measurements from Ramirez et al. (2018). Yellow bars are splitting measurements (Reiss et al., 2016) from the SELASOMA profile (black dashed line). Gray wedges show confidence interval of the SKS splitting measurements. Orange regions represent Cenozoic volcanism. The black vector is the absolute plate motion direction (Argus et al., 2011). The background colors show topography.

suture is divided into two segments, the northeastern segment that separates the Archean Antongil block and the Precambrian Antananarivo block (Raharimahefa and Kusky, 2009) and the southern segment that separates the Archean Masora block and the Precambrian Antananarivo block (Raharimahefa and Kusky, 2006) (see Figure 1.2).

Southern Madagascar is a site of pre-existing weaknesses, of which the most prominent are the Neoproterozoic Ampanihy, Vorokafotra, and the late Proterozoic/early Cambrian Ranotsara shear zones (Figure 1.2). These shear zones are thought to be composed of high-grade metamorphic rock and are associated with the orogenic evolution of the Mozambique (590 - 500 Ma) belt during the East African orogeny (Martelat et al., 2000). The N-S striking Apanihy and Vorkafotra shear zones are >450 km in length and between 10 and 20 km in width. The Ranotsara shear zone (Ra in Figure 1.2) differs from the other shear zones in that it is striking ∼NW-SE instead of N-S. Because of this oblique strike, it has been correlated with various shear zones in east Africa and southern India (Windley et al., 1994) and used to infer the paleoposition of India and Madagascar before the Gondwana break-up (de Wit et al., 2001; Nicollet, 1990). It crosscuts >400 km of the Malagasy Precambrian basement. Although the Ranotsara shear zone is typically considered as an intracrustal mega strike-slip shear zone with a sinistral sense of shear (e.g de Wit et al., 2001), Schreurs et al. (2010) argue that the Ranotsara shear zone is a composite structure with ductile deflection in the central zone based on remote sensing and geologic observations. When Madagascar attained its current position with respect to Africa in the middle Miocene, lithospheric scale E-W extension began with the reactivation of N-S striking faults (Bertil and Regnoult, 1998) that formed rift basins such as the Alaotra-Ankay Rift (Figure 1.2). The late Proterozoic/early Cambrian Ranotsara Shear Zone has been reactivated with brittle faulting causing the formation of along strike basins filled with Neogene sediments (de Wit, 2003; Schreurs et al., 2010).

Madagascar has undergone Cretaceous and minor Cenozoic intra-plate magmatism and active volcanism. The eastern and coastal margins of Madagascar experienced voluminous basic lava extrusions that lasted at most 8 Mya during the late Cretaceous (Seward et al., 2004). The Cretaceous volcanics are sourced from the ancient Marion hotspot (c. 84 Ma; Meert and Tamrat, 2006), of which the volcano-tectonic interactions were responsible for magmatic rifting, thus allowing the breakup of India-Seychelles and Madagascar. The small Neogene-Quaternary volcanic regions are located in disparate locations along the island: at the northernmost tip of the island; along the Nosy-Be-Antongil axis (Massif d'Ambre and Nosy-Be Island); in the center (Itasy and Ankaratra volcanoes); and in the southwest (Ankililoaka volcanics; Figure 1.2).

1.3 Methods

1.3.1 Regional scale 3D edge-driven convection modeling

We simulate instantaneous regional mantle flow in a 3D domain using the open source finite-element code ASPECT v2.1.0 (Advanced Solver for Problems in the Earth's ConvecTion, Bangerth et al., 2018a,b; Heister et al., 2017; Rose et al., 2017). This research software has been successfully applied to a wide range of geodynamic settings such as mantle convection (Austermann et al., 2017; Zhang and O'Neill, 2016), plume dynamics (Bredow, 2017; Dannberg and Gassmöller, 2018; Steinberger et al., 2019), continental rifting (Corti et al., 2019; Heron et al., 2018), and subduction (Fraters et al., 2019; Glerum et al., 2018a). Using ASPECT, we solve for velocity, pressure, and temperature of the Stokes equations with the Boussinesq approximation, which consists of the equations of momentum, conservation of mass, and energy for incompressible fluid flow:

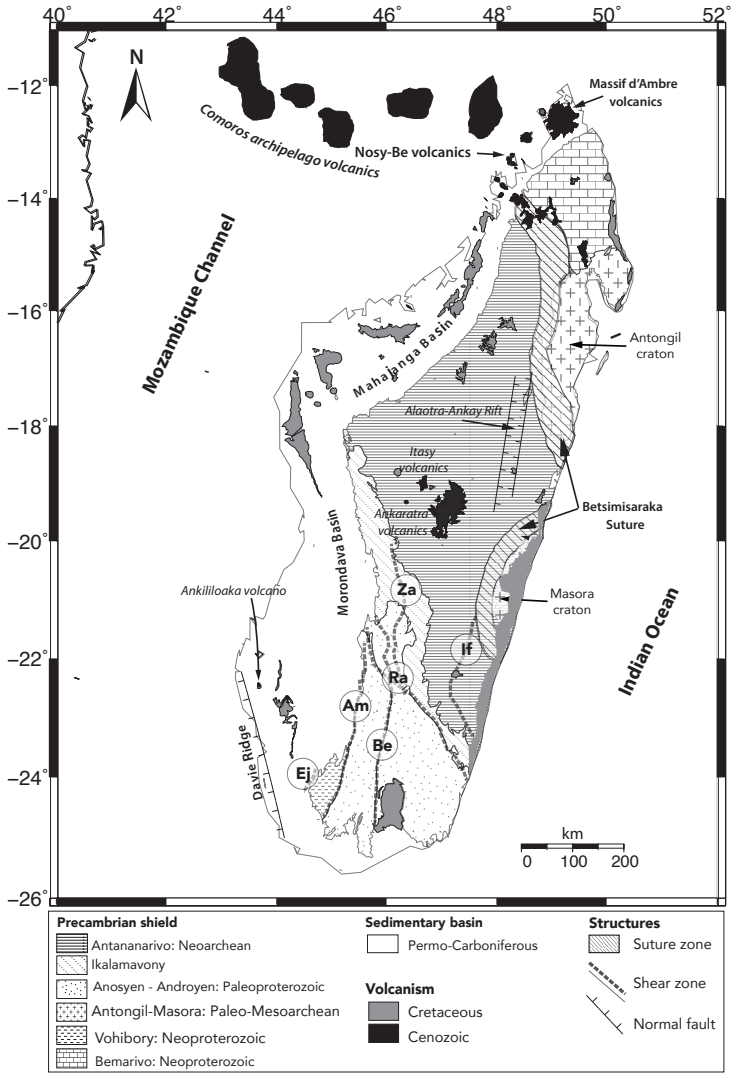

Figure 1.2: Simplified geologic map of Madagascar and the Comoros with key geologic features. Note the geological units (Tucker et al., 2012), Cretaceous (gray color) and Cenozoic (black regions) volcanism, and major structures such as the Alaotra-Ankay Rift, Betsimisaraka suture zone (Collins and Windley, 2002), the Davies Ridge, and the shear zone in southern Madagascar. Dark gray dashed lines indicates shear zones from Martelat et al. (2000): $Ej = Ejeda$, $Am = Ampanihy$, $Be = Beraketa$, $Ra = Ranotsara$, $If = Ifanadiana$, $Za = Zazafotsy$.

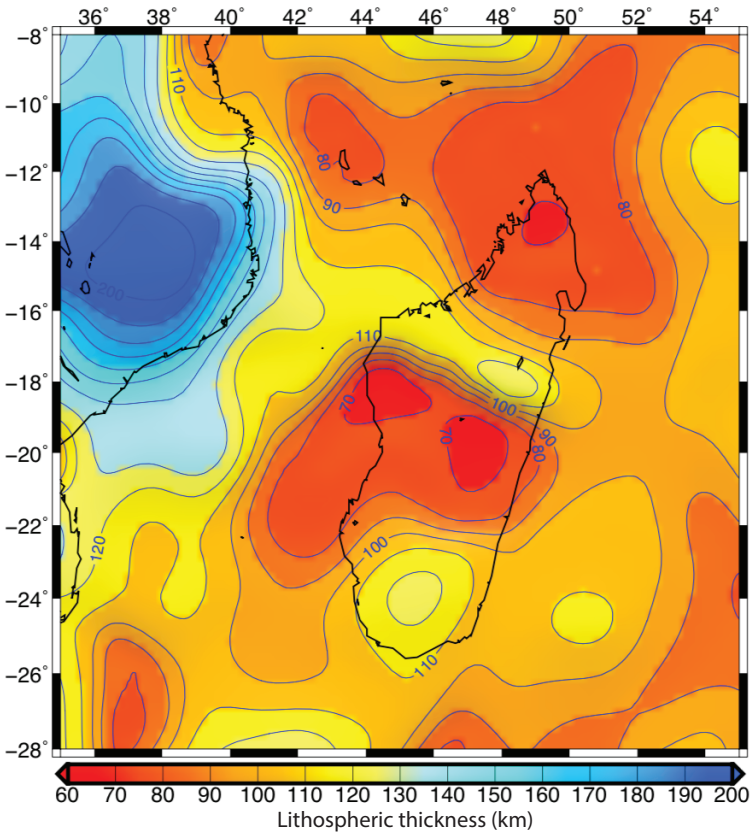

Figure 1.3: Lithospheric thickness model of Madagascar and its surroundings, updated from Fishwick (2010, updated), that we use as an input for our study. Contours show lines of equal lithospheric thickness at 10 km intervals.

$$-\nabla \cdot [2\eta\varepsilon(\mathbf{u})] + \nabla p' = -\rho_0 \alpha T \mathbf{g} \qquad \text{in } \Omega, \tag{1.1}$$

$$\nabla \cdot \mathbf{u} = 0 \qquad \text{in } \Omega, \tag{1.2}$$

$$\rho_0 C_p \left(\frac{\partial T}{\partial t} + \mathbf{u} \cdot \nabla T \right) - \nabla \cdot k \nabla T = \rho H \qquad \text{in } \Omega. \tag{1.3}$$

$\varepsilon(\mathbf{u})$ is the symmetric gradient of velocity, η is viscosity, ρ is density, ρ_0 is the constant reference density, p' is dynamic pressure, T is temperature, $\mathbf{g}$ is gravitational acceleration, α is thermal expansion coefficient, κ is thermal conductivity, H is intrinsic specific heat production, and C_p is specific heat capacity. The effects of shear heating and adiabatic heating are neglected in the model. We employ the "single Advection, iterated Stokes" solver scheme, which solves the temperature and composition equation once at the beginning of each time step and then iterates out the solution of the Stokes equation. Our model domain is approximately 2200×2200×660 km along longitude, latitude, and depth, respectively, for a spherical chunk geometry. The model domain is initially globally refined and each element is approximately 34×34×10 km. The computation consists of 14 million unknowns solved on 192 cores. The model includes both lithosphere and sublithospheric mantle. The depth extent of 660 km is chosen as it corresponds to the 660 km seismic discontinuity associated with large viscosity increases (e.g. Forte and Mitrovica, 1996) and endothermic phase-changes of olivine (Dziewonski and Anderson, 1981). Because of the phase change and the viscosity jump, we assume that the 660 km seismic discontinuity is an appropriate depth to investigate upper mantle flow.

The initial temperature field (Figures 1.4A, 1.5A) incorporates an approximate conductive and an adiabatic geothermal gradient. The initial thermal structure of the lithosphere is assumed to be a linear gradient from the surface (273 K) to the lithosphere-asthenosphere

Table 1.1: Parameters used for EDC simulation.

Parameter	Symbol	Value	Units
Reference density	ρ_0	3300	$kg.m^{-3}$
Thermal conductivity	κ	3	$W.m^{-1}.K^{-1}$
Specific heat capacity	C_p	1.25×10^{3}	$J.kg^{-1}.K^{-1}$
Intrinsic specific heat production	H	7.4×10^{-12}	$W.kg^{-1}$
Thermal expansion coefficient	α	4×10^{-5}	K^{-1}
Gravitational acceleration	g	PREM	$m.s^{-2}$

boundary (LAB). The base of the lithosphere is a thermomechanical boundary where the temperature is 1673 K, which is generally the upper bound of the mantle potential temperature (Hirschmann, 2010; Langmuir et al., 1992; Stixrude and Lithgow-Bertelloni, 2007). We choose the 1673 K because it is the estimated geophysical average of global mantle potential temperature according to Anderson (2000). The sublithospheric mantle temperature increases approximately adiabatically (0.5 K/km) to the base of the model.

The updated lithospheric structure model of Fishwick (2010, updated) is mapped into the 3D domain for Madagascar and surroundings (Figure 1.3). The lithospheric thickness is thinnest in central (∼70-80 km) and northern (∼70-80 km) Madagascar with a NW-SE trending belt of thicker lithosphere between the two regions (∼110-120 km). In southern Madagascar the lithosphere is thicker compared to central Madagascar (∼110-120 km). The lithospheric structure produces lateral variations in temperature such that relatively thick lithosphere features smaller geothermal gradients and is relatively cooler than thinner lithosphere (Figure 1.4a).

The lithosphere is assumed to be in a thermal steady state and without internal deformation, which is implemented by imposing a strong uniform viscosity of 10^{25} Pa.s (Figures 1.4B, 1.5B). We assume that the composition of the underlying mantle is dry olivine and that the viscosity is governed by composite rheology (Jadamec and Billen, 2010). Composite rheology

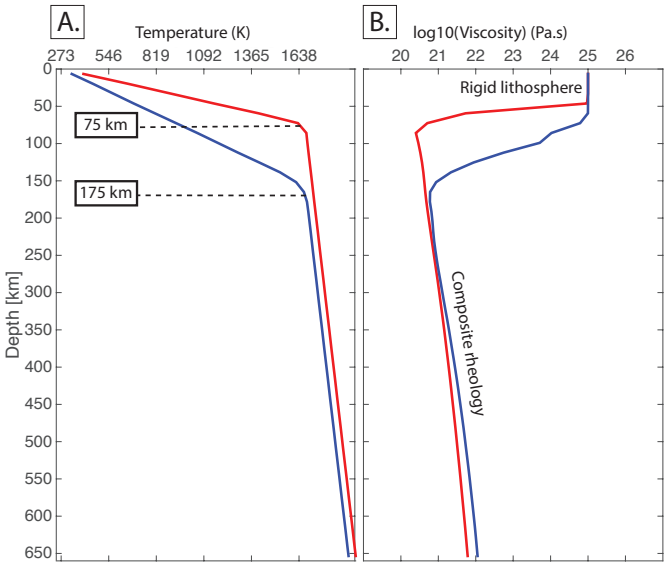

Figure 1.4: A. One dimensional temperature depth profiles for a lithospheric thickness of 75 km (red) and 175 km (blue). The temperature at the base of the lithosphere (1673 K) corresponds to the intersection of the conductive and adiabatic geothermal gradients. B. Corresponding viscosity profiles for 75 km (red) and 175 km (blue) thick lithosphere.

is a harmonic average of viscosity from diffusion creep (η_{diff}) and dislocation creep (η_{disl}) mechanism of olivine. The composite viscosity η_{comp} is given by :

$$\eta_{diff,disl} = \frac{1}{2} A^{-\frac{1}{n}} d^{\frac{m}{n}} \dot{\epsilon}^{\frac{1-n}{n}} exp\left(\frac{E_a + V_a P}{nRT}\right) \tag{1.4}$$

$$\eta_{comp} = \frac{\eta_{diff}\eta_{disl}}{\eta_{diff} + \eta_{disl}} \tag{1.5}$$

$\dot{\epsilon}$ is the square root of the second invariant of the strain rate tensor, T is temperature, P is pressure, E_a is activation energy, V_a is activation volume, n and m are, respectively, the stress and grain size exponents, A is pre-exponent factor, and R is the gas constant. The parameters A, E_a, V_a, n and m are obtained from experimental studies of the olivine mineral from Hirth and Kohlstedt (2003) and their values are given in Table B.2. The material of each layer (i.e

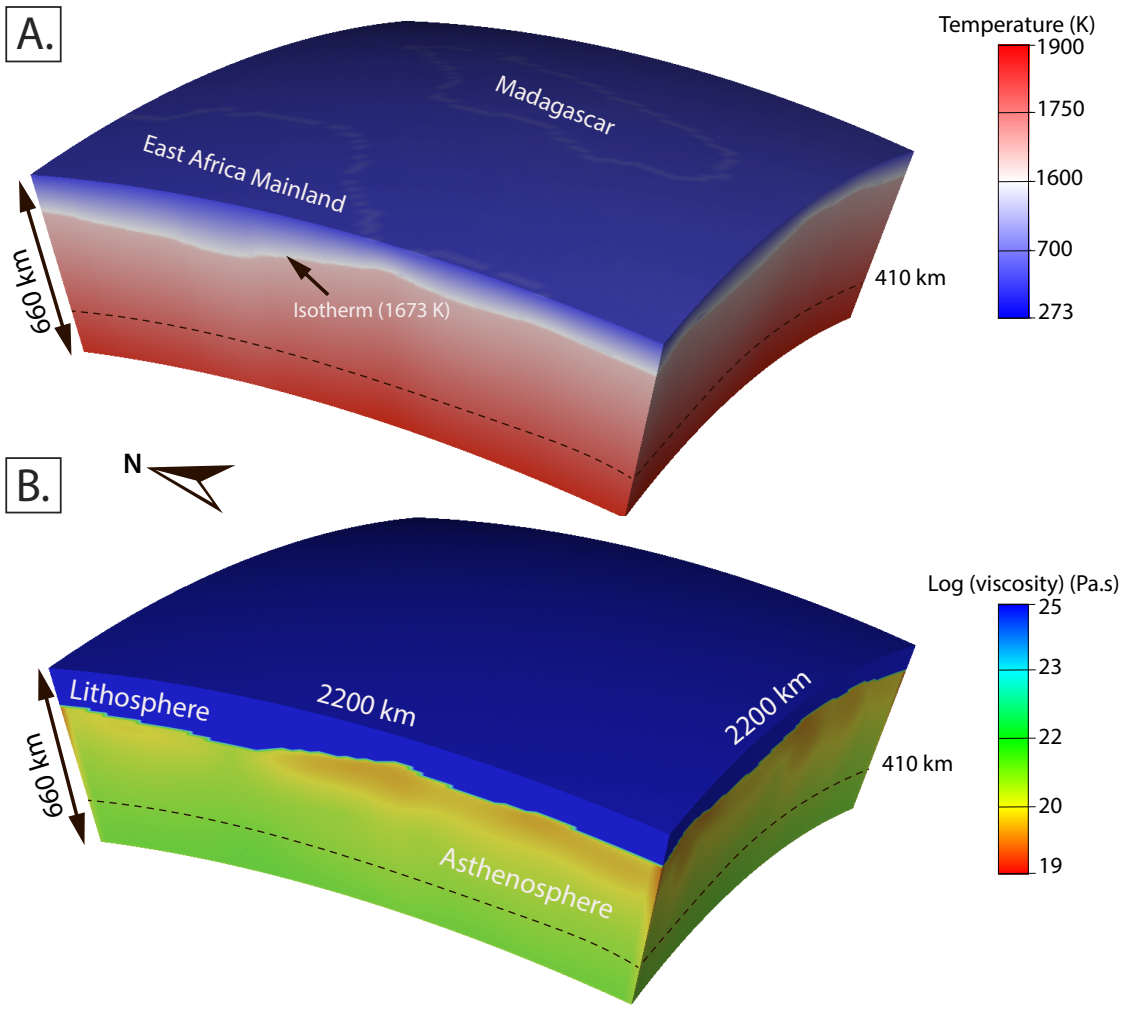

Figure 1.5: Numerical model setup: A. Initial temperature condition. B. Initial viscosity field.

Table 1.2: Parameters used for the viscosity flow law of the sublithospheric mantle for dry olivine.

Parameter	Symbol	Dislocation creep	Diffusion creep	Units
Grain size	d	-	$10{\times}10^{3}$	μm
Grain size exponent	m	-	3	-
Activation energy	E_a	$530\ {\times}10^{3}$	$375\ {\times}10^{3}$	$J.mol^{-1}$
Activation volume	V_a	$18{\times}10^{-6}$	$6{\times}10^{-6}$	$m^3.mol^{-1}$
Prefactor	A	$6.52{\times}10^{-16}$	$1.5{\times}10^{-15}$	-
Stress exponent	n	3.5	1.0	-

lithosphere and sublithospheric mantle) is tracked through compositional fields, which carry properties of the Earth's material within the convective flow. Using compositional fields allows for smoothing across compositional boundaries, which is needed to solve for sharp variations in the viscosity model, which are also smoothed.

The viscosity at each quadrature point is calculated using an harmonic average of the compositional fields weighted by the volume fraction of each composition at the same location (Figures 1.4B, 1.5B). The velocities at the sides and base of the model are set to zero and the surface is free-slip to neglect all effects of global mantle flow and to enhance regional resolution such that we can test our hypothesis regarding EDC. The velocities at the bottom boundary are set to zero to account for the high viscosity jump across the transition zone. The temperature boundary conditions at all boundaries are fixed so that net heat flux at the boundaries is zero.

1.3.2 Modeling mantle wind interactions with the lithosphere

To test lithosphere-mantle wind interactions based on the Behn et al. (2004) and the Forte et al. (2010) global mantle flow models, we subsequently impose velocity boundary conditions that align with global mantle flow at the vertical boundaries (West, North, South and

East) of our regional model and use the same initial conditions as the EDC model. We simulate two mantle wind models using horizontal mantle flow from: 1) Forte et al. (2010) that is trending ~N20E, and 2) Behn et al. (2004) which is oriented ~N80E. Both studies found a similar mantle flow velocity relative to Madagascar of approximately 10 mm/yr, which is why we use this value in both scenarios. In order to simulate the mantle wind, our reference coordinate system is fixed to Madagascar, thus we impose a zero velocity boundary condition at the vertical boundaries in lithospheric regions. Given the highly varying lithospheric thickness at the vertical boundaries (Figure 1.3), the zero velocity boundary condition is imposed to regions shallower than the maximum lithospheric thickness of the model ($\leq$200 km depth), while we impose mantle flow velocities below 200 km depth at all vertical boundaries. These velocity boundary conditions have the same magnitude and orientation at all vertical boundaries so that inflow and outflow are balanced as required by the incompressible model (Equation 2).

1.3.3 Estimating shear-wave splitting parameters

In a first step, we use the program D-Rex (Kaminski et al., 2004) to predict sub-lithospheric LPO that develops beneath Madagascar as a result of EDC. We calculate synthetic LPO of olivine polycrystalline aggregates following the kinematic model for plastic deformation, grain boundary sliding, and dynamic recrystallization originally formulated by Ribe and Yu (1991) and further extended by Kaminski and Ribe (2001, 2002). All crystallographic input parameters are obtained from Kaminski et al. (2004) and from Becker et al. (2006), where the dimensionless parameters $\lambda^* = 5$, $M^* = 125$, and $\chi = 0.3$ are, respectively, the nucleation rate, the intrinsic grain boundary mobility, and the threshold volume fraction below which grain boundary sliding takes place.

Using D-Rex, we follow tracers to calculate accumulated synthetic LPO that develops along pathlines in the EDC flow field assuming steady state flow. A single tracer represents a mineral aggregate consisting of 2000 virtual grains of olivine (70%) and enstatite (30%) crystals (Kaminski et al., 2004), which represents a harzburgite composition. Since there is sensitivity of LPO with resolution, the flow field is interpolated onto a 15×15 km horizontal grid with 10 km depth resolution to capture variations in LPO patterns that may occur. Following the approach of (Becker et al., 2006), the initially unstrained tracers are placed at starting positions at different depths below the locations where observations exist (Figure 1.1). We restrict the tracers to locate between a depth of 100 km and 400 km with a vertical interval of 25 km to ensure asthenospheric material is captured beneath thinner lithosphere (Figure 1.3). The trajectory of each tracer is computed by advecting the tracer backward in time using the fourth order Runge-Kunta advection scheme described in Becker et al. (2003). The backward advection is stopped when tracers either accumulate critical strain, a maximum advection time of 40 Ma is reached, or they arrive at a threshold depth of 410 km, below which mineral fabrics are erased at the transition zone.

The critical strain is a logarithmic saturation strain ξ_c, defined as the minimum of $log(e_1/e_2)$ and $log(e_1/e_3)$, where e_1, e_2 and e_3 are the largest, intermediate, and smallest eigenvalue of the finite strain ellipsoid, respectively. Ribe (1992) shows that ξ_c controls the strength of the anisotropy and a $\xi_c \geq 0.5$ is required to match the natural heterogeneity of LPO found in upper mantle xenoliths. Here, the fabrics are calculated up to a saturation $\xi_c = 0.75$ still following Becker et al. (2006). At the location where the tracer reaches ξ_c, it is set with randomly oriented crystals to form isotropic mantle and advected forward until it reaches the position from which it has been initially distributed. To minimize the diffusion creep contribution, we scale the strain rate tensor with the viscosity ratio $\gamma = \frac{\eta_{diff}}{\eta_{disl}}$ during the forward advection.

As the mineral aggregates accumulate finite strain, LPO develops and evolves along the pathlines in response to shear. D-Rex outputs the volume fractions and orientations of individual crystals that form the aggregates (collectively called the orientation distribution function). The orientation distribution function and single-crystal elastic tensors of olivine-enstatite provided by D-Rex are used to calculate the global elastic tensor of the grain assemblage using the Voigt averaging scheme. Considering the dominant hexagonal anisotropy of the elastic tensor, the orientation of the symmetric axis of the elastic tensor is calculated, which is known as the transverse isotropic approximation (TI). TI indicates the direction of elastic anisotropy that has been a widely used proxy for LPO (e.g. Becker et al., 2006; Faccenda and Capitanio, 2012; Hu et al., 2017).

In a second step, we use the elastic tensors of the olivine-enstatite aggregates calculated in step one as input for FSTRACK (Becker et al., 2006). FSTRACK calculates synthetic splitting parameters (fast direction Φ and delay time δt) where measurements exist (Figure 1.1). Synthetic seismograms are computed for an Earth model of multi-layer anisotropy using the cross-correlation method developed by Menke and Levin (2003). The program constructs a stack of horizontal layers that are 25 km thick and centered at 100 km to 400 km with a 25 km interval, and defined by the elastic tensors of the olivine-enstatite aggregates below the seismic stations. Then FSTRACK computes the synthetic seismograms by calculating the sum of the harmonic responses of rays (over a range of frequencies >0 - 25 Hz) vertically polarized at a 5° incident angle, traversing the horizontal layers. The resulting seismograms are filtered by a band-pass filter with frequency cut-offs from 0.1 - 0.3 Hz that represent the typical frequency band for SKS waves (e.g. Faccenda and Capitanio, 2012, 2013). Due to dependence of splitting parameters on back-azimuth (Becker et al., 2006), a set of fast polarization directions and delay times are calculated with elastic tensors rotated about the vertical axis around 360° with an increment of 2°. The circular mean of the fast directions

and mean delay times represent the synthetic splitting at each station.

1.4 Results

1.4.1 Edge-Driven Convection Beneath Madagascar

Results of the 3D simulations show that EDC forms where the lithosphere transitions from thin to thick (see Figure 1.3). Figure 1.6 portrays map views of the EDC flow field beneath Madagascar and surroundings at different depth slices with the background colors showing vertical motions and the vectors indicating horizontal motions at that depth. Cold downward flow occurs beneath thick lithosphere and upwelling occurs beneath relatively thin lithosphere. Hence, upwelling and diverging asthenospheric flow is located beneath central and northern Madagascar (Figure 1.6A) as well as beneath the Comoros archipelago volcanics in regions where the lithosphere is relatively thin.

In northernmost Madagascar, a region of relatively thin lithosphere (∼70-80 km) lies adjacent to a belt of ∼120 km thick lithosphere that strikes NW-SE and gradually increases in thickness towards the African mainland. As a result, this region develops asthenospheric upwelling in northern Madagascar (∼0.5 mm/yr vertical velocity) and downwelling beneath the belt of thick lithosphere (∼1 mm/yr vertical velocity; Figure 1.6). The corresponding horizontal velocity shows a radial outward flow asymmetrically spreading to the ENE direction at the eastern side of the northern region and to the SW direction at the western side of the northern region that ranges from ∼0.1-1 mm/yr (Figure 1.6, A-D). Beneath the Comoros archipelago volcanics, upwelling increases to ∼2 mm/yr at 200 km depth, due to the sharp increase in lithospheric thickness variation beneath the African mainland.

Central Madagascar features the largest zone of thin lithosphere (∼60 - 70 km) across the

continental island. It is bounded to the north by the belt of thick lithosphere that strikes ∼NW-SE, to the south by thick lithosphere (∼120 km), and further to the west by the thickest lithosphere (∼200 km) within the African mainland. The lithospheric thickness configuration induces a relatively stronger and broad upwelling beneath central Madagascar from 250 - 125 km depths, which has been hypothesized by Reiss et al. (2016). The horizontal velocity shows a radial pattern with the minimum horizontal velocity at the center of Madagascar where the flow is mostly vertical. The strength of upwelling in central Madagascar increases with depth.

Asthenospheric flow beneath southern Madagascar is characterized by pronounced downwelling as shown in Figure 1.6. There is a minor shift in orientation of horizontal flow between shallower and deeper regions. At 125 and 150 km depths, the flow pattern in the transition between central and southern Madagascar features a southward direction of horizontal flow. Vertical downwelling is also more prominent at shallower depths in the center of southern Madagascar shown by the low magnitude horizontal vectors.

In order to assess the temporal stability of EDC beneath Madagascar and the robustness of our results, we simulate the flow field up to a maximum time of 35 Ma. Figure 1.7 (A and B) shows EDC and temperature along the long axis of Madagascar, profile AA' defined in Figure 1.6A at $t = 0$ and at $t = 35$ Ma, respectively. The velocity and temperature fields along the profiles illustrate how EDC is initiated from the lateral variations in temperature and the associated buoyancy forces. There are three pronounced steps in lithospheric thickness across the long axis of Madagascar, which, in turn, generate three convection cells centered at 22°S, 18°S, and 16°S that spread to the base of the model domain. Longer wavelength variations in lithosphere thickness induce wider convection cells as seen beneath northernmost Madagascar, while steeper variations generate smaller convection cells, such as in central Madagascar.

At both $t = 0$ and $t = 35$ Ma, central Madagascar is the site of diverging upwelling and adjacent downwelling that occurs beneath southern Madagascar and the belt of thicker lithosphere to the north. At the initial stage ($t = 0$), downwelling and upwelling asthenospheric flows located in and around central Madagascar have similar magnitudes with a maximum velocity of 2 mm/yr, whereas upwelling is generally faster ($\sim$50 mm/yr) and more focused in central Madagascar at t =35 Ma because hotter mantle materials are brought to shallower depths. The velocity magnitude of 2 mm/yr from EDC at $t = 0$ is consistent with the expected weak flow of EDC (e.g. King and Anderson, 1998), whereas the $\sim$50 mm/yr velocity magnitude at $t = 35$ Ma is in the range of large scale mantle flow (e.g. Moucha and Forte, 2011; Schuberth et al., 2009). In northern Madagascar there is a broad region of upwelling that is similar in magnitude and direction over the 35 Ma time-frame. The main result of this comparison is that the main asthenospheric structures are stable over geological time-frames.

As an additional robustness test, we assess the behavior of our model with respect to uncertainties associated with lithospheric thickness derived from shear wave tomography. We address this point by conducting simulations where we vary the lithospheric thickness between +10 km and −10 km. In all cases we find that the structure of the convective flow remains stable through time with upwelling beneath central and northern Madagascar and adjacent downwelling.

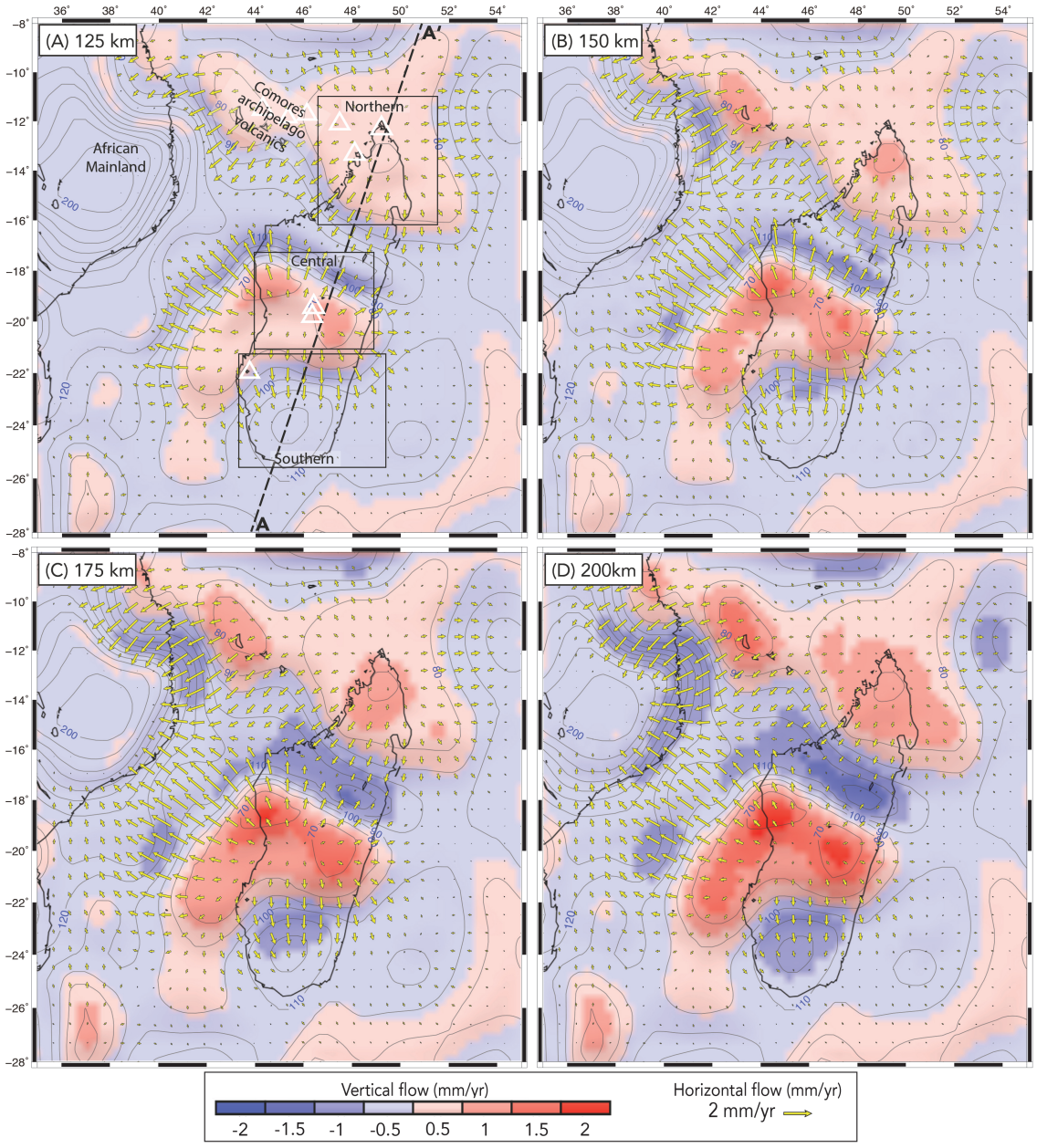

Figure 1.6: Depth slices showing EDC beneath Madagascar at (A) 125 km, (B) 150 km, (C) 175 km, and (D) 200 km depths at initial time (Time = 0 Ma). Background color indicates vertical flow. Yellow vectors portray horizontal flow. We infer two regions below Madagascar that are dominated by upwelling and two regions with downwelling. White triangles in (A) indicate Cenozoic volcanic regions which are also illustrated in Figure 1.2.

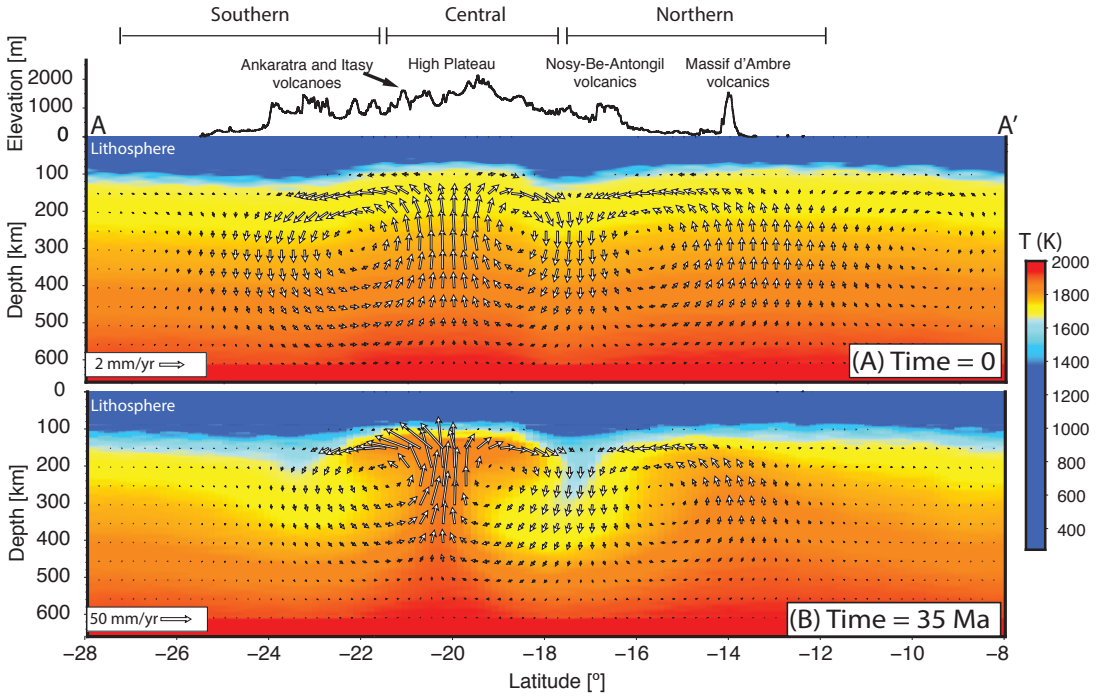

Figure 1.7: Profile showing time-dependent convection across the long axis of Madagascar (profile AA' in Figure 1.6). (A) Time = 0 Ma. (B) Time = 35 Ma. Note the similarity in the structures of mantle flow beneath the continental island.

1.4.2 Mantle wind interactions with lithosphere beneath Madagascar

Figure 1.8A-C shows asthenospheric flow at 125 km all three models (EDC, Behn et al. (2004), and Forte et al. (2010), respectively). Horizontal velocities of the Behn et al. (2004) model (Figure 1.8B) shows mostly ∼N80E trends with magnitudes of 20-30 mm/yr across Madagascar and surroundings. These horizontal velocities are not significantly deflected at the transition from relatively thick to thin lithosphere. However, the magnitude of the horizontal velocities is three times that of the mantle wind applied at the boundaries. This increase in velocity magnitude beneath Madagascar is in response to the low viscosity channel in sublithospheric regions. The vertical velocity shows a similar pattern as the EDC i.e. localized upwelling beneath northern and central Madagascar (∼4 mm/yr vertical velocity), downwelling beneath the belt of thick lithosphere (∼6 mm/yr vertical velocity) and downwelling beneath southern Madagascar (∼2 mm/yr vertical velocity).

Figure 1.8C shows the mantle flow results from mantle wind model of Forte et al. (2010). Horizontal velocities show a mostly ∼N20E trend with magnitudes of 20-30 mm/yr across Madagascar and surroundings. The vertical velocities also show a pattern similar to the EDC models.

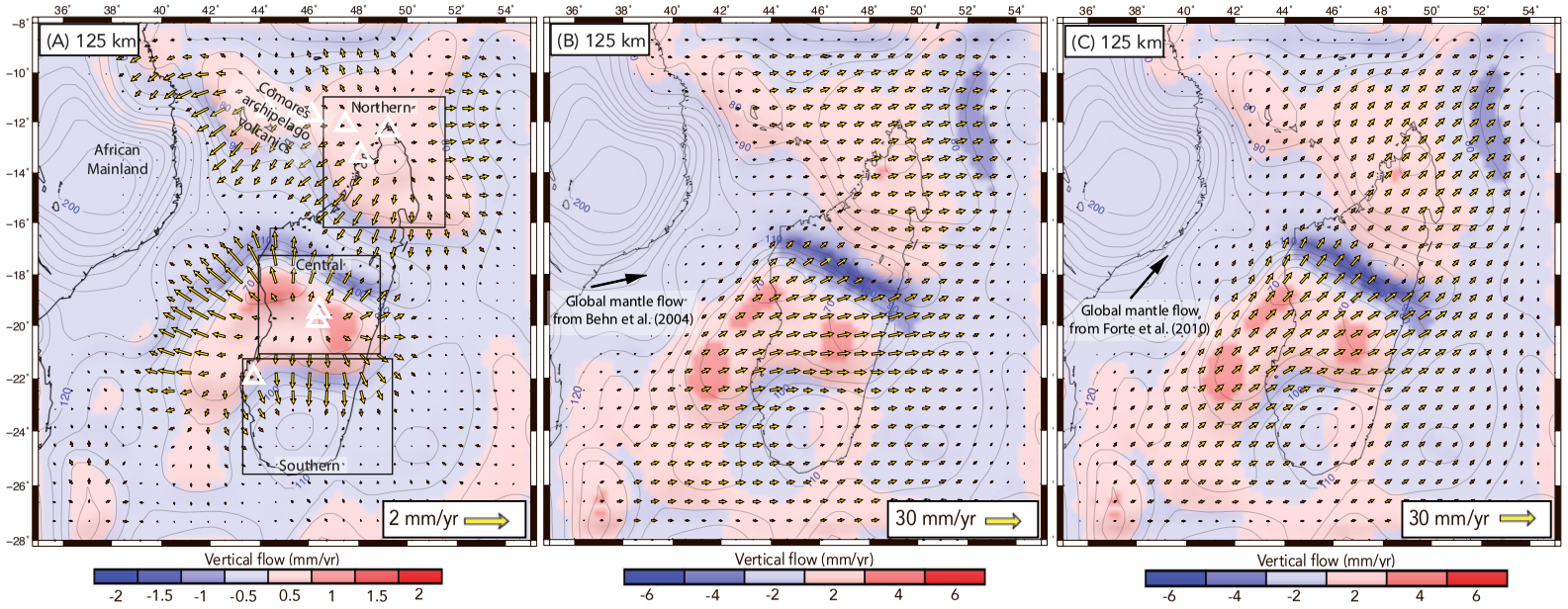

Figure 1.8: Depth slices showing mantle flow fields at initial time (Time = 0 Ma) at 125 km. A) for EDC model, B) from mantle wind of Behn et al. (2004) global mantle flow, C) from mantle wind of Forte et al. (2010) global mantle flow. Background color indicates vertical flow. Yellow vectors portray horizontal flow. The vertical flow show similar pattern for all models where we infer two regions below Madagascar that are dominated by upwelling and two regions with downwelling. White triangles in (A) indicate Cenozoic volcanic regions which are also illustrated in Figure 1.2. Black arrows in B and C indicate the direction of mantle wind of Behn et al. (2004) and Forte and Mitrovica (1996), respectively.

1.4.3 Comparison between observed and synthetic SKS splitting

In this section, we present the comparison of predicted and observed splitting at individual seismic stations where each of the observations exist (Figure 1.9). Due to the high variability of the anisotropy orientations in Madagascar, we present the measurements and observations regionally, partitioned into northern, central, south-central, and southeast Madagascar, after Ramirez et al. (2018) (Table 3). We provide the predicted splitting parameters and TI axes in the PANGAEA repository (doi:10.1594/PANGAEA.909406).

Table 1.3: A comparison of the fit to anisotropy and calculated delay times for the three models produced in this work (EDC, mantle wind from Behn et al. (2004), mantle wind from Forte et al. (2010)). $<\phi_{obs}>^{\circ}$ and $<\delta t_{obs}>$ are the observed mean fast direction and mean delay time, respectively. $<\phi_{synt}>^{\circ}$, $<\Delta\alpha>^{\circ}$ and $<\delta t_{synt}>$ are the calculated mean fast direction, the mean angular misfit and the delay time, respectively. The model output files are available at the PANGAEA repository with doi:10.1594/PANGAEA.909406.

	Observations		Edge Driven Convection			Mantle wind from Behn et al., 2004			Mantle wind from Forte et al., 2010		
Region	$<\phi_{obs}>^{\circ}$	$<\delta t_{obs}>$ (s)	$<\phi_{synt}>^{\circ}$	$<\Delta\alpha>^{\circ}$	$<\delta t_{synt}>$ (s)	$<\phi_{synt}>^{\circ}$	$<\Delta\alpha>^{\circ}$	$<\delta t_{synt}>$ (s)	$<\phi_{synt}>^{\circ}$	$<\Delta\alpha>^{\circ}$	$<\delta t_{synt}>$ (s)
Northern	N68°E	1.00	N85°E	22°	0.92	N65°E	20°	0.78	N47°E	40°	0.89
Central	S39°E	1.00	N60°E	35°	0.88	N55°E	46°	0.71	N57°E	47°	0.92
South Central	S20°E	0.66	S18°E	18 °	0.76	N31°E	50°	0.67	N23°E	43°	1.02
South East	N29°E	0.74	N47°E	26°	0.79	N31°E	37°	0.71	N06°E	32°	0.88

Comparison with Edge-Driven Convection-derived splitting

For northern Madagascar (Region A; Figure 1.9), the observed homogeneous fast direction ϕ_{obs} pattern (N63°E) is well reproduced by the EDC model (∼N85°E), with a mean regional misfit of 22° (Figure 1.9). For central Madagascar (Region B; Figure 1.9) the observed complex fast direction ϕ_{obs} patterns (∼S39°E) are poorly reproduced by the EDC model (∼N60°E), with a mean regional misfit of 35°. Central Madagascar has 12 SKS splitting observations. The large average misfit is mainly due to two stations at the east and one station at the west. We find a good fit at four individual stations in the center of the region and two stations in the southwest corner with an average misfit less than 15° degrees. For south-central Madagascar (Region C in Figure 1.9) the observed fast direction ϕ_{obs} patterns (∼S20°E) are well reproduced by the EDC model (∼S18°E), with a mean regional misfit of 18° (Figure 1.9). LPOs are consistent with the EDC induced southward flow in south-central Madagascar. For southeastern Madagascar (Region D; Figure 1.9) the observed fast direction ϕ_{obs} patterns (∼N029E) are also well reproduced by the EDC (∼N47°E) except for 2 sites that are located on a shear zone. There is a mean regional misfit of 26°.

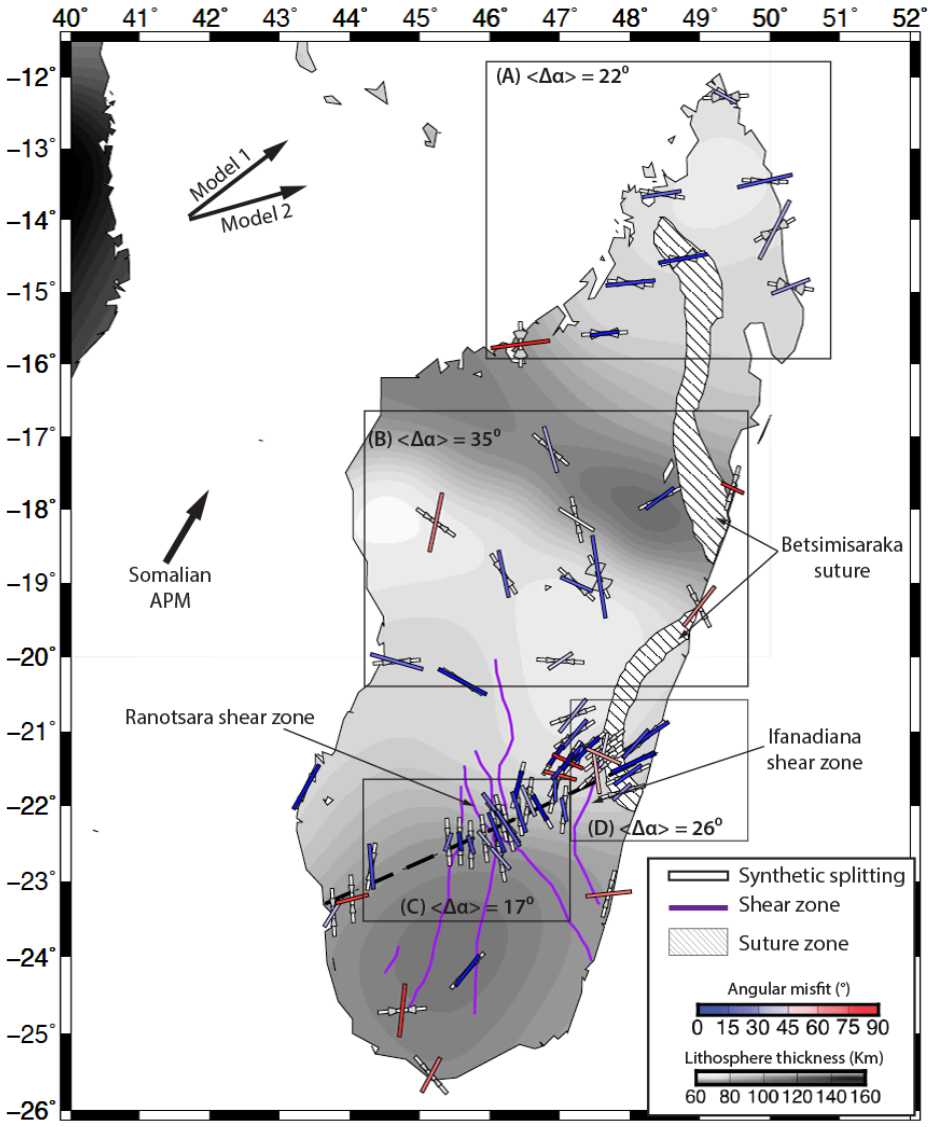

Figure 1.9: Comparison of synthetic splitting directions derived from EDC model (white bars) with SKS splitting measurement bars colored according to angular misfit [0° - 90°] (Ramirez et al., 2018; Reiss et al., 2016). Gray wedges represent confidence interval associated with the synthetic splitting. Rectangular boxes A,B,C, and D depict key regions and $<\Delta\alpha>$ indicates regional circular mean angular misfit within each rectangular box. Purple lines show shear zones after Martelat et al. (2000). Background gray scale color shows lithospheric thickness, an updated version of Fishwick (2010, updated). Black dashed line indicates the SELASOMA profile. Black arrows show the Somalian plate APM (Argus et al., 2011), Model 1 and Model 2 are global mantle flow directions from Forte et al. (2010) and Behn et al. (2004), respectively.

Comparison with mantle wind-derived splitting

In Figure 1.12 we show an example of comparison of TI axes with the observations from the three models at 150 km depth and describe below the overall comparisons with calculated synthetic splitting. The TI axis comparisons at different depths are provided in the Supplementary material. For northern Madagascar (Region A; Figure 1.10A,B), the observed homogeneous fast direction ϕ_{obs} pattern (N63°E) is well reproduced by the Behn et al. (2004) mantle wind model (∼N65°E), with a mean regional misfit of 20° (Figure 1.9), supporting the interpretation that the anisotropy is sourced from below the lithosphere. The Forte et al. (2010) mantle wind model (∼N47°E) produces a poor fit, with a mean regional misfit of 40°. For central Madagascar (Region B; Figure 1.10A,B), both Behn et al. (2004) and Forte et al. (2010) mantle wind models produce mean fast azimuth ∼S39°E and ∼S55°E, respectively, which poorly fit the observed complex pattern ϕ_{obs} pattern (∼S39°E) with a mean regional misfit of 46° and 57°, respectively. For south-central Madagascar (Region C; Figure 1.10A,B), both Behn et al. (2004) and Forte et al. (2010) mantle wind models produce fast direction patterns (∼N31° and ∼N23°E, respectively) roughly perpendicular to the observed fast direction ϕ_{obs} patterns (∼S20°E) , with a mean regional misfit of 50° and 43°, respectively. Both mantle wind models (Behn et al. (2004) and Forte et al. (2010); ∼N31°E and ∼N06°E, respectively) in southeastern Madagascar (Region D; Figure 1.10A,B) poorly fit the observed fast direction ϕ_{obs} patterns (∼N47°E), with mean regional misfits of 37° and 32° (Figure 1.10A,B). Although several seismic stations in Region D (Figure 1.10A,B) show less than 15° individual angular misfit, the overall calculated patterns show complex fast directions. The complex fast directions are due to patterns of the calculated LPO (TI axis) as well as their variations with depths (Region D in Figure S4 and Figure S5) from the mantle wind models.

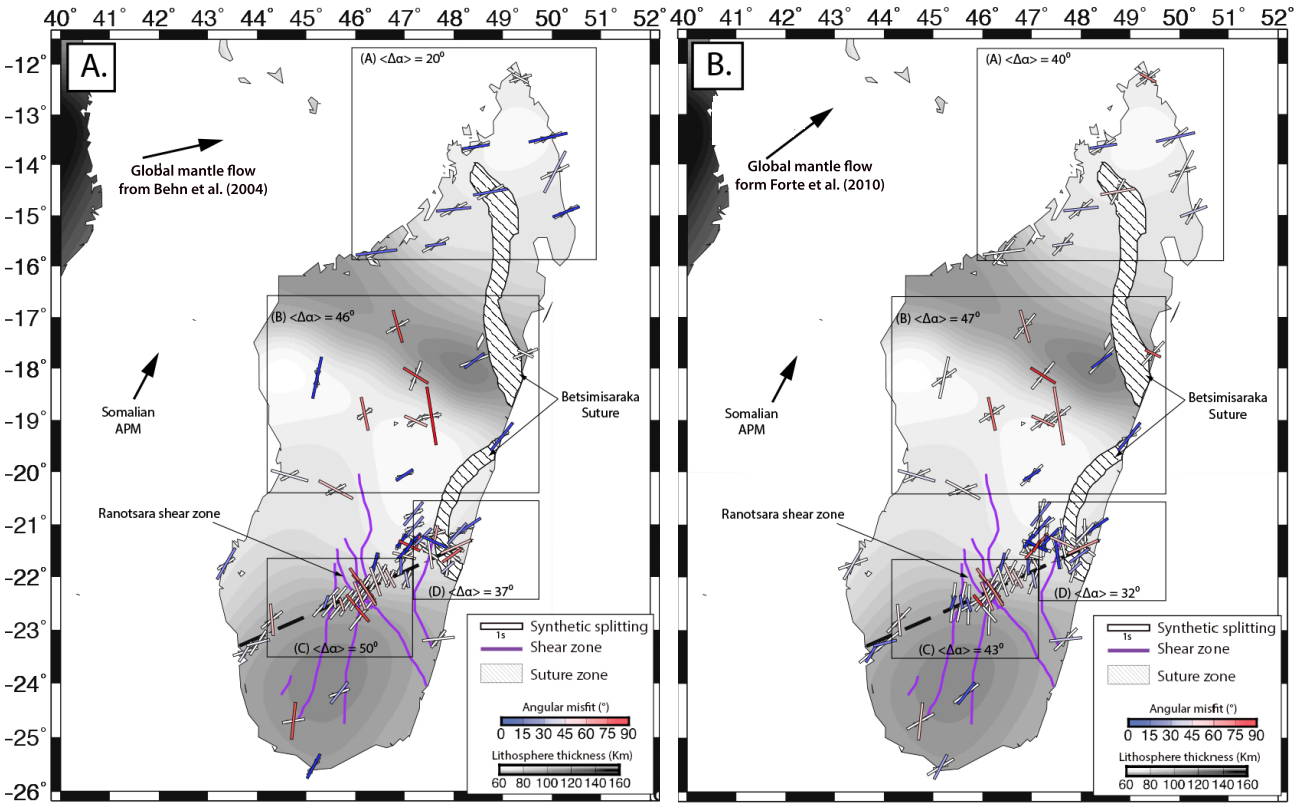

Figure 1.10: Comparison of synthetic splitting (white bars) derived from lithosphere-mantle wind interactions models with SKS splitting measurement bars colored according to angular misfit [0° - 90°] (Ramirez et al., 2018; Reiss et al., 2016). A) for Behn et al. (2004) global mantle flow. B) for Forte et al. (2010) global mantle flow. Gray wedges represent confidence interval associated with the synthetic splitting. Rectangular boxes A,B,C, and D depict key regions and $<\Delta\alpha>$ indicates regional circular mean angular misfit within each rectangular box. Purple lines show shear zones after Martelat et al. (2000). Background gray scale color shows lithospheric thickness, an updated version of Fishwick (2010, updated). Black dashed line indicates the SELASOMA profile. Black arrows show the Somalian plate APM (Argus et al., 2011), Model 1 and Model 2 are global mantle flow directions from Forte et al. (2010) and Behn et al. (2004), respectively.

1.5 Discussion

1.5.1 Sources of complex seismic anisotropy beneath Madagascar

Overall, the synthetic splitting fast directions ϕ_{calc}, derived from EDC induced olivine type-A LPO, are in good agreement with most of the SKS splitting measurements in Madagascar, particularly in the north and the south. In this section, we compare both the predicted splitting orientations and the TI axis orientation at various depths (Figure 1.11A-F) to aid in indicating the depths of the seismic anisotropy measurements since TI can be used as a proxy for LPO. To determine whether the observed anisotropy in Madagascar can be explained with fossil anisotropy, based on Helffrich (1995), the layer thickness to produce a splitting delay is $L = \frac{dt \times <V_s>}{dV_s}$ where L is the thickness, $< V_S >$ is the average shear wave velocity, and dt is the delay time and dV_S is the percentage anisotropy. Thus, the delay time can be calculated using $dt = \frac{L \times dV_s}{<V_s>}$. Assuming a 4% anisotropy (Savage, 1999) in the lithosphere, an average shear wave velocity of 4.4 km/s (updated from Fishwick (2010, updated)), and an average lithospheric thickness of 80 km for northern Madagascar, the expected delay time that would be due to fossil anisotropy is 0.72 s. For central Madagascar, 0.63 s is the expected delay time for an average lithospheric thickness of 70 km. South-central Madagascar exhibits an expected delay time of 0.90 s assuming a 100 km average lithospheric thickness. Finally, the southeastern Madagascar delay time is estimated to be 0.72 s with an average lithospheric thickness of 80 km. The expected delay time due to fossil anisotropy in northern Madagascar and central and southeastern is smaller than the observed average delay time 1 s, 1 s and 0.74 s, respectively. This comparison shows that sublithospheric anisotropy is required to explain the observations in those regions. In contrast, the observed average delay time in south-central Madagascar (0.66 s) is lower than the expected delay time due to fossil anisotropy (0.99 s), which indicates that fossil anisotropy contributes to

the observations assuming the entire depth extent of the lithosphere in this region has been affected by past orogenic events, which is suggested by Reiss et al. (2016).

Northern Madagascar

The predicted splitting from EDC in northern Madagascar (Region A; Figure 1.9) aligns well with the observed homogeneous anisotropy pattern (22° misfit) and TI between depths 125 km (Figure 1.11B; 18° mean misfit) and 150 km (Figure 1.11C; 16° mean misfit). However, the general patterns of the TI axes do not change dramatically with depth, which is consistent with the small standard deviation of the observations. The tectonic setting of northern Madagascar is characterized by the highly deformed Betsimisaraka suture trending NW-SE (Figure 1.1 and Figure 1.9), which is inconsistent with the observations, predicted SKS splitting parameters, and TI. The contribution of lithospheric frozen anisotropy can be ruled out since there is only a single station in the center of this region atop the Betsimisaraka suture, and the anisotropic measurement does not align with the feature. In addition, all 9 fast directions have delay times larger than 0.5 s (∼1 s average) suggesting that the source anisotropy in northern Madagascar is deeper than the crust (Savage, 1999). However, there is a possibility that deep global mantle flow could be a source according to the direction of flow from Behn et al. (2004).

The predicted splitting derived from the mantle wind model align well with the observations for the Behn et al. (2004) global mantle flow (20° misfit, Table 3) and TI between depths 100 km (Figure S4A; 17.01° mean misfit) and Figure sB; 19.03° mean misfit). However, the predicted splitting does not align for the Forte et al. (2010) global mantle flow (40° misfit, Table 3). This result suggests that the mantle wind model from Behn et al. (2004) slightly improves the fit compared to the EDC-derived splitting alone. The good fit (20° misfit, Table 3) of the observations with the mantle wind from Behn et al. (2004) suggests that the

mantle wind from the African Superplume can generate the observed anisotropy in northern Madagascar. This interpretation is consistent with Ramirez et al. (2018).

Central Madagascar

Comparisons of EDC-derived synthetic splitting and observations in central Madagascar (Region B; Figure 1.9) indicate that the diverging EDC model only partly explains the complex pattern (35° misfit). This region is located in the Antananarivo block, which is cross-cut by the Betsimisaraka suture at the eastern side of the terrain. Only one seismic station lies on the Betsimisaraka suture (Figure 1.9) and there is a poor fit with the synthetic splitting suggesting there may be a deep source for the anisotropy, which is consistent with the estimated delay times for central Madagascar (0.88 s), or a contribution from fossil anisotropy associated with the Betsimisaraka suture for stations to the east. The comparison with TI is also poor at all depths (minimum regional misfit 33° at 200 km; Figure 1.11E), which is another indicator the EDC cannot explain all of the seismic anisotropy observations in central Madagascar and consistent with several stations having large standard deviations ($> 9°$).

Our results suggest that the E-W fast splitting in the SW corner of central Madagascar may be due to westward flow associated with the upwelling, radially diverging pattern (Figure 1.6,1.7). The mismatch (35° misfit) suggests that other effects might have contributed to the anisotropy such as multi-layer or tilted-layer anisotropy. Pratt et al. (2017) image a localized low seismic velocity zone beneath central Madagascar that they hypothesize is a thermal anomaly with a deeper, faster seismic velocity structure to the south that may be from delaminated mantle lithosphere. This feature may locally perturb the EDC, which would produce a pattern that rotates away from the flow pattern calculated in this study. The local perturbation may occur since EDC is considered weak flow that can be easily

overwhelmed by local flow driven by temperature anomalies (King and Anderson, 1998).

We also test the potential contribution of mantle wind being deflected around the thick lithosphere as a contributor to the sources of the anisotropy. We find that both models employing Behn et al. (2004) and Forte et al. (2010) boundary conditions do not provide a good fit to the data (46° and 47° average misfits, respectively, Table 3). Due to the high variability in the fast polarization directions in central Madagascar, the anisotropy observations cannot be attributed completely to EDC, global mantle flow, or fossil anisotropy alone. We suggest the anisotropy observations are likely a combination of contributions from the above processes.

Southern Madagascar

The SELASOMA profile shows complex seismic anisotropy measurements (Figure 1.1, 1.9). The measurements are approximately ∼N-S in the south-central region (Region C; Figure 1.9) and then rotate to a NE orientation in southeastern Madagascar (Region D; Figure 1.9). Asthenospheric EDC along the SELASOMA profile is controlled by southward flow that slightly rotates to the southeast, which is induced by a relatively steep lithospheric gradient between central and southern Madagascar (Region C). Our results show that the EDC can explain the sharp variation of azimuthal anisotropy along the SELASOMA profile (Figure 1.9) with an average misfit of predicted SKS splitting of 18° in south-central Madagascar and 26° in southeastern Madagascar (Region D). The comparison with TI axis (Figure 1.11) shows reasonable agreement with synthetic LPO and observations with an average of 26° in south-central Madagascar over all depths, but a less consistent fit to southeastern Madagascar with a minimum misfit of 30°.

Another potential source of the seismic anisotropy in southern Madagascar is fossil anisotropy

in the entire lithosphere as suggested by Reiss et al. (2016). In the south-central region and part of southeastern region, the geology is characterized by the Ranotsara shear zone that was active during the East African Orogeny ∼500 Ma (e.g. de Wit et al., 2001). Reiss et al. (2016) attributed the ∼N-S trending azimuthal anisotropy in the south-central region, with delay times varying between 0.4 and 1.5 s, to fossilized heterogeneities from this event. However, this interpretation is inconsistent with the rotation of seismic anisotropy along the eastern side of the profile, which suggests an additional source is needed.

In south-central Madagascar, the predicted splitting derived from the Behn et al. (2004) and Forte et al. (2010) mantle wind models are poor fits with observations (50° and 43° average misfits, respectively, Table 3). We also find relatively poor fits for both models in southeastern Madagascar (37° and 32° average misfits, respectively, Table 3).

Seismic anisotropy observations in the center of the SELASOMA profile suggest that the observations could result from an integrated anisotropy contribution of two layers or simply from EDC alone. Fossilized lithospheric anisotropy and asthenospheric anisotropy sources could coincidentally align. The relatively large observed delay times can be explained by a contribution from fossil anisotropy in the lithosphere and asthenospheric sources because anisotropy sources confined to the crust can only contribute to a small amount ($\leq$0.3 s) of the measured delay time (see Silver, 1996).

In the eastern part of the profile in the southeastern region (Region D; Figure 1.9), predicted fast directions from EDC align with a ∼NE orientation consistent with the observations. The alignment suggests that the change in anisotropy direction from the center to the east of the profile is likely due to EDC derived from the decrease of lithospheric thickness to the eastern margin of Madagascar. The relatively large misfit of 26° in the southeastern region (Region D) can be explained by several possibilities. The orientations of the fast directions at 3 stations in the middle of the region exhibit ∼N-S directions that align with

the existing Ifanadiana shear zone (see region D in Figure 1.9) suggesting a source from pre-existing structure. Alternatively, Reiss et al. (2016) suggest that APM induces LPO because the average orientation of the observed anisotropy is parallel to the Somalian plate APM. However, our model suggests that EDC can produce the observations equally well (26°) without accounting for APM or pre-existing shear zones, but the abrupt changes in fast direction in the center and west of region D can be better explained with a contribution from the pre-existing Ifanadiana Shear Zone.

A recent study by Scholz et al. (2018) supports our interpretations. Scholz et al. (2018) calculate SKS splitting observations mainly in oceanic regions around Madagascar, which is beyond the continental scope of this work, but have two measurements in southern Madagascar. One SKS splitting measurement is approximately 100 km south of the easternmost terminus of the SELASOMA profile (∼S73°E +- 20.4) and the other is approximately 250 km south of the SELASOMA profile on the eastern coast of Madagascar (∼N14°E +- 14.5). Since the two measurements on Madagascar are poorly constrained, we choose not to use them in our analysis. Consistent with our interpretation, Scholz et al. (2018) hypothesize that the source of SKS splitting observations on Madagascar may be due to sub-lithospheric material driven by EDC below a locally thin lithosphere. Scholz et al. (2018) also suggest that most of their anisotropy observations surrounding Madagascar and in the Indian Ocean poorly align with the present-day motion of the Somalian plate. They argue that the Somalian plate motion is too slow, $\sim 2.7\ cm/yr$ (e.g. Argus et al., 2011), such that the shear induced LPOs are expected to be weak (Debayle et al., 2016).

In southernmost Madagascar (Figure 1.9), two observations appear to align with the existing N-S trending shear zones (Ampanihy and Beraketa, Figure 1.2). Since only one observation aligns with the EDC-derived splitting (Figure 1.9) and derived from the mantle wind model of Forte et al. (2010) (Figure 1.10B), we propose that those observations may be sourced

from fossil anisotropy. The observation in the southernmost tip of Madagascar aligns well with the calculated splitting derived from the mantle wind model of Behn et al. (2004). We propose that this observation is sourced from sublithospheric LPO induced by the mantle wind.

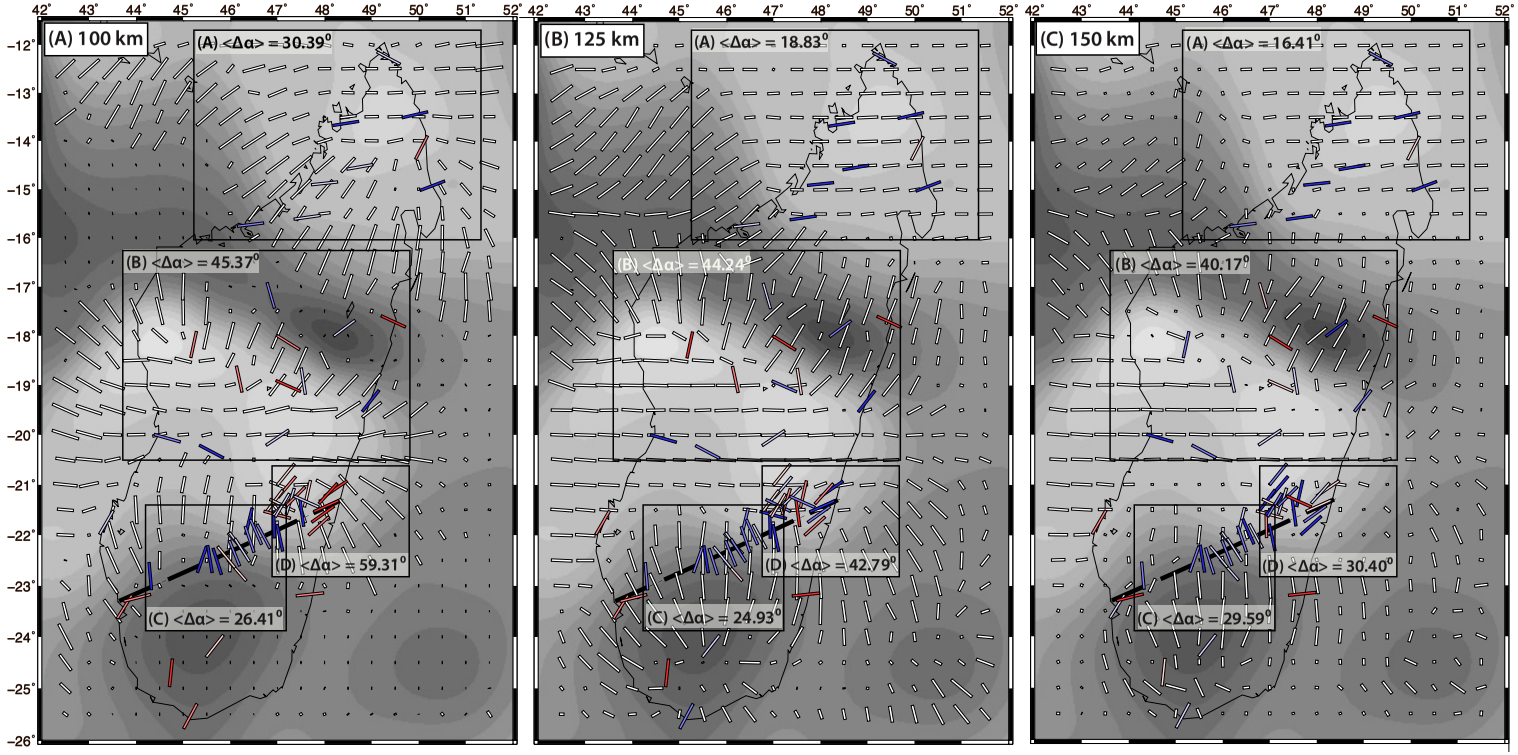

Figure 1.11: Comparison of TI axes from the EDC model and observed SKS splitting at depth of (A) 100 km, (B) 125 km (C) 150 km,(D) 175 km, (E) 200 km and (F) 225 km. The SKS splitting measurement bars are colored according to angular misfit [0° - 90°]. The background shows lithospheric thickness from updated Fishwick (2010, updated). The model output files are available at the PANGAEA repository with doi:10.1594/PANGAEA.909406.

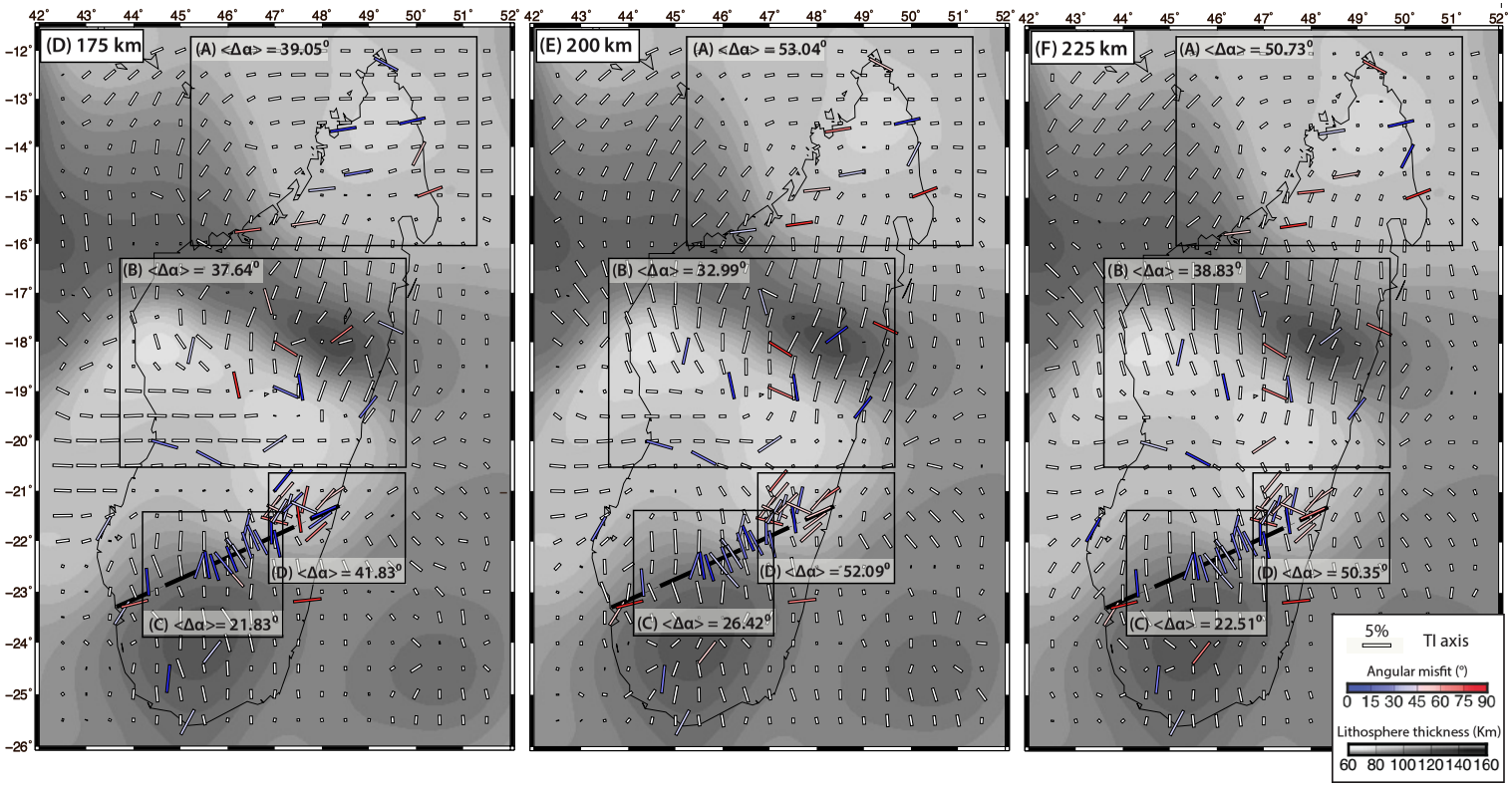

Figure 1.11: Continued.

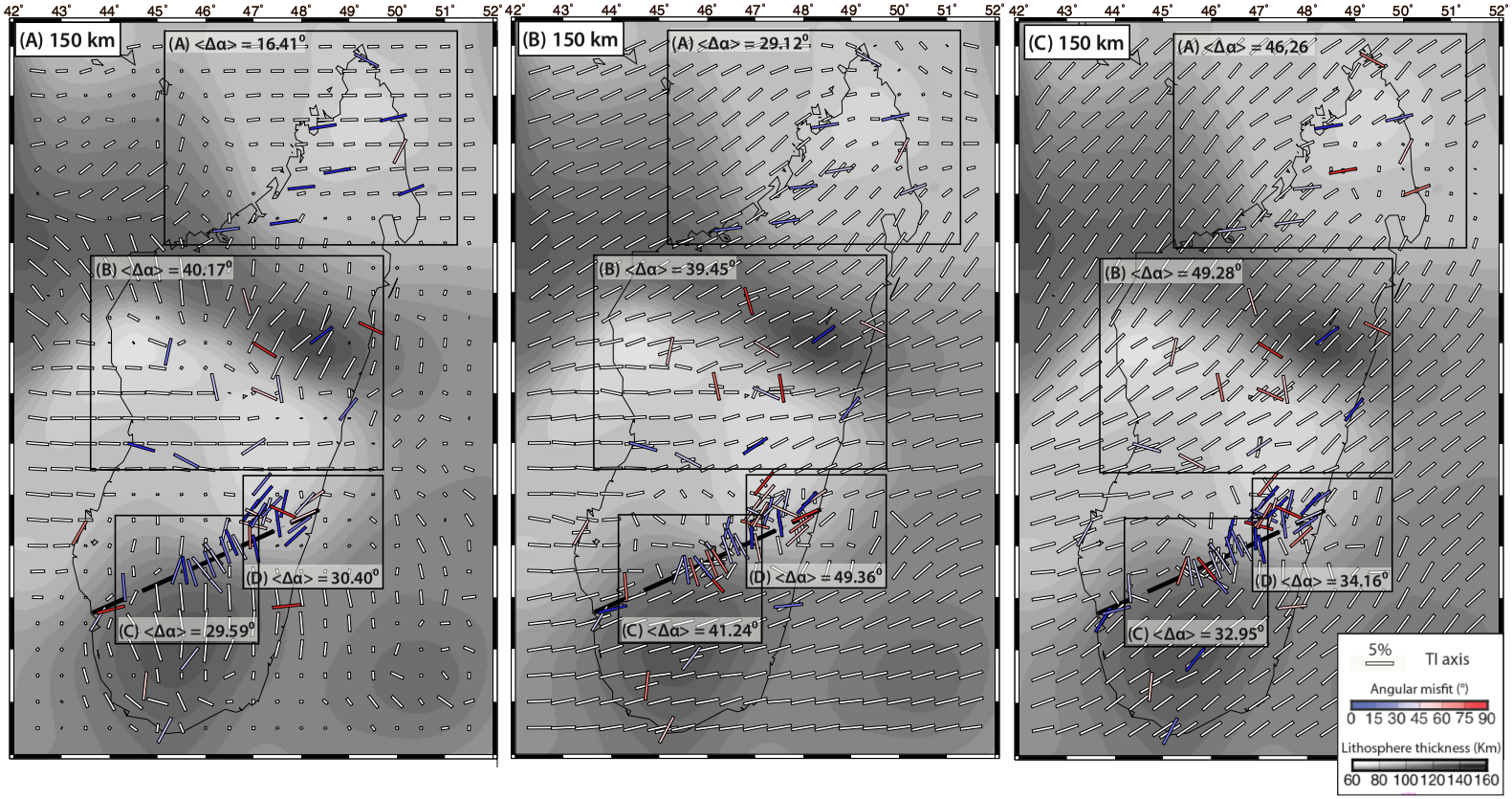

Figure 1.12: Comparison of calculated TI axes with observations at 150 km depth derived from the: A) EDC model, B) mantle wind model for Behn et al. (2004), and C) mantle wind model for Forte et al. (2010). The SKS splitting measurement bars are colored according to angular misfit [0° - 90°]. The background shows lithospheric thickness from updated Fishwick (2010, updated). The model output files are available at the PANGAEA repository with doi:10.1594/PANGAEA.909406.

1.5.2 Dominance of Edge-Driven Convection over mantle wind beneath Madagascar

The overall comparison of calculated splitting shows that EDC model produces a better fit with the observations than the mantle wind models, except in the north where the Behn et (2004) mantle wind model also reproduces the observations. The EDC model can explain the small-scale variations of anisotropy along the SELASOMA profile, but both mantle wind models do not. This result suggests that EDC dominates convective flow in the upper mantle beneath Madagascar, which implies EDC can develop within the presence of mantle wind. The lithosphere-mantle wind interactions models show that small perturbation (10 mm/yr) from global mantle flow can overwhelm the pattern of EDC to produce mostly horizontal flow. However, several studies suggest that present-day deformation in Madagascar is linked with asthenospheric upwelling (e.g Paul and Eakin, 2017; Rambolamanana et al., 1997; Rindraharisaona et al., 2013). Therefore, other processes, such as a lithospheric drip, which has been associated with asthenospheric upwelling (West et al., 2009) and potentially imaged beneath central Madagascar (Pratt et al., 2017), may enhance the development of EDC beneath Madagascar. An integrated time-dependent modeling approach that incorporates global mantle flow calculations and edge-driven convection is an area of future research. Based on the results from our approach, we suggest EDC is critical in explaining the formation of sublithospheric azimuthal anisotropy beneath Madagascar.

1.5.3 Upper mantle rheology beneath Madagascar

Knowledge of upper mantle rheology is fundamental to the study of mantle dynamics in a region. Rheological properties of sub-lithospheric continental regions may differ from those of oceanic regions (Karato, 2010). It is commonly accepted that the primary mechanisms

for controlling upper mantle deformation are diffusion and dislocation creep with diffusion creep typically dominating sub-lithospheric mantle (e.g. Karato and Wu, 1993; Nicolas and Christensen, 1987; Ribe and Yu, 1991; Zhang and Karato, 1995). While the diffusion creep mechanism tends to cause random orientations of olivine crystals, and is thus responsible for isotropic aggregates, dislocation creep produces LPO and is responsible for observed seismic anisotropy in the upper mantle (Dziewonski and Anderson, 1981; Karato and Wu, 1993). Determining the depth extent of dislocation creep and diffusion creep deformation has implications for mantle flow patterns, especially for small-scale flow in continental regions. The viscosity of both diffusion and dislocation creep flow laws depends on temperature and pressure. Dislocation creep, or power-law creep, also depends on strain rate (Podolefsky et al., 2004). Thus, the thickness of the dislocation creep layer may depend on the amount of strain rate in the asthenosphere. For example, Podolefsky et al. (2004) found that in oceanic regions, slower plate motion leads to a thinner layer of dislocation creep regime, which produces a thin and weak seismically anisotropic layer. Nevertheless, the depth extent of dislocation creep in continental regions has only been poorly constrained so far.

Here, we examine the depth where deformation changes from dislocation creep to diffusion creep using 1) observed seismic anisotropy and predicted LPO that develop at different depths and 2) the diffusion creep - dislocation creep ratio (Figure 1.13A). For northern Madagascar, the good fit between TI axes and observations at 125 km and 150 km depth and the decrease in the fit below this depth indicates a change in the rheological regime. Assuming that in that location the LPO results from strain that is accumulated along the upwelling flow beneath northern Madagascar, the asthenosphere undergoes dislocation creep deformation within the 125 km-150 km channel. LPO beneath this channel might not exist as they could potentially be erased by diffusion creep. There are a few studies that suggest that anisotropy may develop in the diffusion creep regime (Maruyama and Hiraga, 2017;

Miyazaki et al., 2013; Wheeler, 2009), but our results indicate shallow sources of anisotropy favoring its formation in the dislocation regime.

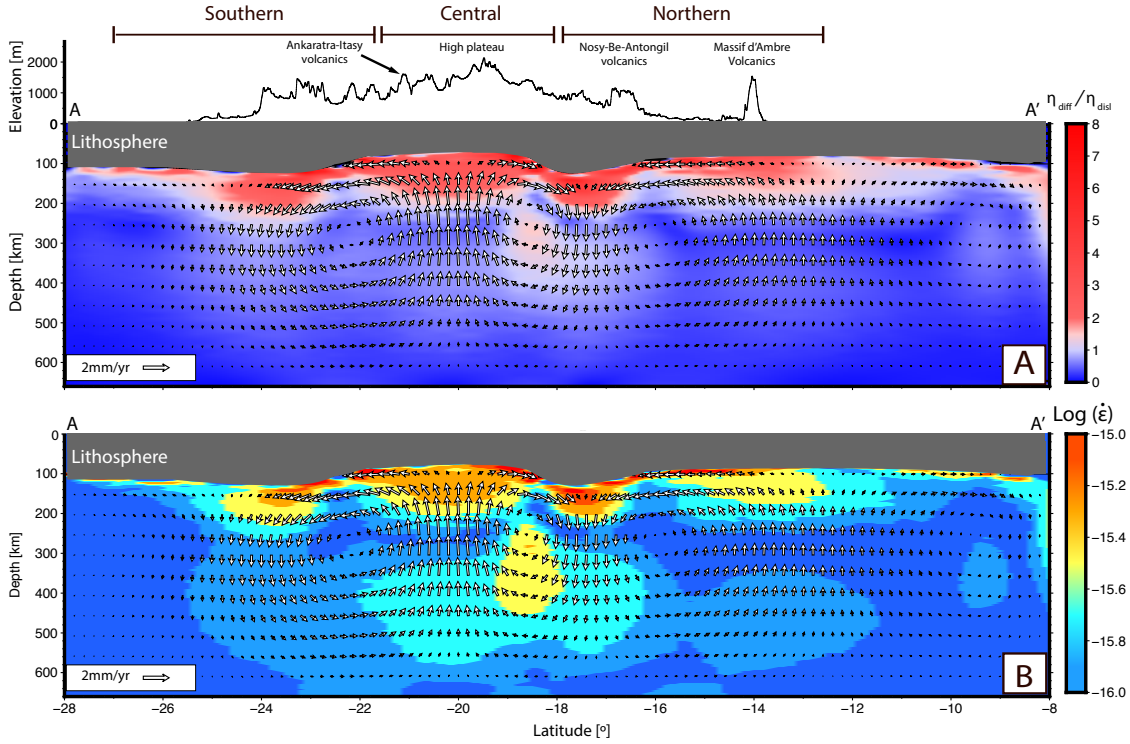

Figure 1.13: (A) Viscosity ratio (ratio of diffusion creep η_{diff} and dislocation creep viscosity η_{disl}) at the initial model stage across the long axis of Madagascar (profile AA' in Figure 1.6). Cool colors ($\frac{\eta_{diff}}{\eta_{disl}} < 1$) indicate regions dominated by diffusion creep. Conversely, warm colors ($\frac{\eta_{diff}}{\eta_{disl}} > 1$) indicate regions where dislocation creep dominates. White vectors represent the asthenospheric flow field. Dry olivine parameters are used for the viscosity calculations, which are obtained from Hirth and Kohlstedt (2003) and are listed in Table A.1. (B) Logarithmic scale of strain rate magnitude (square root of the second invariant of the strain rate tensor) across the profile AA'.

Figure 1.13A shows dominance of dislocation creep in the shallow asthenosphere beneath Madagascar, where strain rate magnitude is relatively large (Figure 1.13B). The viscosity ratio provides insight into how the EDC controls the thickness of the sublithospheric layer with predominantly dislocation creep regime along the long axis of Madagascar. In central Madagascar, where upwelling is relatively large, the thickness of the dislocation creep regime layer is up to 100 km. A similar thickness of the dislocation creep regime is found beneath the corner of thick to thin lithosphere to the north and to the south of central Madagascar. This dislocation creep channel has similar thickness, but with lower magnitude and decreases rapidly beneath northern Madagascar. The diffusion creep regime dominance is present in the shallow asthenosphere only beneath the oceanic lithosphere in the northernmost and southernmost regions of the profile because of low strain rates in these regions. In zones where diffusion creep dominates beneath oceanic lithosphere, we expect dislocation creep to be limited to the lithospheric mantle.

1.6 Conclusions

In this study, we employ 3D geodynamic models of upper mantle flow to investigate the sources of recently observed complex seismic anisotropy patterns in Madagascar and of asthenospheric rheology. Our model workflow involves three steps: 1) modeling of EDC generated by lithospheric thickness variations and modeling lithosphere-mantle wind interactions, 2) calculation of LPO that develops due to these flow calculations, and 3) prediction of splitting shear wave propagating through sublithospheric LPO. Our results show that EDC should be considered as a major source of asthenospheric upwelling beneath Madagascar. Synthetic SKS splitting directions, derived from EDC induced LPO, compare well with most of splitting measurements from Ramirez et al. (2018) and Reiss et al. (2016), except in central

Madagascar where EDC may be locally disrupted by an existing thermal anomaly imaged by shear wave tomography. However, we also find mantle wind-derived synthetic splitting from the Behn et al. (2004) model can reproduce observations in northern Madagascar as well.

Our results suggest that EDC contributes to the development of observed anisotropy, and that the role of the Somalian APM and/or global flow is minor, except in northern Madagascar where it may play a role. Upper mantle flow is partly controlled by EDC due to lateral variations of lithospheric thickness. EDC should be considered when interpreting future SKS splitting measurements including measurements across the SELASOMA profile where frozen lithospheric anisotropy exists. Our models indicate that dislocation creep extends up to 200 km into the upper asthenosphere beneath Madagascar, but also that the thickness of the anisotropic layer varies laterally. These results suggest that dislocation creep extends into the asthenosphere beneath some continental regions.

Chapter 2

The Role of Variations in Lithospheric Buoyancy Forces in Driving Deformation at the Eastern Branch of the East African Rift System

A manuscript version of this chapter was submitted to Geophysical Research Letters in 2020, with co-authors: D. Sarah Stamps (Virginia Tech) and John Naliboff (New Mexico Tech)

Despite decades of investigation, the origin of forces driving continental rifting remains highly debated. Deciphering their relative contributions is challenging due to the non-linear and depth-dependent nature of lithospheric rheology. Recent geodynamic studies of the East African Rift (EAR) report contradicting results regarding the relative contribution of horizontal mantle tractions and lithospheric buoyancy forces. Here, we use high-resolution 3D regional numerical modeling of the EAR to isolate the contribution lithospheric buoyancy forces to observed deformation. Modeled surface velocities closely match kinematic models of the Somalian Plate, Victoria Block, and Rovuma Block motions, but provide poor fit to along-rift surface motions in deforming zones. These results suggest that variations in lithospheric buoyancy forces primarily drive present-day E-W extension across the EAR, but intra-rift deformation may result from viscous coupling to horizontal asthenospheric flow.

2.1 Introduction

The East African Rift (EAR, Figure 2.1A) is the dominantly continental portion of the East African Rift System, which separates the Nubian and Somalian Plates and is the largest continental rift on Earth. The EAR is traditionally divided into three distinct rift segments: the northern EAR (Afar region), the Eastern Branch, and the Western Branch. Its spatial extent, heterogeneous lithospheric structure, and variable rates of extension across the EAR produce a wide range of deformation styles. At present, the origin of forces driving extension across the EAR remains highly debated. The absence of regional slab-pull forces requires dominant contributions from variations in lithospheric buoyancy and horizontal mantle flow. Variations in lithospheric buoyancy arise from a combination of changes in lithospheric structure (composition, geothermal gradients) and surface topography (Fleitout, 1991; Fleitout and Froidevaux, 1982; Flesch et al., 2000; Jones et al., 1996), with the latter partially supported by vertical mantle flow (i.e. dynamic topography; Flesch et al., 2007). When isostatic compensation is assumed, variations in lithospheric buoyancy can be quantified through the integration of lithostatic pressure to a compensation depth (i.e., gravitational potential energy GPE), with regions of locally high GPE undergoing extension (e.g. Coblentz and Sandiford, 1994). While variations in lithospheric buoyancy generate internal stresses driving deformation, mantle flow gives rise to both vertical and horizontal tractions acting at the base of the lithosphere. The magnitude of horizontal tractions acting on the base of the lithosphere is a function of both short- and long-wavelength convection patterns and the viscosity at the lithosphere-asthenosphere boundary, with deep and cold continental roots producing stronger coupling and higher stress magnitudes (Conrad and Lithgow-Bertelloni, 2006). New GPS observations, combined with azimuthal seismic anisotropy and strike-slip focal mechanisms, provide insight into the balance of these two forces driving deformation across the EAR (Figure 2.1A,B). Several GPS stations positioned within rift segments mea-

sure non-transient, secular surface motions between the Nubian and Somalian Plates that are rift-parallel, or oblique to the E-W extension across the broader rift system (Figure 2.1A). In particular, GPS velocities corrected for volcanic deformation in the Kivu Rift exhibit NNE trajectories (Ji et al., 2017; Stamps et al., 2018), while multiple GPS stations in the Eastern Branch and northern EAR exhibit a NE trend. In addition, strike-slip focal mechanisms within multiple rift segments (Figure1b; Dziewonski et al., 1981; Ekström et al., 2012) provide evidence for strain partitioning reflecting rift-parallel deformation. N-S oriented azimuthal seismic anisotropy measurements beneath the Kenya Rift, Uganda, and Ethiopia (Figure 1b) likely reflects the northward mantle flow associated with the African Superplume (Ballmer et al., 2015). We hypothesize that the observed northward component of surface motions within rift segments may be the result of viscous coupling to northward mantle flow associated with a single, or multiple plumes, and that the forces driving E-W opening of the Nubia-Somalia plate system are dominated by lithospheric buoyancy forces. Here, we use state-of-the-art 3D thermomechanical models of the EAR to isolate the contribution of variations in lithospheric buoyancy to observed deformation patterns and test this hypothesis. Prior studies of deformation within the EAR have been limited due to a lack of 3D thermomechanical modeling, although recent 3D thermomechanical experiments (Koptev et al., 2018a,b) suggest that the interactions of plumes with the lithosphere contribute to both rift initiation and evolution along parts of East Africa through lithospheric weakening and melt migration. However, these studies do not address the distinct role of the lithospheric buoyancy forces in driving present-day deformation across the EAR. Furthermore, existing studies that examine the role of lithospheric buoyancy forces have relied on thin-sheet or shell approximations to model lithospheric deformation. While such approximations are computationally inexpensive and thus allow for conducting extensive sensitivity analyses, they fail to capture the non-linear and depth-dependent nature of lithospheric rheology that affects transmission of both internal buoyancy forces and viscous coupling to horizontal

mantle tractions (e.g. Naliboff et al., 2012). In this work, we characterize the contribution of lithospheric buoyancy forces in driving deformation across East Africa and surroundings, centered on the southern Eastern Branch. We developed a 3D regional model that comprises the lithosphere-asthenosphere system with topography imposed at the model surface and lateral density variations in the crust and mantle down to a compensation depth of 100 km. This model allows for estimates of surface motions to be solely driven by lithospheric buoyancy forces. To assess the contribution of lithospheric buoyancy forces to the present-day extension across East Africa, we compare several model outputs with previous modeling results (gravitational potential energy, geodetic strain rates, surface motions from kinematic modeling) and GPS data.

2.2 Modeling Lithospheric Deformation of the East African Rift

We calculate dynamic velocities, continuous strain rates, and deformation style solely driven by lithospheric buoyancy forces for East Africa and surroundings. We use the open-source finite element code ASPECT (Bangerth et al., 2015, 2020; Glerum et al., 2020; Kronbichler et al., 2012; Naliboff et al., 2020) to model present-day (instantaneous) deformation driven by lithospheric buoyancy forces. Using ASPECT, we solve for velocity from the Stokes system of equations including the Bousinessq equation of momentum and conservation of mass for an incompressible Newtonian fluid (see Appendix A). The surface deformation is calculated by simulating a regional 3D thermomechanical model of the lithosphere-asthenosphere system that encompasses the EAR centered on the Eastern Branch. The model domain is 5300×3300×660 km in the East, North, and radial (depth) directions, consisting of upper, middle, and lower crustal layers, a mantle lithosphere layer, the asthenosphere, and the 410-

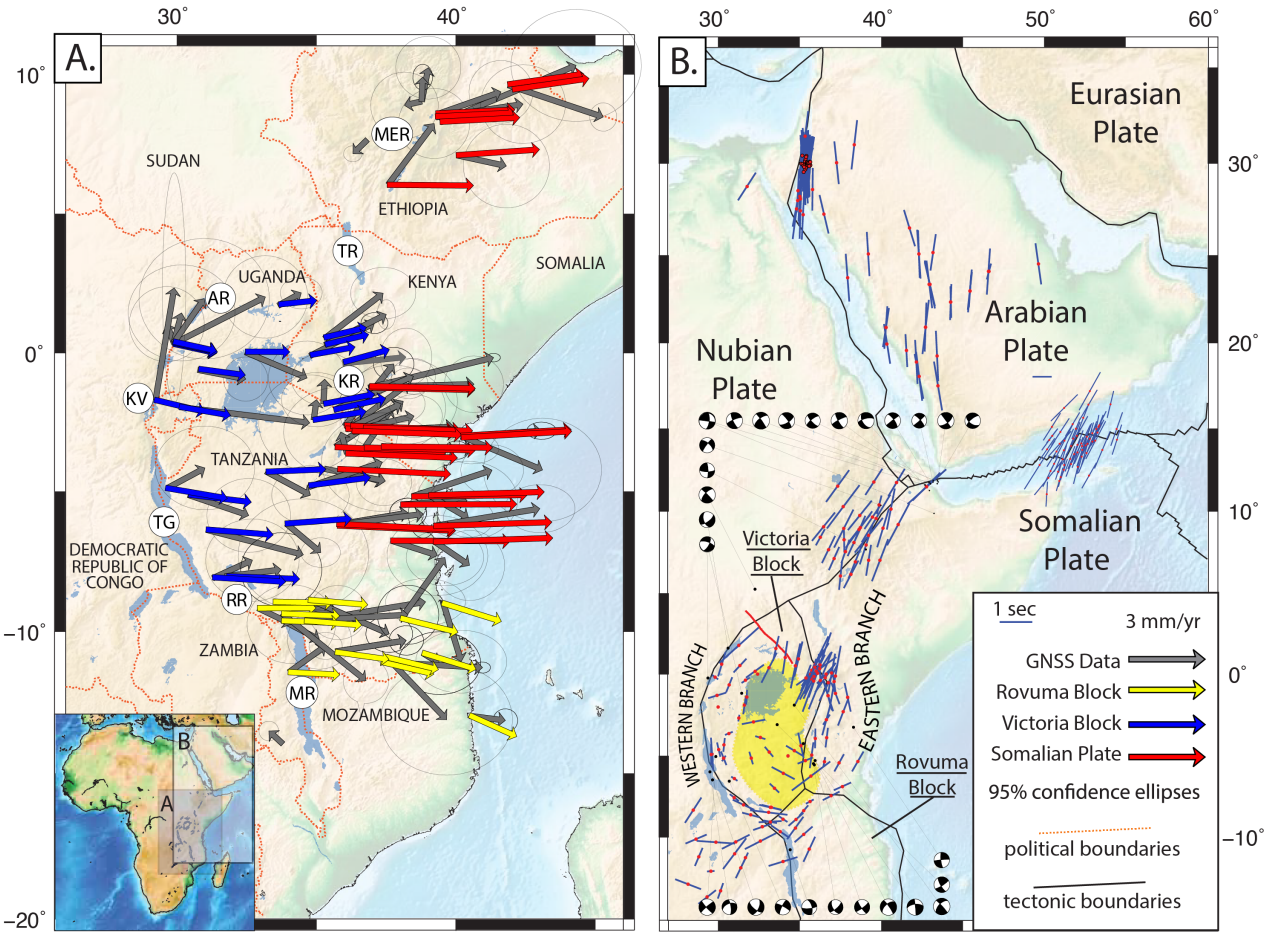

Figure 2.1: a) GPS velocities along the East African Rift (EAR; Stamps et al., 2018; gray vectors with 95% confidence ellipses). Red, blue, and yellow vectors are kinematic models from Saria et al. (2014) for the Somalian Plate, the Victoria Block, and the Rovuma Block, respectively. Orange lines are political boundaries. Several rifts are defined: TG = Tanganyika Rift, RR = Rukwa Rift, AR = Albertine Rift, MER = Main Ethiopian Rift, TR = Turkana Rift, KR = Kenya Rift, MR = Malawi Rift, and KV = Kivu Rift. b) Observed SKS splitting and strike-slip focal mechanisms along the EAR. The shear-wave splitting measurements are shown as blue bars with red circles showing the associated seismic station location. Black dots indicate earthquake locations where strike-slip focal mechanisms are observed (GCMT; Dziewonski et al., 1981; Ekström et al., 2012).

660 km transition zone (Figure 2.2). We employ quadratic finite elements for the temperature fields, compositional fields, and velocity fields with a resolution of 40×25×5 km. Our modeling approach includes the lithosphere, asthenosphere, and the transition zone down to 660 km depth, a non-linear visco-plastic rheology, and initial conditions (temperature, density) constrained by synthetic lithospheric structure based on average lithospheric thicknesses of the key tectonic regions derived from averages of the lithospheric models LITHO1.0 Pasyanos (2013), Fishwick (2010, updated), and Emry et al. (2019). For cratonic regions (Tanzania Craton and Congo Craton) the lithospheric thickness is 150 km, 70 km for the Eastern Branch, 90 km for the Western Branch, and 100 km thick for mobile melts. We also impose 50 km thickness for oceanic ridges and 100 km thickness for oceanic lithosphere. The model is centered on the southern Eastern Branch such that the deforming regions are distant from the side boundaries to avoid boundary effects. The mechanical boundary conditions are free slip on all faces of the model, except at the bottom boundary, where it is fixed. Crustal density variations are derived from CRUST1.0 (density and thicknesses for lower, middle, and upper crust; Laske et al., 2013) and ETOPO1 (Amante and Eakins, 2009) data sets into the 3D model. The lithospheric temperature structure is a steady-state conductive geothermal gradient characteristic of the continental lithosphere, which is constrained using estimates of regional lithospheric thickness and surface heat flow of the key tectonic regions (cratons, mobile belts, and rifts; Table A.1). Isostatic compensation is enforced through adjustments to the mantle density (i.e. Pratt isostasy) down to 100 km, with a constant value of 3300 kg/m3 assigned from the compensation depth to 660 km. We assume that all densities are independent of temperature. This approach allows for neglecting buoyancy driven mantle flow that might arise from plumes (e.g. Koptev et al., 2018a,b) or lithospheric modulated convection (e.g. Njinju et al., 2019a; Rajaonarison et al., 2020) in the sub-lithospheric regions. While the geothermal gradient does vary within our model, temperature variations only affect the rheological structure. The rheological model of the crust combines non-linear

dislocation creep (dry quartzite; Gleason and Tullis, 1995) with plastic failure. The mantle lithosphere rheological model follows olivine dislocation creep (Hirth and Kohlstedt, 2003) combined also with plastic failure, while a composite rheology of dry olivine is used in the sublithospheric mantle (Jadamec and Billen, 2010). In the deforming regions, defined by Stamps et al. (2018), a plastic strain weakening factor for cohesion and friction is applied to the lithospheric viscosity to promote strain localization. Details of the numerical experiment, including the governing equation, the density variations, the initial temperature field, and the applied rheology, are described in the Appendix B.

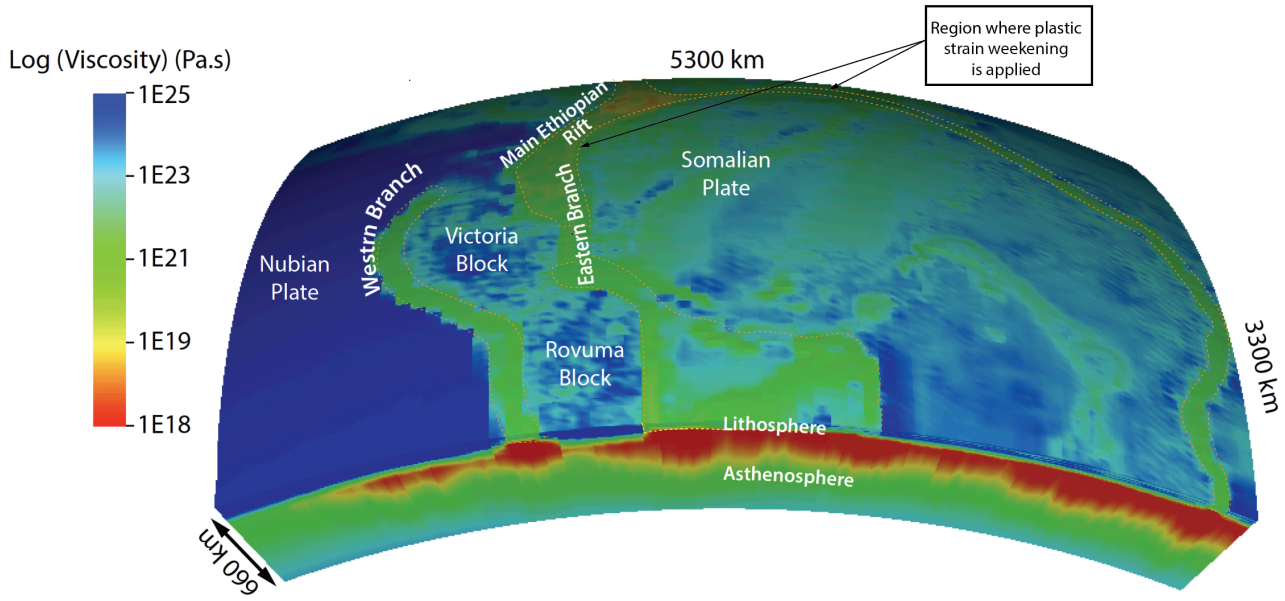

Figure 2.2: 3D thermomechanical lithosphere-asthenosphere system for the EAR and surroundings. The viscosity is shown in a logarithmic scale. In the lithosphere, regions with viscosity between $10^2$3-$10^2$5 Pa.s are effectively undeformed (i.e., low strain rate) , whereas regions with viscosity between 10^{19}-10^{21} Pa.s have the highest rates of near-surface deformation . The latter regions largely fall within branches of the EAR where zones of reduced brittle strength were imposed, which promote strain localisation.

2.3 Results and Discussions

2.3.1 Lithospheric Buoyancy Forces and Rift Strength

To provide a point of comparison with previous 2D studies of GPE-driven deformation in the EAR, we calculate regional GPE patterns using the lithostatic pressures from the 3D simulation. Following previous work that is consistent with our imposed isostatic compensation depth (e.g. Flesch et al., 2001; Ghosh et al., 2009; Jones et al., 1996; Stamps et al., 2014), we define GPE as the vertically integrated lithostatic pressure from a depth of 100 km to the surface and compare our results with Stamps et al. (2014). The first-order patterns and magnitudes of the GPE from this study compare well with Stamps et al. (2014), which notably uses a lower resolution model of crustal thickness (CRUST2.0; Bassin, 2000) and topography (ETOPO5; Edwards, 1989; Figure 2.3A). Our modeled GPE distribution ranges from 1.52-1.66 TN/m in the African mainland to 1.40 - 1.52 TN/m in the oceanic basin (Figure 2.3B), whereas in Stamps et al. (2014) the same regions have values of 1.54-1.58 TN/m to 1.46-1.52 TN/m. The residual between this study and Stamps et al. (2014) is between 0.05-0.1 TN/m (Figure 2.3C), which accounts for <10% of the total GPE and likely reflects variations in the assumed crustal structure and surface topography. Notably, the influence of surface topography is clearly evident in the shorter-wavelength GPE variations observed in this study. However, given that the depth-integrated lithospheric buoyancy driving forces are similar to previous studies, the model design provides a template for analyzing the effects of vertically- and laterally-varying lithospheric structure on surface deformation patterns.

To test whether the available lithospheric buoyancy forces are capable of causing lithospheric rupture at the deforming zones, we consider six scenarios with variable lithospheric thickness and randomly reduced brittle strength (cohesion, friction) within the Eastern and Western Branches (Table s1). The reductions in brittle strength within the rift zones are achieved by

applying an initial randomized plastic strain field between values of 0.5 and 1.5, over which the cohesion and angle of internal friction linearly weaken by a factor (ϕ_{wf}, Table s1). The imposed lithospheric thickness in the rifts varies by up to 20 km between models (Western Branch 80100 km, Eastern Branch 60-80 km), which modifies the geothermal gradient and resulting viscosity in ductile portions of the lithosphere. For each simulation, the vertically integrated lithospheric strength is compared to the depth-averaged GPE, and the resulting plate and block rotations are compared with the kinematic predictions of Saria et al. (2014).

The available forces acting on the rifts are equal to the GPE averaged over 100 km, which ranges between 15.6-16.8 MPa (Figure 2.3D). For the case of intermediate rift lithospheric thicknesses (Western Branch 90 km, Eastern Branch 70 km), the available driving forces only exceed the lithospheric strength (Figure 2.3E) when the friction and cohesion are reduced by a factor of 0.01 (Model 1, Table s1). The excess of the available driving forces with respect to lithospheric strength is supported by the positive residual (Figure 2f). While rifting occurs in this case, reducing the brittle weakening factor sufficiently increases the lithospheric strength to prevent rifting and resulting plate velocities exhibit a poor fit to kinematic predictions (Models 2-3, Table s1).

While decreasing the lithospheric thickness by 10 km within both rift segments enables rifting to occur for brittle weakening factors of 0.1 and 0.01, both models (Models 4-5, Table s1) exhibit the worst fit to the kinematic predictions. Increasing the lithospheric thickness by 10 km and using a brittle weakening factor of 0.01 (Model 6) improves the RMS misfit significantly relative to Models 4 and 5, although the misfit values are roughly equivalent to Models 2 and 3 where rifting fails to occur. As Model 1 provides the best first-order match to the observations of plate motion, we hereby use it for analysis of individual regions.

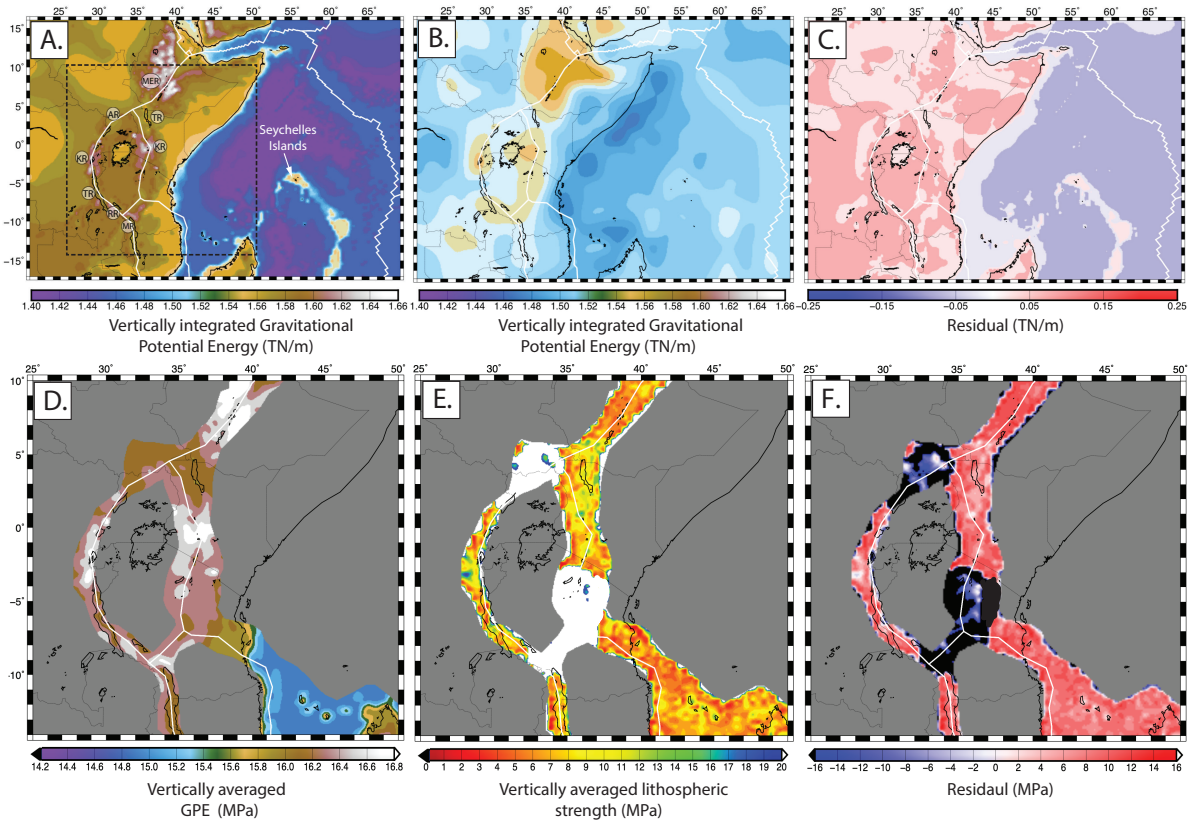

Figure 2.3: a, Calculated GPE for the EAR from this study constrained by CRUST1.0 (Laske et al., 2013) and ETOPO1 Amante and Eakins, 2009 topography data set with an isostatically compensated lithosphere of 100 km, from this study. Highest GPE are around the rifts. b, GPE constrained by CRUST2.0 (Bassin, 2000) and ETOPO5 (Edwards, 1989) from Stamps et al. (2014) for an isostatically compensated lithosphere at 100 km depth. c) The GPE residual between (a) and (b). Plate and block boundaries are from D. S. Stamps (2008). d, Vertically averaged GPE (averaged over 100 km) acting on the deforming regions of the EAR e, Vertically averaged lithospheric strength for Model 1 (Table 1). f, Residual between (d) and (e).

2.3.2 Rigid Plate Rotation

To further test if lithospheric buoyancy forces drive present-day deformation across East Africa and surroundings, we compare our dynamic velocity estimates from our preferred model with kinematic predictions of surface motions within zones of rigidity (Saria et al., 2014; Figure 2.4A) and GPS velocities in intra-rift zones (Stamps et al., 2018; Figure 2.4B).

We also quantitatively compare the continuous strain rate magnitude (second invariant of strain rate) and qualitatively compare the style of deformation with the geodetic strain rate model of (Stamps et al., 2018; Figure 2.5D,E). Surface velocities predicted by the block kinematic model of Saria et al. (2014) for the Somalian Plate, Victoria Block, and Rovuma Block are well reproduced by our dynamic velocities with an overall RMS misfit of 1.4 mm/yr and angular misfit of 8° (Figure 2.4A). Since the dynamic velocities of the Nubian Plate are nearly zero, the velocities of the Somalian Plate, Victoria Block, and Rovuma Block can be regarded as in a Nubian-fixed reference frame. For the Somalian Plate, the dynamic velocities have a clockwise rotation at rates of ∼2-6 mm/yr decreasing from north to south, while the kinematic velocities are slightly slower at 2-5 mm/yr. The RMS value for the Somalian Plate in comparison with predicted velocities from Saria et al. (2014) is 1.8 mm/yr and the angular misfit is 10°. The clockwise rotation of the Rovuma Block in our region of study predicted by Saria et al. (2014) is on the order of 2 mm/yr and is consistent with our dynamic velocities with an RMS of 0.2 mm/yr and an angular misfit of 10°. For the Victoria Block, the dynamic velocity is ∼1.4 mm/yr with a counterclockwise rotation decreasing from south to north, which is also consistent with the kinematic predictions. The RMS misfit is 0.5 mm/yr and the angular misfit is 5°. As opposed to clockwise rotation of the Somalian Plate and the Rovuma Block with respect to Nubia, the counterclockwise rotation of the Victoria Block is an intriguing characteristic of the kinematics of the EAR (Fernandes et al., 2013; Glerum et al., 2020). However, many authors suggest contradicting explanations of its driving mechanism. Earlier studies attribute this counterclockwise rotation of the Victoria Block to plume-lithosphere interactions, with northward mantle flow pushing the keel of the Tanzania Craton positioned within the Victoria Block (Calais et al., 2006). However, in more recent studies, Glerum et al. (2020) used a numerical modelling approach to demonstrate that the rotation is due to edge-driven mechanisms caused by strong rheology at northernmost Western Branch and southernmost Eastern Branch. This new finding implies that variations

in lithospheric strength across the rifts control the rotation and only the far-field extensional forces are required. Our result is consistent with the edge-driven mechanism as our model incorporates the strong rheology at northernmost Western Branch and southernmost Eastern Branch where no plastic strain weakening is applied. Lithospheric buoyancy forces acting on laterally varying lithospheric strength causes the Victoria Block to rotate counterclockwise without the need for sublithospheric forces.

2.3.3 Intra-Rift Surface Motions

Overall, there is poor agreement between the dynamic velocities and GPS observations within the deforming zones (Figure 2.4B), with an overall RMS misfit of 2.9 mm/yr and angular misfit of 70°. In the Main Ethiopian Rift (Region A; 2.4B), there is an alignment between the dynamic and GPS velocities at 5 stations and misalignment at 3 stations yielding a poor angular misfit of 66°. The dynamic velocities are twice as fast as the observations along the Main Ethiopian Rift with an RMS misfit of 2.6 mm/yr. The fit within the southern Eastern Branch is variable. Within the Kenya Rift, there is a good agreement in the northern segment (Region B; Figure 2.4B) with an RMS misfit of 1.5 mm/yr and angular misfit of 12°0, but the fit worsens in the central segment (Region C; Figure 2.4B) where the dynamic velocities are oriented in the SE direction and the GPS velocities are oriented in the NE direction (RMS misfit of 1.3 mm/yr and angular misfit of 74°0). In the southern segment of the Eastern Branch (Region D; 2.4B), there is a good fit with GPS data with an RMS misfit of 1.1 mm/yr and angular misfit of 8°0. In the central and northern Western Branch (Region E; Figure 2.4B; Kivu Rift and Albertine Rift), dynamic velocities are near zero, but the GPS velocities are up to 4 mm/yr and parallel to the rift with northward directions, yielding an RMS misfit of 2.1 mm/yr and angular misfit of 114^o. For stations located in the Rukwa Rift and northern Malawi Rift, the dynamic velocities are mostly parallel to the ∼E-W GPS

velocity directions, but with lower magnitudes, yielding an RMS misfit of 0.8 mm/yr and angular misfit of 20°0.

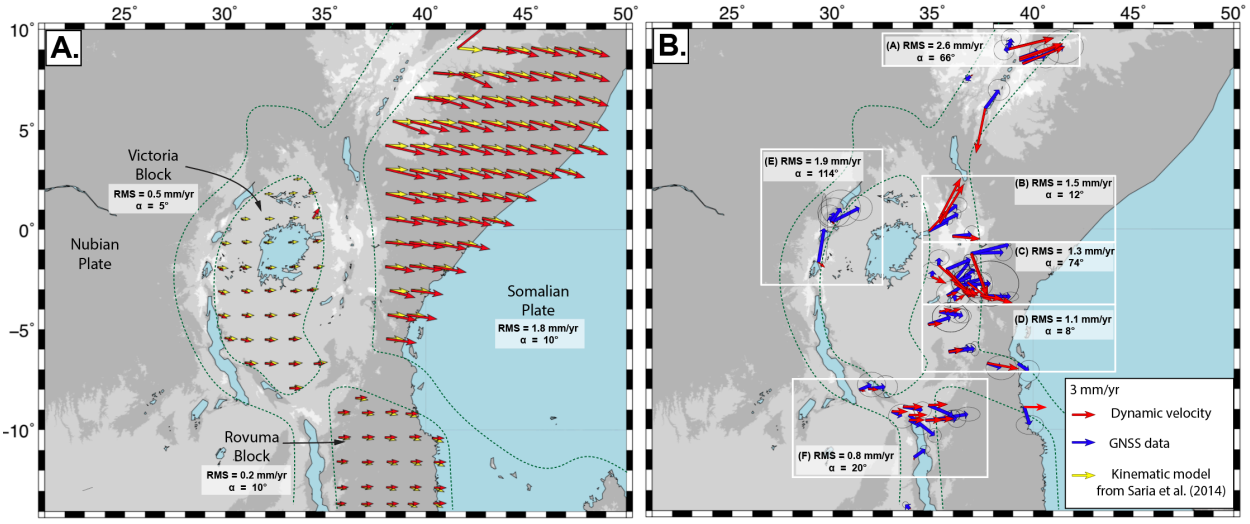

Figure 2.4: Surface velocity comparison. a, Dynamic velocities driven by variations in lithospheric buoyancy forces (red vectors) and kinematic predictions from the Saria et al. (2014) model (yellow vectors) within the Somalian Plate, the Victoria Block, and the Rovuma Block. b, Dynamic velocities (red vectors) and GPS data from (Stamps et al., 2018, blue vectors) within the deforming zones.

2.3.4 Strain Rates in Deforming Zones

For the comparison of vertically integrated strain rate magnitude through the lithosphere with the geodetic strain rate model of Stamps et al. (2018), we find that both models have similar patterns but slightly differ in magnitudes (Figure 2.5A,B). Similar to the geodetic strain rate model, the estimated vertically integrated strain rate magnitude from our model is spatially varying across the rifts. The highest magnitudes (0.9-1.3*10-8 yr-1 , Figure 4a) are found in the the Main Ethiopian Rift, which are slightly lower than the geodetic strain rate (0.9-2.0*10-8 yr-1 , Figure 4b), producing residuals between 0-2.0*10-8 yr-1 (Figure 2.4C). Along the Eastern Branch, our model predicts relatively large strain rate magnitudes of 1-

2*10-8 yr-1 in the Kenya Rift, but they are relatively low (0.8-1*10-8 yr-1) in the Turkana Rift. In the Main Ethiopian Rift and the Eastern Branch, variations from high to low strain rates correspond to regions from high to low topography in this work. Along the Western Branch, the dynamic strain rates are mostly lower 0-0.8*10-8 yr-1 than the geodetic strain rates 0.8-2*10-8 yr-1. The highest residuals, ranging from 1.5 to 2*10-8 yr-1, between the dynamic strain rates and the geodetic strain rates are found along the Tanganyika Rift, the Rukwa Rift, and the northern Malawi Rift. The relatively low dynamic strain rates with respect to geodetic strain rates, along the Main Ethiopian Rift, in the central segment of the southern Eastern Branch, and along the Tanganyika Rift, the Rukwa Rift, and the northern Malawi Rift, indicate lithospheric buoyancy forces are not sufficient to produce the observed strain rate in the deforming zones of the EAR. Predicted patterns of deformation style (compression, extension, strike-slip) patterns (Figure 2.4D) largely match those predicted by the geodetic strain rate model (Figure 2.4C). The deformation style exhibits dominantly extensional deformation with a component of strike-slip across the EAR, except at the northernmost Western Branch and the southernmost Eastern Branch where deformation is compressive. These regions of compression fall within imposed cratonic domains, which act as relatively rigid blocks due to the lower geothermal gradient and that plastic strain is not imposed. A minor difference occurs at the central segment of the Eastern Branch where the dynamic model predicts dominantly extensional deformation whereas the geodetic-based deformation style exhibits sparse regions of compressional deformation. This comparison of the predicted and geodetic deformation styles emphasize the predominance of the lithospheric buoyancy forces in driving E-W extension across the EAR.

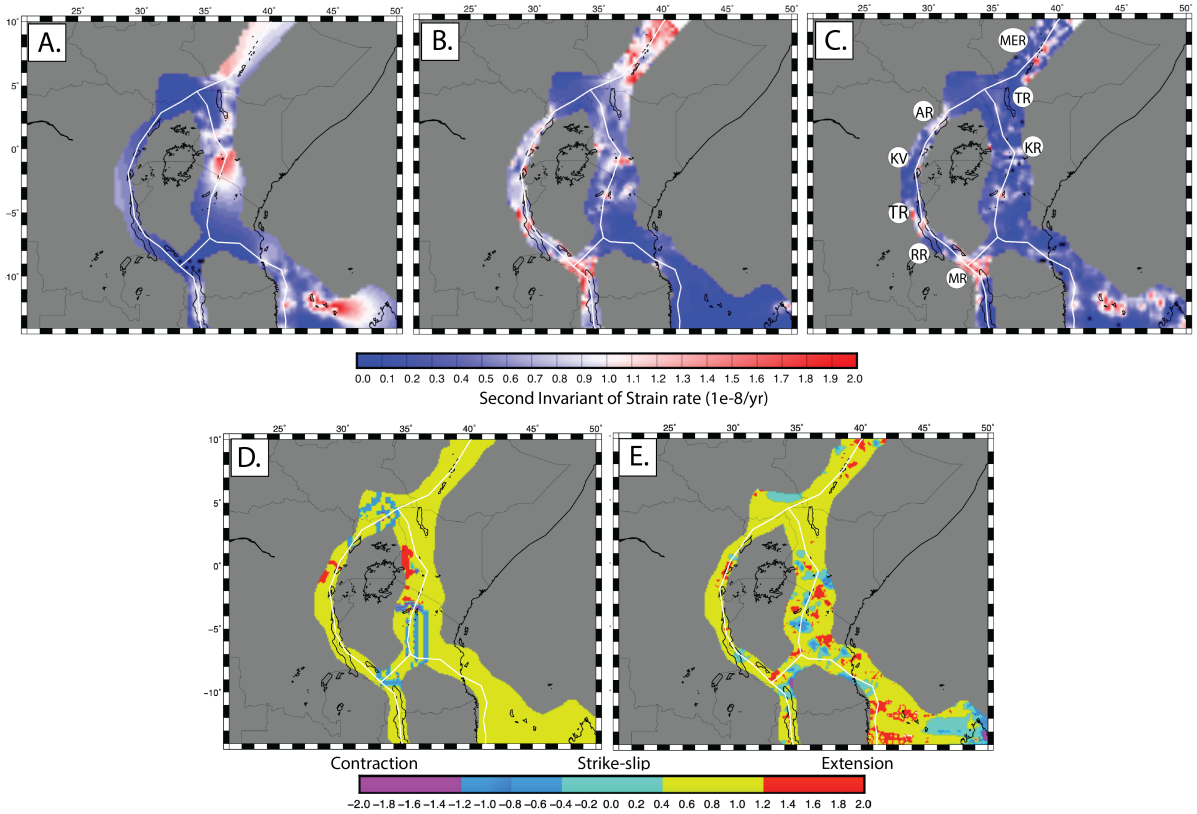

Figure 2.5: (a-c) Strain rate magnitude comparison: a) Modeled vertically averaged dynamic strain rate magnitudes driven by lithospheric buoyancy variations, from this study, b) geodetic strain rate magnitudes from Stamps et al. (2018). c) Residual strain rate magnitudes. (d-f) Strain rate style comparison: d) dynamic strain rate style, f) geodetic strain rate style form Stamps et al. (2018).

2.4 Conclusions

Our 3D thermomechanical models of the EAR demonstrate that variations in lithospheric buoyancy forces drive E-W extension across East Africa that results from rigid block rotation. These findings are consistent with previous 2D models of regional deformation patterns (Stamps et al., 2015, i.e.), but contradict additional 2D studies that suggest horizontal tractions at the base of the lithosphere contribute significantly to observed large-scale deformation patterns across the EAR (Bird et al., 2008; Ghosh et al., 2013; Kendall and

Lithgow-Bertelloni, 2016; Kusznir and Park, 1984). Our comparisons with intra-rift GPS velocities demonstrate lithospheric buoyancy forces cannot explain all surface motions within the deforming zones. This work suggests that, across East Africa and surroundings, viscous coupling to horizontal mantle flow may play a role in driving deformation in regions that are relatively weak compared to rigid block rotations controlled by lithospheric buoyancy forces.

Chapter 3

A Geodynamic Investigation of Plume-Lithosphere Interactions Beneath the East African Rift

A modified manuscript version of this chapter is in preparation for submission to G-cubed (Journal of Geophysical Research), with co-authors: D. Sarah Stamps (Virginia Tech), John Naliboff (New Mexico Tech), Andrew Nyblade (Pennsylvania State University), and Emmanuel Njinju (Virginia Tech)

Constraining the origin of forces that drive continental rifting remains a highly debated and unresolved question within geodynamics. The East African Rift (EAR) provides an ideal natural laboratory to examine the relative role of plate driving forces because only two of three major forces acting on the system since it is surrounded by spreading ridges: lithospheric buoyancy forces and horizontal mantle tractions. Recent geodynamic investigations suggest widely varying estimates for the relative contributions of lithospheric buoyancy forces and horizontal mantle tractions to observed deformation patterns. Here, we employ high-resolution 3D thermo-mechanical models of the EAR, using the open source code ASPECT, to test the hypothesis that: 1) anomalous, rift parallel surface deformation observed by GNSS data in the EAR are driven by viscous coupling to northward mantle flow associated with the African superplume and 2) mantle flow driven by African superplume is the

dominant source mechanism of observed N-S and NNE azimuthal seismic anisotropy beneath the EAR. We explore two types of mantle flow: (1) multiple plumes model constrained by shear wave tomography and (2) a superplume model derived from the multiple plumes model but with northward mantle wind imposed as boundary conditions to simulate flow from the superplume. Using ASPECT, we calculate surface deformation driven by both lithospheric buoyancy forces and mantle flow that is compared with surface motion constraints (GNSS and plate kinematics). We also calculate Lattice Preferred Orientation (LPO) that develops along pathlines of both models and compare them with observations. We find a better fit with observations and dynamic surface velocities with lithospheric deformation coupled with the superplume mantle flow model than with the multiple plume models. We find also a relatively better fit spatially between observed seismic anisotropy and calculated LPO with the superplume model beneath northern and central EAR where the superplume is proposed to be shallowest. Our results suggest that the viscous coupling to the lithosphere to northward mantle flow associated with the African superplume drives most of the rift parallel deformation in the EAR and is the dominant source of the observed LPO beneath the EAR.

3.1 Introduction

Continental rifting is an important geodynamic process during which the Earth's lithosphere undergoes continuous stretching resulting in continental break-up and the formation of new oceanic basins. In the past few decades, many geophysical studies have been carried out to elucidate the driving forces of continental rifting to advance our understanding of rift initiation and evolution. Extensional stresses responsible for continental rifting can be classified into two categories: 1) convective mantle generates horizontal tractions at the base of the lithosphere that drive extension and 2) variations in lithospheric buoyancy forces that arise

form topography and density variations generate extension.

The EAR is diverging the Nubia-Somalia plate system with approximately ∼E-W extension as shown by kinematic model (Stamps et al. 2020; Figure 3.1A). The EAR is driven by variations in lithospheric buoyancy forces attributed mainly to the unusually high to topography (higher than 1000 m above see level) known as the African Superswell (Nyblade and Robinson, 1994) of the EAR (Figure 3.1A) and to density variations withing the lithosphere (e.g. Coblentz and Sandiford, 1994; Stamps et al., 2014, 2015). However, other studies propose horizontal mantle tractions are crucial to the force balance that causes East African to rupture (e.g. Ghosh and Holt, 2012; Kendall and Lithgow-Bertelloni, 2016). In our recent study (Rajaonarison et al., under review, GRL), using 3D thermomechanical modeling we isolated the contribution of lithospheric buoyancy forces to the present-day deformation in the EAR. We found that the E-W extension of the EAR is dominated by lithospheric buoyancy forces and that additional forces, such as viscous coupling to mantle flow, are needed to explain the anomalous observed northward surface motions within the deforming zones as shown by GNSS/GPS velocities in (Figure 3.1A, Stamps et al. (2018)) and strike-slip focal mechanisms observed at multiple branches of the rift (Figure 3.1B; Dziewonski et al. (1981); Ekström et al. (2012)). In this work, we focus on plume-lithosphere interactions as an explanation for the rift-parallel deformation observed along the EAR.

Numerous seismic tomography studies have imaged low velocity anomalies beneath the EAR and associated them with the presence of plumes. However, interpretations of these low velocity anomalies in term of plumes remain controversial with two main end-member plume models (Figure 3.1C,D) are often evoked. The first model attributes the low velocity anomalies beneath the EAR as originating from multiple plumes (Figure 3.1C) beneath the EAR (e.g. Camp and Roobol, 1992; Chang and Van der Lee, 2011; Ebinger and Sleep, 1998; George et al., 1998; Montelli et al., 2006). The second model is known as the African superplume

(Figure 3.1D), which consists of a large single low velocity anomaly that penetrates the transition zone, originating from the core-mantle boundary situated beneath South Africa and flows northeastward beneath east Africa to Arabia (e.g. Bastow et al., 2008; Benoit et al., 2006; Forte et al., 2010; Furman et al., 2006; Ritsema et al., 1999; Simmons et al., 2007, 2009). The hypothesized northeastward direction of the mantle flow associated with the African superplume is supported by consistent rift-parallel (NE) shear wave splitting measurements beneath the EAR (Figure 3.1B; Bagley and Nyblade, 2013). Bagley and Nyblade (2013) suggests that those NE azimuthal anisotropy are sourced from deep Lattice Preferred Orientation (LPO) of olivine induced by northeastward mantle flow associated with the African superplume.

In this work, we hypothesize that: 1) the observed northward component of surface motion is driven by viscous coupling between the lithosphere and northward mantle flow beneath the EAR and 2) NE oriented azimuthal anisotropy beneath the EAR reflects northeastward mantle flow associated with the African superplume. To test these hypotheses, we use the open-source finite element code Advanced Solver for Problems in the Earth's ConvecTion (ASPECT) (Bangerth et al., 2015, 2020; Kronbichler et al., 2012) to simulate 3D convection and deformation of the lithosphere-asthenosphere system for the EAR and surroundings. Our numerical experiments build upon the model from Rajaonarison et al. (under review, GRL), in which the deformation is driven by lithospheric buoyancy forces. Here, we incorporate sublithospheric mantle flow using thermal anomalies derived from the conversion of shear wave tomography from Emry et al. (2019) to account for plume structures in the upper 660 km. We explore the multiple plumes hypothesis with a model in which mantle flow is constrained only by using shear wave tomography. Then, we test the superplume hypothesis with the same model but with a northward mantle wind beneath 200 km depth to mimic flow that would arise from the African superplume. For each model, we use the mantle

flow to generate synthetic seismic anisotropy that is subsequently compared with observed azimuthal anisotropy beneath the EAR. The synthetic seismic anisotropy is calculated using the routines D-Rex (Kaminski et al., 2004), that follow the kinematic model for plastic deformation and dynamic recrystallization (Kaminski and Ribe, 2001, 2002; Ribe and Yu, 1991). To test the influence of mantle flow on surface deformation, we quantitatively compare surface motion from both models with GNSS observations from Stamps et al. (2018) and block kinematic models from Stamps et al. (2020). We find that the presence of multiple plumes or the superplume does not affect the rigid block rotation of the Victoria and Rovuma Block but produces faster velocities (up to twice in velocity magnitude) for the Somalian Plate. We also found that the northward component of motion along the Main Ethiopian Rift, the Western Branch, and the central Eastern branch can be explained by viscous coupling of the lithosphere to northward mantle flow associated with the African Superplume. The velocity angular misfit between predicted velocities and GNSS/GPS observations in these regions improve from 66°, 114°, and 74°, respectively from model with deformation driven solely by lithospheric buoyancy forces (Rajaonarison et al., under review, GRL), to 50°, 40°, and 30°, respectively. This improvement of the angular misfit suggests that viscous coupling to northward mantle flow is favored withing the deforming zones. Our results also suggest that additional mechanisms, such as anisotorpic viscosity in the asthenpshere is needed to explain the rotation rate of the Somalian Plate. Although lithospheric buoyancy forces dominate the force balance driving E-W extension across the EAR, this work suggests horizontal tractions from northward mantle flow associated with the African Superplume is needed to explain observations of rift-parallel surface motions in deforming zones from GNSS/GPS data and northward oriented seismic anisotropy beneath the EAR.

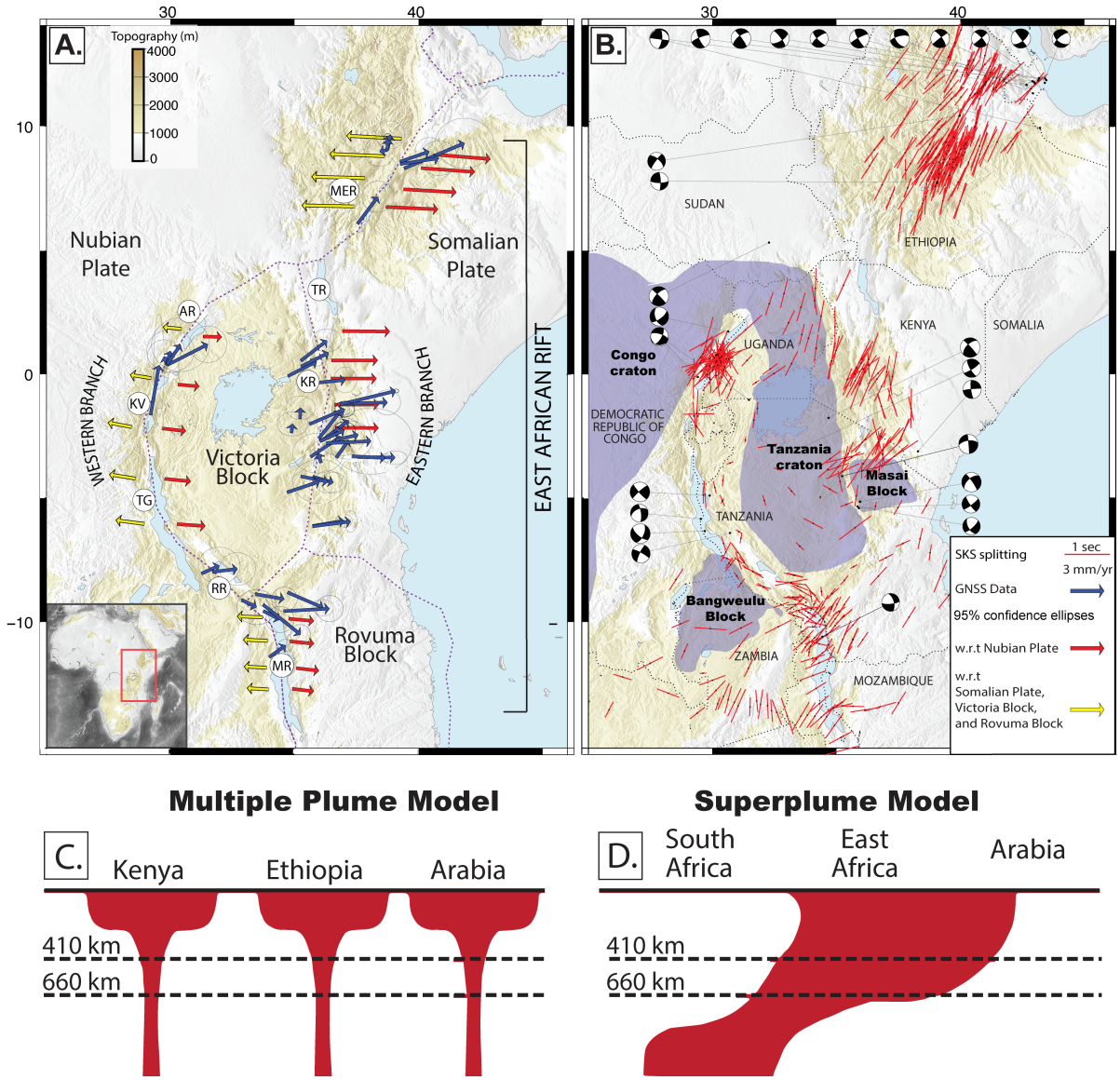

Figure 3.1: a) GPS velocities along deforming zone of the East African Rift (EAR; Stamps et al., 2018; blue vectors with 95% confidence ellipses). Red and yellow vectors are kinematic models from Saria et al. (2014) for the Somalian Plate, the Victoria Block, and the Rovuma Block, respectively. Purple lines are political boundaries. b) Observed SKS splitting (blue bars) and strike-slip focal mechanisms along the EAR. Several rifts are defined: TG = Tanganyika Rift, RR = Rukwa Rift, AR = Albertine Rift, MER = Main Ethiopian Rift, TR = Turkana Rift, KR = Kenya Rift, MR = Malawi Rift, and KV = Kivu Rift. Black dots indicate earthquake locations where strike-slip focal mechanisms are observed (GCMT; Dziewonski et al., 1981; Ekström et al., 2012). (c and d) Plume models for the East African Rift System invoked to explain upper mantle seismic velocity models (adapted from Hansen et al. (2012)). c) The multiple plume model. d) The superplume model that referred to as African superplume.

3.2 Methods

3.2.1 Model Design and Experiments

We use the finite element code ASPECT to simulate lithospheric deformation and mantle flow of the EAR. The surface velocities and mantle flow are solutions of the Stokes system of equations including the Bousinessq equation of momentum and conservation of mass for an incompressible Newtonian fluid (see Appendix A). Although the aim of this study is to assess the contributions of horizontal tractions, from mantle flow beneath the EAR, it is important that the primary driving forces acting in this region, which are lithospheric buoyancy forces and horizontal mantle tractions and are incorporated in the model. Thus, our model is derived from Rajaronarison et al. (under review, GRL) in which the lithospheric buoyancy forces are implemented using ETOPO1 (Amante and Eakins, 2009) for the surface topography and CRUST1.0 for the laterally varying crustal structures and densities (lower, middle, and upper crust; Laske et al., 2013). In this work, mantle flow field driven by density heterogeneities are added in the sublithospheric regions. The sub-lithospheric mantle density in our simulations varies linearly with temperature:

$$\rho = \rho_0(1 - \alpha(T - T_0) \tag{3.1}$$

Where α is the thermal expansion coefficient. The Stokes system of equations is solved using a 3D spherical chunk geometry model domain, covering 5300×3300×660 km in the East, North, and radial directions, respectively.

The initial temperature structure throughout the lithosphere is calculated following the approach of Chapman (1986), which uses an analytical solution for a conductive geothermal profile to obtain temperatures throughout a layered lithosphere (upper crust, middle crust,

lower crust, and mantle lithosphere). A key assumption to this approach is that each layer contains a constant thermal conductivity and radiogenic heat production unique for each layer (Table B.1). While the lithosphere asthenosphere boundary is defined as an isotherm 1673 K, the lithospheric geothermal gradient varies as a function of lithopsheric thickness, the surface heat flow, and the crustal thicknesses (CRUST1.0). We use synthetic lithospheric thickness model that capture the key tectonic regions and obtained from averages of the lithospheric models LITHO1.0 Pasyanos (2013), Fishwick (2010, updated), and Emry (per comm.). For the cratonic regions, including the Tanzania Craton, the Congo Craton, the Bangweulu Block, and the Masai Block, the the lithospheric thicknesses are 150 km thick. For the rifts, the Eastern Branch and the Western Branch have 70 km and 90 km thick lithosphere, respectively. We assume a 100 km thick lithosphere for mobile melts and for the oceanic lithosphere. We also impose 50 km thickness for oceanic ridges.

In sub-lithospheric regions, the temperature is the sum of an approximate adiabatic temperature profile (with 0.0003 K/m increase with depth; Schuberth et al. (2009)) and a temperature anomaly obtained using a conversion of shear wave anomalies from Emry et al. (2019), which is shown in Figure 3.2A,B. The shear wave anomalies are first converted to density perturbations $\delta\rho/\rho$ using a velocity-density factor of 0.15 (e.g. Conrad and Lithgow-Bertelloni, 2006). The density perturbation is further translated into a temperature anomaly ΔT (Figure 3.2C,D) by multiplying it by the negative inverse of thermal expansion (e.g. Austermann et al., 2017; Karato, 1993). The shear tomography from Emry et al. (2019) show low velocity up to 6-12% beneath Kenya Rift and the Main Ethiopian Rift in Figure 3.2A,B, which could result in temperature excess of 500-1000 K following the conversion outlined method above. However, these temperatures are higher than typical plume temperature ranging from 200-300 K (e.g. Schuberth et al., 2009). We apply a temperature excess cut-off of 300 K during the shear wave anomaly to temperature conversion. This assumption is supported by

geochemical evidence suggesting that low velocity beneath the EAR is a combined contribution from mantle temperature, melt (at shallow depth), and composition beneath 200 km (Rooney et al., 2012). Details of calculation of lithospheric geothermal gradient is described in the Appendix B.1.

The numerical experiments incorporate non-linear (non-Newtonian) rheological flow laws, which are needed to match first-order observations of solid Earth deformation and constraints from rock deformation experiments. In brittle regions (i.e. in the upper crust and uppermost mantle), plasticity limits the stress and reduces viscosity, which we assume is in accordance with a Drucker-Prager yield criterion. The viscous flow law for the crust is visco-plastic with dry quartzite and dislocation creep for dry olivine in the mantle lithosphere. We assume that the main composition of the mantle is olivine (dry), where the flow in the sublithospheric mantle lithosphere is governed by composite rheology (Jadamec and Billen, 2010). A plastic strain weakening factor for cohesion and friction is applied to the lithospheric viscosity in the deforming zones (Stamps et al., 2018) in order to promote strain localization. Details of viscosity calculation in the lithosphere and the sub-lithospheric mantle are described in Appendix B.2.

The velocity boundary condition at the model surface is free slip in order to minimize unrealistic vertical motions and restrict near-surface motion to be predominantly horizontal. For the multiple plumes model, the mechanical boundary conditions are free slip on all faces (northern, southern, eastern, and western faces) of our regional model, except at the bottom boundary, where it is fixed. For the superplume model a 2 cm/yr northward velocity boundary conditions is applied at the northern and southern faces below 200 km and zero velocity above this depth.

To test the influence of mantle flow on surface deformation in the EAR, we consider two categories of mantle flow in the sublithospheric regions: (1) multiple plume model in which

the mantle flow is driven by density heterogeneities derived from shear wave tomography as described above, and (2) a superplume model in which the temperature field is the same as the multiple plume model, except that the mantle flow is subject to a northward mantle wind at the boundaries to represent flow from the African superplume. Flow associated with the African superplume is imposed using a 2 cm/yr northward velocity boundary condition at the southern and northern faces of our regional model. The only difference between the multiple plume and superplume models is the initial horizontal velocity imposed at depths between 200-660 km at the south and north face of the model. The 2 cm/yr velocity boundary condition is restricted to below 200 km depth above which (in the lithosphere) the velocity boundary condition is zero. These velocity boundary conditions have the same magnitude and orientation for the southern and northern faces in order to satisfy mass conservation required by the incompressible model.

3.2.2 Estimating Mantle Flow Induced LPO

Using the program D-Rex (Kaminski et al., 2004), we predict asthenospheric crystal aggregates LPO that develops beneath the EAR from both the multiple plume and superplume models. Because D-Rex incorporates deformation mechanisms of olivine-enstatite aggregates in flow such as plastic deformation, grain boundary sliding, and dynamic recrystallization (Kaminski and Ribe, 2001, 2002), the code has been successfully used to estimate synthetic LPO that develop in response to a given global or regional mantle flow field (e.g. Faccenda and Capitanio, 2012, 2013; Hu et al., 2017; Rajaonarison et al., 2020). Since most seismic anisotropy is often interpreted as the fast axis of olivine crystals, the transverse isotropic approximation (TI) output by D-Rex is used here as a proxy for LPO (e.g. Becker et al., 2006; Faccenda and Capitanio, 2012; Hu et al., 2017).

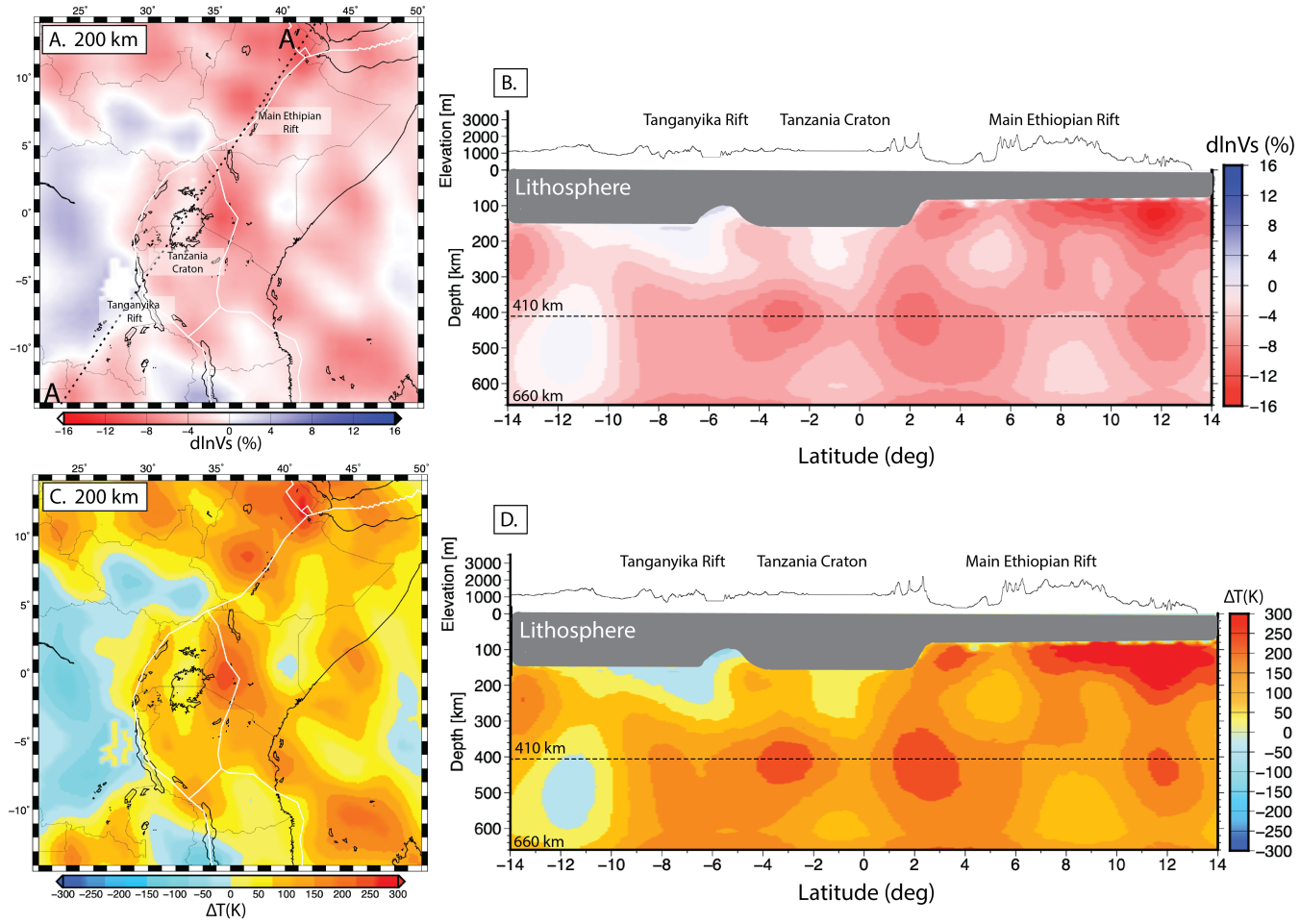

Figure 3.2: (a,b) Shear wave tomography anomaly from Emry et al. (2019): a) at 200 km depth and b) along profile AA'. (c,d) Temperature anomaly obtained by converting the shear wave tomography in (a and b). c) at 200 km depth and d) along profile AA').

The workflow for calculating synthetic LPO that develops along pathlines in steady state flow field is as follows. We consider particles that consist of 2000 virtual grains of olivine (70%) and enstatite (30%) crystals (Kaminski et al., 2004), which represents a harzburgite composition. The particles are located beneath the seismic stations where observations are available, and distributed between 100 km and 400 km depths with a vertical interval of 25 km. For the purpose of calculating their trajectories, first, the particles are advected backward in time, using the fourth order Runge-Kunta advection scheme described in Becker et al. (2003), during which they accumulate strain and stopped until a critical strain of 0.75 is reached (e.g. Rajaonarison et al., 2020) or until the particles reach the 410 km discontinuity. At the location where the backward advection is stopped, the particle is set with randomly oriented crystals to form isotropic mantle and advected forward along its trajectory. During this forward advection, the mineral aggregates accumulate finite strain, LPO develops and evolves along the pathlines in response to shear. Then, D-Rex calculates the global elastic tensor of the grain assemblage using the Voigt averaging scheme for single-crystal elastic tensors and extracts the TI axis orientation that we subsequently compare with observations.

3.3 Results

3.3.1 Mantle Flow Beneath the EAR

The mantle flow from the multiple plume model is mainly characterized by localized upwelling beneath multiple rift segmetns of the EAR (see Figure 3.4). Figure 3.4A,B shows map views of the multiple plumes at depth slices 150 km and 300 km with the background colors showing vertical motions and the vectors indicating horizontal motions at that depth. The positive vertical velocities at 150 km (Figure 3.4A) indicate localized upwelling occurs beneath the

Main Ethiopian Rift, the Eastern Branch, the Western Branch, and the northern Malawi Rift. The upwelling ranges from 6-10 cm/yr, where the upwelling beneath northernmost EAR, the Main Ethiopian Rift, and Kenya Rift are more vigorous that beneath the Western Branch. These patterns of upwelling are consistent with relatively low shear wave anomalies beneath the Main Ethiopian Rift, the Eastern Branch, and northern Malawi Rift, which result in relatively higher temperature, higher buoyancy, and lower viscosity. The associated horizontal velocities show radiating patterns that result mostly in rift perpendicular flow with a mostly E-W orientation. At 300 km depth (Figure 3.4B) the horizontal velocities associated with the localized upwelling are converging inward, indicating that slow seismic velocity anomalies are not connected to a deeper source that passes through the transition zone. A profile view of the mantle flow (Figure 3.4C) shows that the localized upwelling extend down to 410 km discontinuity and is mostly limited to that depth due to the high viscosity between 410-660 km. Figure 3.4C also shows that a downwelling beneath the Tanzania Craton separates the upwellings beneath the Western Branch and Eastern Branch.

Asthenospheric flow from the superplume model beneath the EAR is characterized by northward horizontal flow driven by the imposed northward mantle wind (Figure 3.3A,B). The associated vertical velocities show that the upwellings still occur beneath multiple segments of the rifts. At 150 km (Figure 3.3A), the mantle wind is imposed along the from southern EAR (i.e. the Malawi Rift) and is deflected to the west and to the east by the rheologically strong Tanzania craton. To the west, the mantle flow is channelled northward between the Tanzania craton and the Bangweulu block then accommodate the curvature of the Western Branch to the north. To the East, the mantle flow is slightly deflected eastward by the Tanzania craton. At 300 km depth (Figure 3.3B), the horizontal mantle flow mostly exhibits northward flow directions except beneath the Eastern Branch and Main Ethiopian Rift, where the horizontal flow tends to align in the ∼NE direction. Figure 3.3C shows that

the northward mantle wind generates mostly horizontal northward mantle flow between the base of the lithosphere and the 410-discontinuity beneath the thick lithosphere in the southern EAR. In contrast, beneath the thin lithosphere of northern EAR, localized upwellings still occur at shallow depths.

3.3.2 Comparison of Mantle Flow Induced LPO

In this section, we present the comparison of synthetic LPO, or TI-axis orientation, and observed splitting at locations where each of the observations exist (Figure 3.6 and Figure 3.5). Due to the high variability of the anisotropy orientations, we present the comparisons regionally, partitioned into northern (Regiona A), central (Region B), and southern (Region C) EAR. Also, given the changes of horizontal mantle flow pattern with depth from both multiple plumes and superplume model, we illustrate and present the comparison with observations at relatively shallow asthenosphere (150 km) and at relatively deeper depth (300 km). Table 3.1 shows a summary of the comparison of predicted TI-axis with observed shear wave splitting.

For the multiple plumes mantle flow model (Figure 3.5) the overall observed (N27°E) fast direction ϕ_{obs} pattern (∼S39°E) is poorly reproduced by the calculated synthetic LPO. At 150 km (Figure 3.5A), the synthetic LPO mostly exhibits rift perpendicular trend with an average orientation of S20°E in the northern EAR (Region A), the orientation is S15°E in the central EAR (Region B), and the trend is N20°E at the southern EAR (Region C). Comparisons yield a poor angular misfit with the observations with average angular misfits of 51°, 52°, and 40°, respectively. Similarly, poor misfit are found at 300 km depth because the synthetic LPO also exhibits rift perpendicular trends with average orientations of S20°E, S15°E, and N20°E for the northern, central, and southern EAR, respectively. The

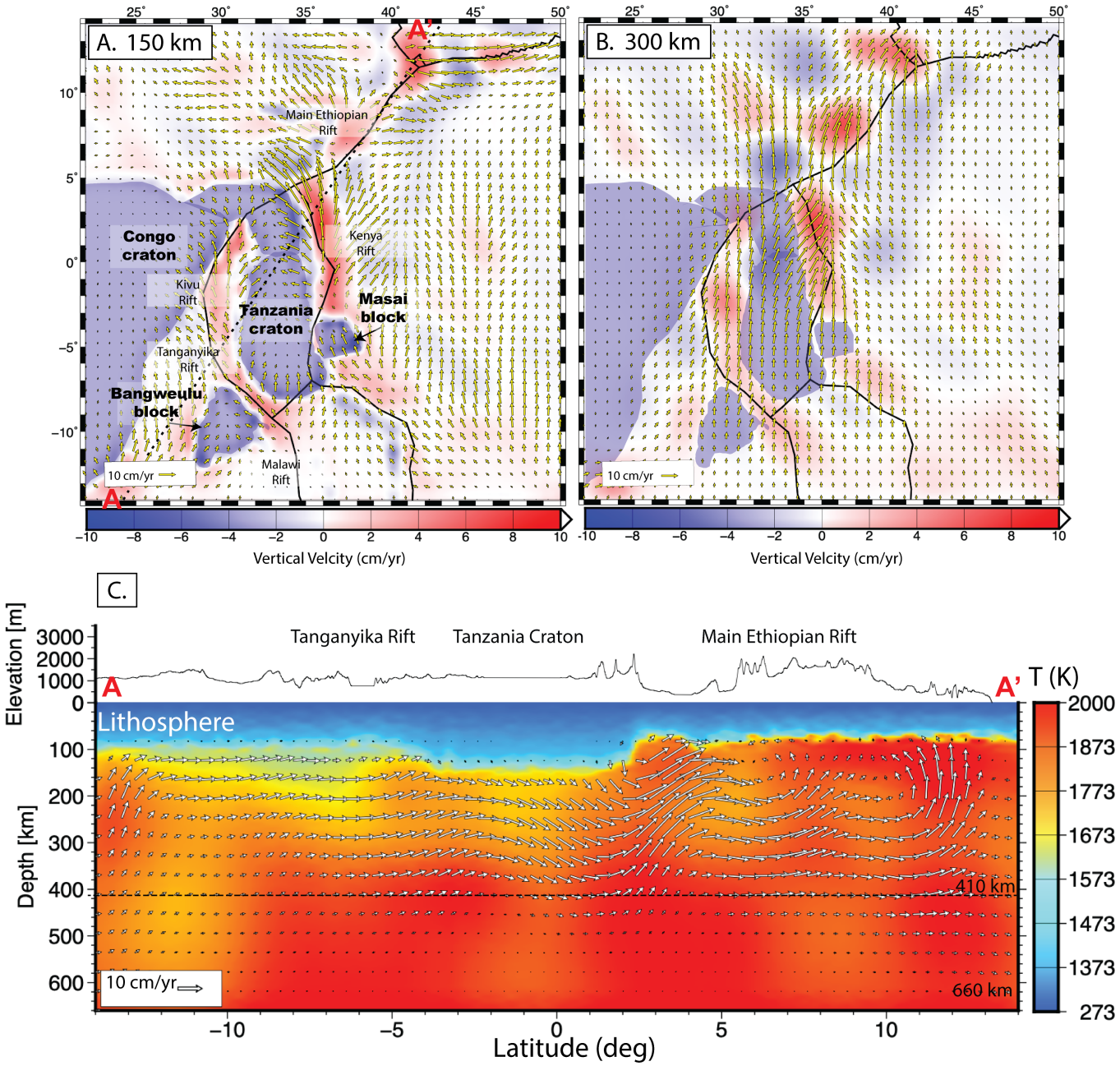

Figure 3.3: Mantle flow field from the superplume model: A) at 150 km depth, B) at 300 km depth. Background color indicates vertical flow. Yellow vectors portray horizontal. C) along profile AA' (Figure 3.3A). The Background color indicates temperature field.

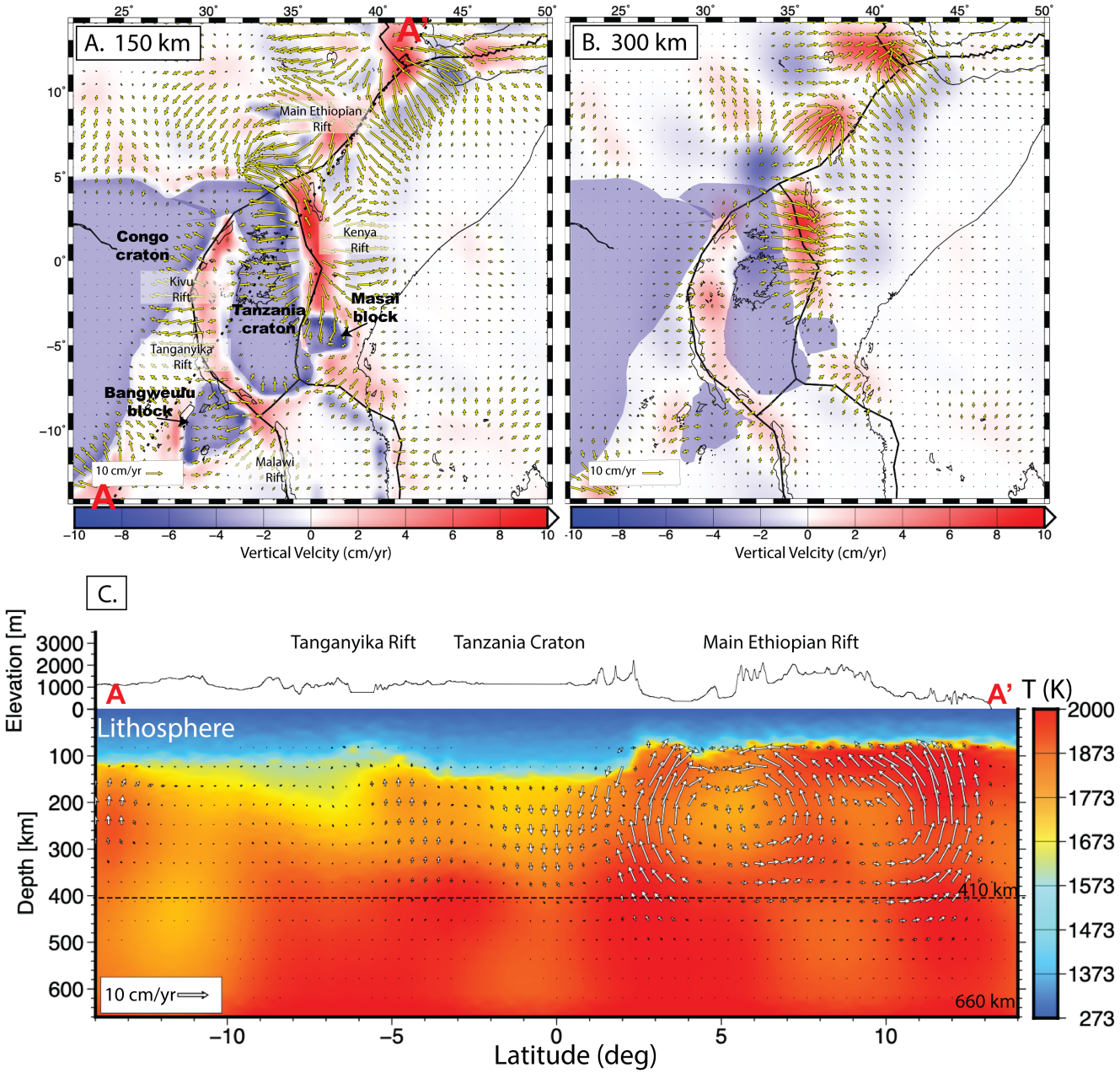

Figure 3.4: Mantle flow field from the multiple plumes model: A) at 150 km depth, B) at 300 km depth. Background color indicates vertical flow. Yellow vectors portray horizontal. C) along profile AA' (Figure 3.4A). The Background color indicates temperature field.

Table 3.1: A comparison of TI-axis, or synthetic LPO, from the two models (multiple plumes and superplume) produced in this work with observed anisotropy. $<\phi_{obs}>$ and $<\delta t_{obs}>$ are the observed regional mean fast direction, respectively. TI-axis represents the predicted synthetic LPO. $<\Delta\alpha>$ is the regional mean angular misfit between the observed fast direction and predicted LPO.

	Observations		Multiple Plumes Model				Superplume Model			
Region	$<\phi_{obs}>^\circ$	$<\delta t_{obs}>$ (s)	TI-axis		$<\Delta\alpha>^\circ$		TI-axis		$<\Delta\alpha>^\circ$	
Depth	-	-	150 km	300 km	150 km	300 km	150 km	300 km	150 km	300 km
Northern	N27°E	1.3	S20°E	S20°E	51°	51°	S30°E	N23°E	60°	20°
Center	N26°E	1.	S15°E	S20°E	52°	51°	S1°E	N13°E	44°	27°
South	N35°E	0.8	N20°E	N1°E	40°	46°	N20°E	N56°E	46°	40°

corresponding mean angular misfits are 51°, 51°, and 46°, respectively. The rift perpendicular trend of the synthetic LPO is due to radiating pattern of the horizontal flow from the multiple plumes model (see Figure 3.4).

For the superplume mantle flow model (Figure 3.6), the overall observed ∼NE fast direction patterns are well reproduced by the calculated synthetic LPO at relatively deeper depths (300 km; Figure 3.6B) than at shallow depths (150 km; Figure 3.6A). At 150 km (Figure 3.6A), the synthetic LPO mostly exhibits rift perpendicular trends (S30°E, S1°E, and N20°E, respectively, for the northern, central, and southern EAR), yielding poor mean angular misfit of 60°, 44°, and 46°, respectively. The rift perpendicular trend of the synthetic LPO at 150 km is consistent with the radiating pattern of horizontal flow pattern (see Figure 3.3A). At 300 km (Figure 3.6B), we find a good fit between the observations and the synthetic LPO with average directions of N23°E, N13°E, and N50°E for the northern, central, and southern EAR, respectively. The best fit is found in the northern EAR (Region A, Figure 3.6B) with an average misfit of 20°. The angular misfits are 27° for central EAR, and 40° in the southern EAR (Region C; Figure 3.6B).

Table 3.2: Summary of the comparison of dynamic velocities from this study (driven by GPE + Multiple Plumes Model and GPE + Superplume Model) and from Rajaonarison et al. (under review, GRL) (driven by GPE only) with kinematic model from Stamps et al. (2020) and GNSS/GPS velocities from Stamps et al. (2018) in deforming zones defined as regions A-F. $\overline{V}$(mm/yr) represents mean velocity, α represents mean angular misfit ([0 - 180°] from good to poor fit), and RMS is the root mean square velocity.

	Kinematic model/GPS	GPE only			GPE+Multiple Plumes Model			GPE+Superplume Model		
Region	$\overline{V}(mm/yr)$	$\overline{V}(mm/yr)$	RMS (mm/yr)	α	$\overline{V}(mm/yr)$	RMS (mm/yr)	α	$\overline{V}$	RMS (mm/yr)	α
Somalian Plate	4.41	6	1.8	10°	13	12.	5°	7.5	5.	5°
Victoria Block	2.13	1.39	0.5	5°	2.5	0.5	6°	2.8	0.6	7°
Rovuma Block	2.14	2.3	0.2	10°	2.	0.5	10°	3.1	1.	6°
Region A	2.59	5.9	2.6	66°	7.1	6	60°	8.1	6.	50°
Region B	2.7	4.3	1.6	12°	2.7	2.1	5°	2.7	0.7	40°
Region C	3.2	5.1	1.3	74°	2.9	2.5	50°	2.7	1.8	3°
Region D	2.8	3.2	1.1	8°	2.	1.5	4°	2.	1.8	30°
Region E	2.55	0.54	1.9	114 °	0.2	1.36	99°	0.3	1.3	4°
Region F	2.6	1.9	0.8	20°	2.4	0.8	20°	2.9	0.7	24°

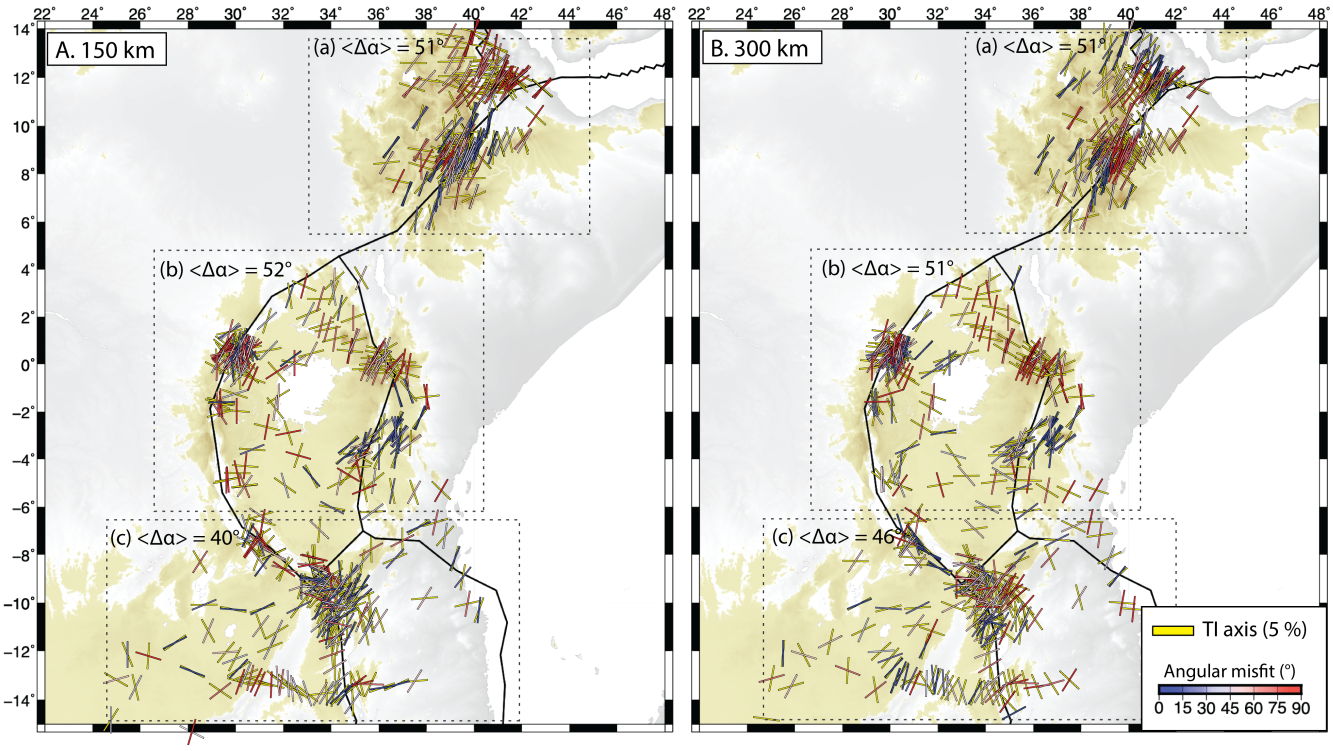

Figure 3.5: Comparison of calculated TI axes with observations from the multiple plume model: A) at 150 km and B) at 300km. The yellow bars indicates TI axis orientation. The SKS splitting measurement bars are colored according to angular misfit [0° - 90°]. The background shows topography.

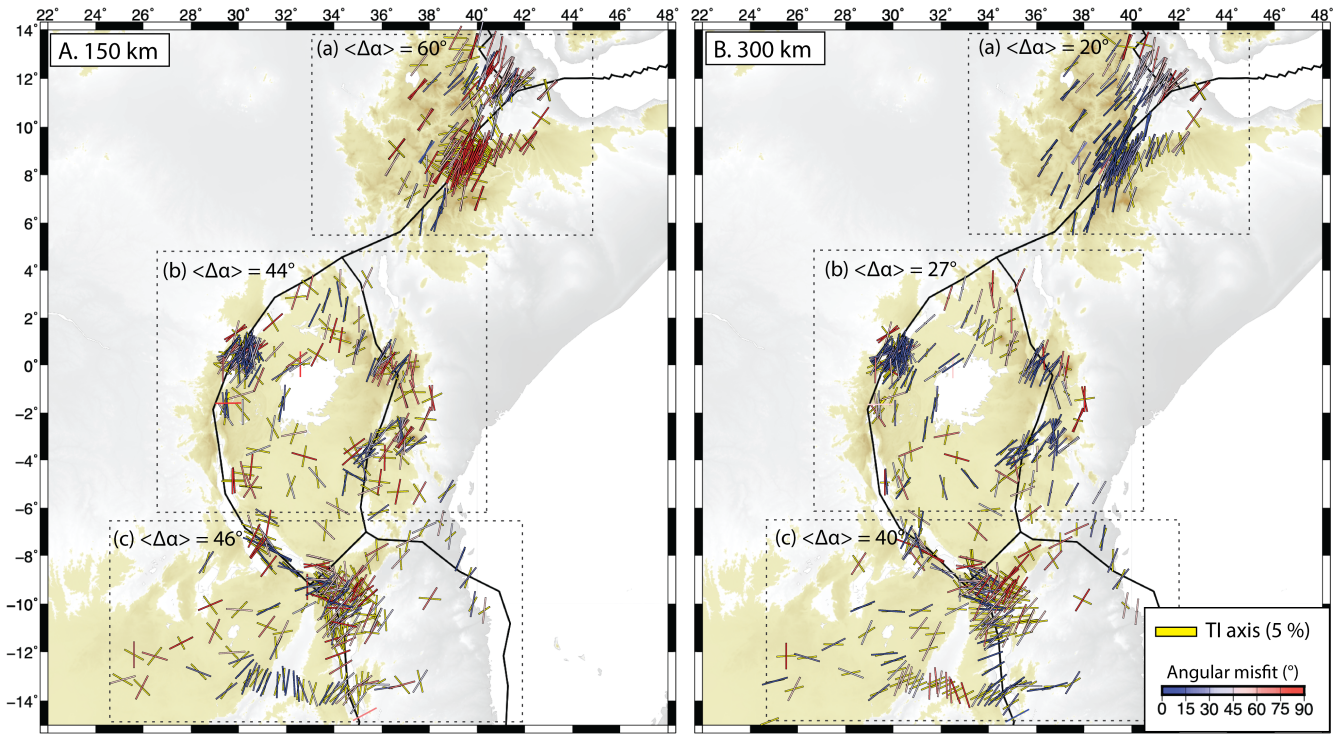

Figure 3.6: Comparison of calculated TI axes with observations from the superplume model: A) at 150 km and B) at 300km. The yellow bars indicates TI axis orientation. The SKS splitting measurement bars are colored according to angular misfit [0° - 90°]. The background shows topography.

3.3.3 Surface Velocity Comparison

To test how the presence of multiple plumes or a superplume beneath the EAR drives surface deformation, we quantitatively compare our dynamic velocity estimates with kinematic predictions of surface motions within zones of rigidity (Saria et al., 2014; Figure 2.4A) and GNSS/GPS velocities in intra-rift zones (Stamps et al., 2018; Figure 3.7 and 3.8). For velocity magnitude comparison, we use the Root Mean Square velocity statistic, whereas regional mean angular misfit ([0-180] from aligned to opposite velocity direction) is used to quantify the fit between predicted and observed velocity directions. The comparison of dynamic velocities with the kinematic model and GPS observations are summarized in Table 3.2.

Dynamic velocities driven by mantle tractions from multiple plumes mantle flow and lithospheric buoyancy forces predict well the rigid plate motions of the Victoria and the Rovuma Block with RMS misfit of 0.5 mm/yr and 0.5 mm/yr, repectively, and an angular misfit of 6° and 10°, respectively (Figure 3.7B). For the Somalian Plate, the dynamic velocities align well with the predicted clockwise rotation with an angular misfit of 5°, but the rotation rate is 13 mm/yr, which is three times larger than the kinematic model (4.41 mm/yr; see Table 3.2), resulting in a large RMS misfit of 12 mm/yr (Figure 3.7A). Within the deforming zones (Figure 3.7B), the dynamic velocities are driven by mantle tractions from the multiple plumes and lithospheric buoyancy forces resulting in a poor fit to the GNSS/GPS observations. In the MER (Region A; Figure 3.7), although the dynamic velocities align well with the GNSS/GPS observations at some stations within the rift, the velocities at the western border of the rift and in the southern region do not align well, yielding a mean angular misfit of 60°. The dynamic velocities are also faster, with a mean velocity of 7.1 mm/yr compared to the GNSS/GPS velocities (2.59 mm/yr; see Table 3.2). In the Eastern Branch (Region B,C,D; Figure 3.7B), we find good fits between the dynamic velocities and the GPS observations in Region B and C, with RMS misfit of 2.1 mm/yr and 1.5 mm/yr, respec-

tively, and angular misfits of 5° mm/yr and 4 mm/yr, respectively. The fit is worse in the central Eastern Branch (Region C; Figure 3.7B) where the RMS misfit is 2.5 mm/yr. In Region C, the fit is consistent with some of the dynamic velocities exhibiting a ∼SE trend whereas the GPS velocities trend ∼NE, yielding poor angular misfit of 50°. For the Western Branch (Region E; Figure 3.7), the mean dynamic velocity magnitude is relatively small (0.2 mm/yr) compared with the 2.55 mm/yr observed by GNSS/GPS, with an RMS misfit of 1.36 mm/yr and the velocities do not align well with a poor angular misfit of 99°. For the southern EAR (Region F; Figure 3.7) or the northern Malawi Rift, we find a good fit of the dynamic velocities and the GNSS/GPS velocities with an angular misfit of 20° and an RMS misfit of 0.8 mm/yr. Overall, the lithospheric buoyancy forces combined with sub-lithospheric multiple plumes drive similar surface deformation to the lithospheric buoyancy forces alone estimated by Rajaonarison et al. (under review, GRL), indicating that lithospheric deformation is decoupled from the mantle flow, except for the Somalian Plate, which appears to be coupled with the underlying eastward mantle flow.

For the model in which deformation is driven by mantle tractions from the superplume and lithospheric buoyancy forces, the block kinematics are also predicted well with angular misfits of 5°, 7°, and 6°, respectively for the Somalian Plate, Victoria Block, and Rovuma Block. Their rotation rates are slightly faster (7.5 mm/yr, 2.8 mm/yr, and 3.1 mm/yr, respectively) than the kinematic model (4.41 mm/yr, 2.13 mm/yr, and 2.14 mm/yr, respectively). The Somalian Plate rotation exhibits the largest RMS misfit (5 mm/yr), indicating some degree of coupling between the plate and the underlying mantle flow. In the deforming zones, we find some improvement of the fit with the lithospheric buoyancy forces and superplume combined model. In the MER (Region A; Figure 3.8), although the RMS misfit is relatively large (6 mm/yr), the mean angular misfit decreases from 66° (from the model with only GPE only, see Table 3.2) to 30°, with predicted velocities and observations having opposite directions at

a station located in the southern part of Region A. We also find in the mean angular misfit at the central Eastern Branch (Region C), where the dynamic velocities at some stations have shifted from ∼SE trend to ∼E-W and ∼NE decreasing the mean angular misfit from 73° to 30°. In the Western Branch (Region E; Figure 3.8), the mean angular misfit also significantly improves form 114° to 43° respectively. However, the dynamic velocities remain small 0.7 mm/yr compared to the GNSS/GPS velocities (2.55 mm/yr). In the southern EAR (Region F; Figure 3.8), the dynamic velocities exhibit ∼E-W and ∼NE trends whereas the GPS velocities are oriented ∼E-W and ∼SE, which slightly worsens the mean angular misfit from 20° to 24°, but may be within the uncertainties of the model. Overall, the comparison of dynamic velocities from the combined lithospheric buoyancy forces and the superplume model indicates there is some degree of lithosphere coupling to northward flow, notably within the deforming zones and beneath the Somalian Plate.

3.4 Discussion

3.4.1 Source of Observed Seismic Anisotropy Beneath EAR

Overall observed seismic anisotropy in the EAR exhibits N-S or NNE trends with delay times ranging from 1-1.5 s. Most anisotropy with such relatively large delay time are often attributed to mantle flow induced LPO (Helffrich, 1995). However, in divergent settings, mantle flow induced LPO are expected to be perpendicular to the rifts. For example along mid oceanic ridges mantle flow induced LPO are perpendicular to the plate boundaries (Becker et al., 2003, 2006, 2014). Thus, interpretations of the observed rift parallel anisotropy along the EAR remains controversial. Several mechanisms such as fossilized anisotropy due to past orogenic events (Homuth et al., 2016; Walker et al., 2004), parallel dykes or magma-

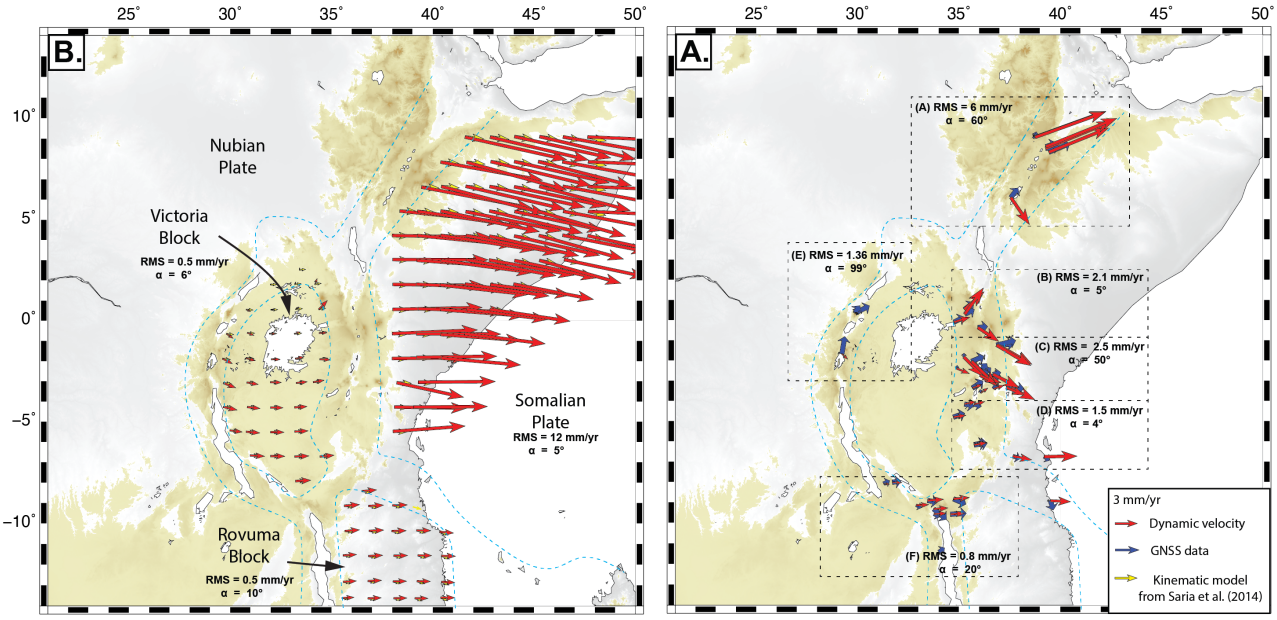

Figure 3.7: Comparison of dynamic velocities (red vectors) driven by mantle tractions from the multiple plumes model and lithospheric buoyancy forces with: A) kinematic predictions from the Stamps et al. (2020) model (yellow vectors) within the Somalian Plate, the Victoria and the Rovuma Blocks. B) GNSS/GPS data from (Stamps et al., 2018, blue vectors) within the deforming zones (dashed blue line) and Comparisons statistics (RMS and mean angular misfit) are show inside a dashed box for each region.

filled (Albaric et al., 2014; Gao et al., 1997) lences has been invoked as an explanation for the rift parallel anisotropy. Bagley and Nyblade (2013) suggest that the overall consistent N-S or NNE trend of the anisotropy can be attributed one single mechanism that is the northward flow of the African superplume.

The results presented here corroborate with the African superplume hypothesis suggested by Bagley and Nyblade (2013) because we find good alignment with calculated LPO and observations at deeper depths (300 km) than shallower depths (150 km) for the superplume mantle flow model. Moreover, the multiple plume model does not produce a good fit with the observations indicating that mantle upwelling beneath the Main Ethiopian Rift, the Kenya Rift, the Western Branch are influenced by northward flow from the African superplume.

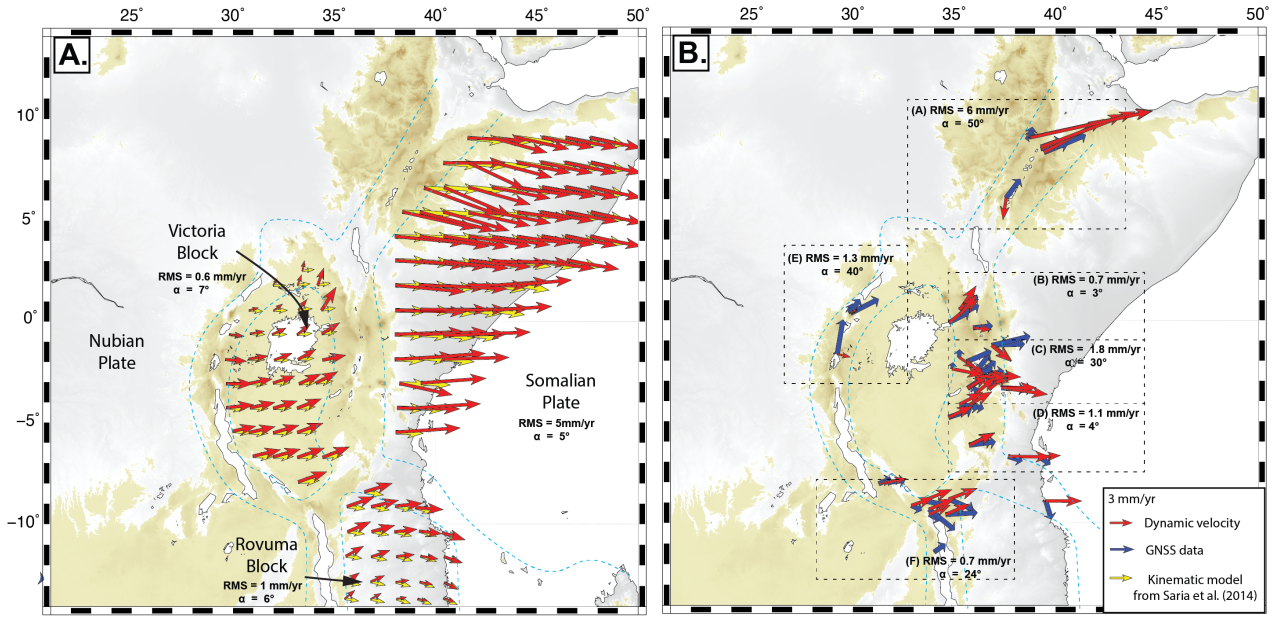

Figure 3.8: Comparison of dynamic velocities (red vectors) driven by mantle tractions from the superplume model and lithospheric buoyancy forces with: A) kinematic predictions from the Stamps et al. (2020) model (yellow vectors) within the Somalian Plate, the Victoria and the Rovuma Blocks. B) GNSS/GPS data from (Stamps et al., 2018, blue vectors) within the deforming zones (dashed blue line) and Comparisons statistics (RMS and mean angular misfit) are show inside a dashed box for each region.

Our results also highlight the importance of the Tanzania craton, Congo craton, and the Bangweulu Block in channelling the northward mantle wind resulting in rift parallel mantle flow mainly in the Western Branch. This rift parallel mantle flow results in rift parallel anisotropy explaining most of the seismic anisotropy including those in the northernmost Western Branch. It is also worth nothing that sub-lithosphere mantle viscosity play important role in favoring rift parallel mantle flow. For example, the mantle flow and the LPO exhibit NNE trend at the Main Ethiopian Rift as a result of low viscosity along the strike of the rift.

3.4.2 Plume-Lithosphere Interactions Beneath EAR

Our comparison of surface velocities with predicted rigid block motion and GPS velocities highlights the importance of the interactions between the lithosphere and mantle flow associated with the African superplume beneath the EAR. This significance of plume-lithosphere interactions has been noticed by Forte et al. (2010) and (Ghosh and Holt, 2012), who suggest that mantle tractions from divergent flow associated with the African superplume alone can cause the opening of East Africa. However, previous geodynamic modeling results suggest that the E-W extension of the EAR is dominated by lithospheric buoyancy forces and adding sub-lithospheric mantle flow over-predicted the observed deformation (Stamps et al., 2014, 2015). Our numerical experiments of lithospheric deformation combined with asthenospheric flow suggest that the multiple plumes model beneath the EAR does not significantly affect the surface deformation of the EAR, except for the Somalian Plate where the rotation rate is over-predicted. Moreover, the multiple plumes mantle flow cannot explain the northward component of motion with the deforming zones. The inconsistency between the multiple plume model and surface velocities in the deforming zones is likely because (Figure 3.4) beneath the rifts is dominated by upwelling and diverging E-W flow beneath the adjacent rigid blocks. In contrast, for the superplume (Figure 3.3) results in the mantle flow beneath the rifts that is mostly oriented northward and rift parallel. This northward horizontal flow generates horizontal tractions at the base of the lithosphere and produces northward surface motions.

Our results also suggest that the counter-clockwise rotation of the Victoria Block is independent of the underlying mantle flow from the multiple plumes model, but a minor contribution might occur from the northward mantle flow associated with the African Superplume. Due to the presence of Tanzania Craton within the Victoria Block, the lithosphere-asthenosphere coupling is expected to be significant because previous studies have shown that viscous cou-

pling between asthenosphere and lithosphere is favorable beneath cratonic roots (Conrad and Lithgow-Bertelloni, 2006; Stoddard and Abbott, 1996; Zhong, 2001). This strong coupling is not case for the Victoria Block because of the continuation of the Congo Craton into the Tanzania Craton through northern Western Branch provides resisting forces (drag) to mantle tractions. The resisting forces can be caused by the stability of the Congo Craton within the stable Nubian Plate. The role of craton in favoring viscous coupling of mantle flow and lithosphere can, however, be observed at the central Eastern Branch, located to the north of the Masai Block. Our results indicate that due to the presence of the Masai Block, the surface deformation in central Eastern Branch is influenced by the underlying northward mantle flow associated with the African Superplume.

3.4.3 Anisotropic Viscosity

Our results indicate the rotation rate of the Somalian Plate is over-predicted by our lithospheric deformation models driven by lithospheric buoyancy forces and mantle flow (multiple plumes and superplume model). Previous geodynamic modeling studies have also reported this over-prediction when coupling lithospheric deformation with basal shear from global mantle flow models (e.g. Stamps et al., 2014, 2015). These previous studies suggest that lithospheric buoyancy forces alone are capable of driving present-day plate motion of the EAR and that viscous coupling between mantle flow and lithosphere should be inefficient. Stamps et al. (2015) attribute the inefficiency of coupling with lower viscosity of the asthenosphere or slower mantle flow than is often estimated. An alternative mechanism of decoupling between mantle flow and lithosphere beneath the EAR is anisotropic viscosity in the asthenosphere. Recent studies on viscous anisotropy in the asthenosphere reveal that the development of olivine aggregates'LPO can weaken the viscosity in the direction parallel to the fabrics and strengthen the viscosity in the perpendicular direction (Hansen et al., 2016;

Király et al., 2020). The anisotropic viscosity has important implication for plate motion because it can increase plate velocity in the direction of the LPOs and slows down in the perpendicular direction over a period up of to ∼10 Myr (Király et al., 2020).

Here, we found that the observed rift parallel NE seismic anisotropy beneath the EAR can be associated with the northward mantle flow from the African Superplume. The presence of such long-term northward flow and the induced LPO could lead to anisotropic viscosity beneath the EAR. This would result in weak viscosity parallel to the rifts and thus faster northward flow than extimated in this study. Conversely, the viscosity in the E-W direction would be stronger causing more resistance to plate motion and would result in slower Somalian plate motion. Since in this study, we have posteriorly calculated the synthetic LPO after the mantle flow simulation, the anisotropic viscosity is not captured in our models. The implementation of anisotropic viscosity would require using a viscosity tensor (e.g. Hansen et al., 2016; Király et al., 2020; Perry-Houts and Karlstrom, 2019) rather than the scalar composite viscosity used here. The concept of anisotropic viscosity beneath the EAR provides new insight into the lithosphere and mantle dynamics beneath East African and a future direction for studies of continental rifting.

3.5 Conclusions

We use 3D thermomechanical modeling of the lithosphere-asthenosphere system to investigate: 1) the role plume-lithosphere interactions beneath the EAR in driving observed surface deformation and 2) the sources of observed seismic anisotropy beneath the EAR oriented approximately ∼N-S. We tests two types of mantle flow models including a multiple plume model constrain by shear wave tomography from Emry et al. (2019) and an African superplume model simulating a northward mantle wind on the multiple plume model. Our results

indicate that interactions of the northward African superplume with the rigid Tanzania craton, Congo craton, and Bangweulu and Masai Blocks may be controlling mantle flow orientations beneath the EAR and may be the source of most of the observed seismic anisotropy beneath northern and southern EAR. We also found that the multiple plume mantle flow model should be ruled out as a dominant source mechanism of sublithospheric mantle flow beneath the EAR. Comparison of dynamic velocities and block kinematics suggests that the Victoria and Rovuma Blocks rotate independently from mantle flow from multiple plumes or superplume. In contrast, we found that for the multiple plumes and superplume mantle flow models, the Somalian plate is over-predicted up to twice or three time its expected rotation rate. While the multiple plumes mantle flow model does not significantly affect the surface deformation driven by the lithospheric buoyancy forces, the northward mantle flow field from the superplume model drives northward component of motions in the deforming zones that improves the fit at the Main Ethiopian Rift, Central Eastern Branch, and northern Western Branch. Our results suggest that sublithospheric viscosity beneath the EAR might be anisotropic due to developed olivine aggregates's LPO induced by the African superplume. The anisotropic viscosity might control the rotation rate of the Somalian Plate.

Bibliography

J. Albaric, J. Deverchere, J. Perrot, A. Jakovlev, and A. Deschamps. Deep crustal earthquakes in north tanzania, east africa: Interplay between tectonic and magmatic processes in an incipient rift. *Geochemistry, Geophysics, Geosystems*, 15(2):374–394, 2014.

L. R. Alejano and A. Bobet. Drucker–prager criterion. In *The ISRM Suggested Methods for Rock Characterization, Testing and Monitoring: 2007-2014*, pages 247–252. Springer, 2012.

C. Amante and B. W. Eakins. Etopo1 arc-minute global relief model: procedures, data sources and analysis. 2009.

D. L. Anderson. The thermal state of the upper mantle; no role for mantle plumes. *Geophysical Research Letters*, 27(22):3623–3626, 2000.

D. F. Argus, R. G. Gordon, and C. DeMets. Geologically current motion of 56 plates relative to the no-net-rotation reference frame. *Geochemistry, Geophysics, Geosystems*, 12 (11), 2011.

J. Austermann, J. X. Mitrovica, P. Huybers, and A. Rovere. Detection of a dynamic topography signal in last interglacial sea-level records. *Science Advances*, 3(7):e1700457, 2017. doi: 10.1126/sciadv.1700457. URL http://advances.sciencemag.org/lookup/doi/10.1126/sciadv.1700457.

B. Bagley and A. A. Nyblade. Seismic anisotropy in eastern africa, mantle flow, and the african superplume. *Geophysical Research Letters*, 40(8):1500–1505, 2013.

M. D. Ballmer, C. P. Conrad, E. I. Smith, and R. Johnsen. Intraplate volcanism at the edges of the Colorado Plateau sustained by a combination of triggered edge-driven convection and shear-driven upwelling. *Geochemistry, Geophysics, Geosystems*, 16(2):366–379, 2015.

W. Bangerth, T. Heister, et al. Aspect: Advanced solver for problems in earth's convection. *Computational Infrastructure for Geodynamics*, 2015.

W. Bangerth, J. Dannberg, R. Gassmoeller, T. Heister, et al. ASPECT v2.1.0 [software], June 2018a. URL https://doi.org/10.5281/zenodo.1297145.

W. Bangerth, J. Dannberg, R. Gassmöller, T. Heister, et al. **ASPECT**: Advanced Solver for Problems in Earth's ConvecTion, User Manual. may 2018b. doi: 10.6084/m9.figshare.4865333. URL https://doi.org/10.6084/m9.figshare.4865333. doi:10.6084/m9.figshare.4865333.

W. Bangerth, J. Dannberg, R. Gassmoeller, and T. Heister. Aspect v2.2.0, June 2020. URL https://doi.org/10.5281/zenodo.3924604.

C. Bassin. The current limits of resolution for surface wave tomography in north america. *EOS Trans. AGU. 81: Fall Meet. Suppl., Abstract*, 2000.

I. Bastow, A. A. Nyblade, G. Stuart, T. Rooney, and M. Benoit. Upper mantle seismic structure beneath the ethiopian hot spot: Rifting at the edge of the african low-velocity anomaly. *Geochemistry, Geophysics, Geosystems*, 9(12), 2008.

T. W. Becker, J. B. Kellogg, G. Ekström, and R. J. O'Connell. Comparison of azimuthal seismic anisotropy from surface waves and finite strain from global mantle-circulation models. *Geophysical Journal International*, 155(2):696–714, 2003.

T. W. Becker, S. Chevrot, V. Schulte-Pelkum, and D. K. Blackman. Statistical properties of

seismic anisotropy predicted by upper mantle geodynamic models. *Journal of Geophysical Research: Solid Earth*, 111(B8), 2006.

T. W. Becker, C. P. Conrad, A. J. Schaeffer, and S. Lebedev. Origin of azimuthal seismic anisotropy in oceanic plates and mantle. *Earth and Planetary Science Letters*, 401:236–250, 2014.

C. Beghein, K. Yuan, N. Schmerr, and Z. Xing. Changes in seismic anisotropy shed light on the nature of the Gutenberg discontinuity. *Science*, 343(6176):1237–1240, 2014.

M. D. Behn, C. P. Conrad, and P. G. Silver. Detection of upper mantle flow associated with the African Superplume. *Earth and Planetary Science Letters*, 224(3-4):259–274, 2004.

M. H. Benoit, A. A. Nyblade, and J. C. VanDecar. Upper mantle p-wave speed variations beneath ethiopia and the origin of the afar hotspot. *Geology*, 34(5):329–332, 2006.

D. Bertil and J. M. Regnoult. Seismotectonics of Madagascar. *Tectonophysics*, 294(1):57–74, 1998.

P. Bird, Z. Liu, and W. K. Rucker. Stresses that drive the plates from below: Definitions, computational path, model optimization, and error analysis. *Journal of Geophysical Research: Solid Earth*, 113(B11), 2008.

E. Bredow. *Geodynamic models of plume-ridge interaction*. PhD thesis, Universität Potsdam, 2017. URL http://nbn-resolving.de/urn:nbn:de:kobv:517-opus4-411732.

E. Calais, C. Ebinger, C. Hartnady, and J. Nocquet. Kinematics of the east african rift from gps and earthquake slip vector data. *Geological Society, London, Special Publications*, 259 (1):9–22, 2006.

V. E. Camp and M. J. Roobol. Upwelling asthenosphere beneath western arabia and its regional implications. *Journal of Geophysical Research: Solid Earth*, 97(B11):15255–15271, 1992.

S.-J. Chang and S. Van der Lee. Mantle plumes and associated flow beneath arabia and east africa. *Earth and Planetary Science Letters*, 302(3-4):448–454, 2011.

D. Chapman. Thermal gradients in the continental crust. *Geological Society, London, Special Publications*, 24(1):63–70, 1986.

D. D. Coblentz and M. Sandiford. Tectonic stresses in the african plate: Constraints on the ambient lithospheric stress state. *Geology*, 22(9):831–834, 1994.

A. Collins. The tectonic evolution of Madagascar: Its place in the East African Orogen. *Gondwana Research*, 4(3):549–552, 2000.

A. S. Collins and B. F. Windley. The tectonic evolution of central and northern Madagascar and its place in the final assembly of Gondwana. *The Journal of geology*, 110(3):325–339, 2002.

A. S. Collins, I. C. Fitzsimons, B. Hulscher, and T. Razakamanana. Structure of the eastern margin of the East African Orogen in central Madagascar. *Precambrian Research*, 123 (2-4):111–133, 2003.

C. P. Conrad and M. D. Behn. Constraints on lithosphere net rotation and asthenospheric viscosity from global mantle flow models and seismic anisotropy. *Geochemistry, Geophysics, Geosystems*, 11(5), 2010.

C. P. Conrad and C. Lithgow-Bertelloni. Influence of continental roots and asthenosphere on plate-mantle coupling. *Geophysical Research Letters*, 33(5), 2006.

G. Corti, R. Cioni, Z. Franceschini, F. Sani, S. Scaillet, P. Molin, I. Isola, F. Mazzarini, S. Brune, D. Keir, A. Erbello, A. Muluneh, F. Illsley-Kemp, and A. Glerum. Aborted propagation of the ethiopian rift caused by linkage with the kenyan rift. *Nature Communications*, 10:1309, 2019. doi: 10.1038/s41467-019-09335-2. URL https://doi.org/10.1038/s41467-019-09335-2.

E. S. C. H. J.-M. N. C. J. E. R. M. F. D. S. Stamps, E. Calais. A kinematic model for the east african rift. *Geophys. Res. Lett.*, 35:L05304, 2008.

J. Dannberg and R. Gassmöller. Chemical trends in ocean islands explained by plume−slab interaction. *Proceedings of the National Academy of Sciences*, 115(17):4351–4356, 2018.

M. J. de Wit. Madagascar: heads it's a continent, tails it's an island. *Annual Review of Earth and Planetary Sciences*, 31(1):213–248, 2003.

M. J. de Wit, S. A. Bowring, L. D. Ashwal, L. G. Randrianasolo, V. P. Morel, and R. A. Rambeloson. Age and tectonic evolution of Neoproterozoic ductile shear zones in southwestern Madagascar, with implications for Gondwana studies. *Tectonics*, 20(1):1–45, 2001.

E. Debayle, F. Dubuffet, and S. Durand. An automatically updated S-wave model of the upper mantle and the depth extent of azimuthal anisotropy. *Geophysical Research Letters*, 43(2):674–682, 2016.

A. Dziewonski, T.-A. Chou, and J. H. Woodhouse. Determination of earthquake source parameters from waveform data for studies of global and regional seismicity. *Journal of Geophysical Research: Solid Earth*, 86(B4):2825–2852, 1981.

A. M. Dziewonski and D. L. Anderson. Preliminary Reference Earth Model. *Physics of the Earth and Planetary Interiors*, 25(4):297–356, 1981.

C. J. Ebinger and N. Sleep. Cenozoic magmatism throughout east africa resulting from impact of a single plume. *Nature*, 395(6704):788–791, 1998.

M. Edwards. Global gridded elevation and bathymetry (etopo5). *Digital raster data on a*, 5, 1989.

G. Ekström, M. Nettles, and A. Dziewoński. The global cmt project 2004–2010: Centroid-moment tensors for 13,017 earthquakes. *Physics of the Earth and Planetary Interiors*, 200:1–9, 2012.

E. L. Emry, Y. Shen, A. A. Nyblade, A. Flinders, and X. Bao. Upper mantle earth structure in africa from full-wave ambient noise tomography. *Geochemistry, Geophysics, Geosystems*, 20(1):120–147, 2019.

M. Faccenda and F. Capitanio. Development of mantle seismic anisotropy during subduction-induced 3-D flow. *Geophysical Research Letters*, 39(11), 2012.

M. Faccenda and F. A. Capitanio. Seismic anisotropy around subduction zones: Insights from three-dimensional modeling of upper mantle deformation and sks splitting calculations. *Geochemistry, Geophysics, Geosystems*, 14(1):243–262, 2013.

R. Fernandes, J. Miranda, D. Delvaux, D. Stamps, and E. Saria. Re-evaluation of the kinematics of victoria block using continuous gnss data. *Geophysical Journal International*, 193(1):1–10, 2013.

S. Fishwick. Surface wave tomography: imaging of the lithosphere–asthenosphere boundary beneath central and southern Africa? *Lithos*, 120(1):63–73, 2010, updated.

L. Fleitout. The sources of lithospheric tectonic stresses. *Philosophical Transactions of the Royal Society of London. Series A: Physical and Engineering Sciences*, 337(1645):73–81, 1991.

L. Fleitout and C. Froidevaux. Tectonics and topography for a lithosphere containing density heterogeneities. *Tectonics*, 1(1):21–56, 1982.

L. M. Flesch, W. E. Holt, A. J. Haines, and B. Shen-Tu. Dynamics of the pacific-north american plate boundary in the western united states. *Science*, 287(5454):834–836, 2000.

L. M. Flesch, A. J. Haines, and W. E. Holt. Dynamics of the india-eurasia collision zone. *Journal of Geophysical Research: Solid Earth*, 106(B8):16435–16460, 2001.

L. M. Flesch, W. E. Holt, A. J. Haines, L. Wen, and B. Shen-Tu. The dynamics of western north america: stress magnitudes and the relative role of gravitational potential energy, plate interaction at the boundary and basal tractions. *Geophysical Journal International*, 169(3):866–896, 2007.

A. M. Forte and J. X. Mitrovica. New inferences of mantle viscosity from joint inversion of long-wavelength mantle convection and post-glacial rebound data. *Geophysical Research Letters*, 23(10):1147–1150, 1996.

A. M. Forte, S. Quéré, R. Moucha, N. A. Simmons, S. P. Grand, J. X. Mitrovica, and D. B. Rowley. Joint seismic–geodynamic-mineral physical modelling of african geodynamics: A reconciliation of deep-mantle convection with surface geophysical constraints. *Earth and Planetary Science Letters*, 295(3-4):329–341, 2010.

M. Fraters, W. Bangerth, C. Thieulot, A. Glerum, and W. Spakman. Efficient and practical Newton solvers for non-linear Stokes systems in geodynamic problems. *Geophysical Journal International*, 218(2):873–894, 2019.

T. Furman, J. Bryce, T. Rooney, B. Hanan, G. Yirgu, and D. Ayalew. Heads and tails: 30 million years of the afar plume. *Geological Society, London, Special Publications*, 259(1): 95–119, 2006.

S. Gao, P. M. Davis, H. Liu, P. D. Slack, A. W. Rigor, Y. A. Zorin, V. V. Mordvinova, V. M. Kozhevnikov, and N. A. Logatchev. Sks splitting beneath continental rift zones. *Journal of Geophysical Research: Solid Earth*, 102(B10):22781–22797, 1997.

R. George, N. Rogers, and S. Kelley. Earliest magmatism in ethiopia: evidence for two mantle plumes in one flood basalt province. *Geology*, 26(10):923–926, 1998.

A. Ghosh and W. E. Holt. Plate motions and stresses from global dynamic models. *Science*, 335(6070):838–843, 2012.

A. Ghosh, W. E. Holt, and L. M. Flesch. Contribution of gravitational potential energy differences to the global stress field. *Geophysical Journal International*, 179(2):787–812, 2009.

A. Ghosh, W. Holt, and L. Wen. Predicting the lithospheric stress field and plate motions by joint modeling of lithosphere and mantle dynamics. *Journal of Geophysical Research: Solid Earth*, 118(1):346–368, 2013.

G. C. Gleason and J. Tullis. A flow law for dislocation creep of quartz aggregates determined with the molten salt cell. *Tectonophysics*, 247(1-4):1–23, 1995.

A. Glerum, C. Thieulot, M. Fraters, C. Blom, and W. Spakman. Nonlinear viscoplasticity in ASPECT: benchmarking and applications to subduction. *Solid Earth*, 9(2):267, 2018a.

A. Glerum, C. Thieulot, M. Fraters, C. Blom, and W. Spakman. Nonlinear viscoplasticity in aspect: benchmarking and applications to subduction. *Solid Earth*, 9:267–294, 2018b.

A. Glerum, S. Brune, D. S. Stamps, and M. R. Strecker. Victoria continental microplate dynamics controlled by the lithospheric strength distribution of the east african rift. *Nature Communications*, 11(1):1–15, 2020.

L. N. Hansen, J. M. Warren, M. E. Zimmerman, and D. L. Kohlstedt. Viscous anisotropy of textured olivine aggregates, part 1: Measurement of the magnitude and evolution of anisotropy. *Earth and Planetary Science Letters*, 445:92–103, 2016.

S. E. Hansen, A. A. Nyblade, and M. H. Benoit. Mantle structure beneath africa and arabia from adaptively parameterized p-wave tomography: Implications for the origin of cenozoic afro-arabian tectonism. *Earth and Planetary Science Letters*, 319:23–34, 2012.

T. Heister, J. Dannberg, R. Gassmöller, and W. Bangerth. High accuracy mantle convection simulation through modern numerical methods. II Realistic models and problems. *Geophysical Journal International*, 210(2):833–851, 2017. doi: 10.1093/gji/ggx195. URL https://doi.org/10.1093/gji/ggx195.

G. Helffrich. Lithospheric deformation inferred from teleseismic shear wave splitting observations in the united kingdom. *Journal of Geophysical Research: Solid Earth*, 100(B9): 18195–18204, 1995.

P. J. Heron, R. N. Pysklywec, R. Stephenson, and J. van Hunen. Deformation driven by deep and distant structures: Influence of a mantle lithosphere suture in the Ouachita Orogeny, southeastern United States. *Geology*, 2018.

M. M. Hirschmann. Partial melt in the oceanic low velocity zone. *Physics of the Earth and Planetary Interiors*, 179(1-2):60–71, 2010.

G. Hirth and D. Kohlstedt. Rheology of the upper mantle and the mantle wedge: A view from the experimentalists. *Inside the Subduction Factory*, pages 83–105, 2003.

B. Homuth, U. Löbl, A. Batte, K. Link, C. Kasereka, and G. Rümpker. Seismic anisotropy of the lithosphere/asthenosphere system beneath the rwenzori region of the albertine rift. *International Journal of Earth Sciences*, 105(6):1681–1692, 2016.

J. Hu, M. Faccenda, and L. Liu. Subduction-controlled mantle flow and seismic anisotropy in South America. *Earth and Planetary Science Letters*, 470:13–24, 2017.

M. A. Jadamec and M. I. Billen. Reconciling surface plate motions with rapid three-dimensional mantle flow around a slab edge. *Nature*, 465(7296):338, 2010.

K. H. Ji, D. S. Stamps, H. Geirsson, N. Mashagiro, M. Syauswa, B. Kafudu, J. Subira, and N. d'Oreye. Deep magma accumulation at nyamulagira volcano in 2011 detected by gnss observations. *Journal of African Earth Sciences*, 134:824–830, 2017.

C. H. Jones, J. R. Unruh, and L. J. Sonder. The role of gravitational potential energy in active deformation in the southwestern united states. *Nature*, 381(6577):37–41, 1996.

L. Kaislaniemi and J. van Hunen. Dynamics of lithospheric thinning and mantle melting by edge-driven convection: Application to Moroccan Atlas Mountains. *Geochemistry, Geophysics, Geosystems*, 15(8):3175–3189, 2014.

E. Kaminski and N. Ribe. A kinematic model for recrystallization and texture development in olivine polycrystals. *Earth and Planetary Science Letters*, 189(3):253–267, 2001.

E. Kaminski and N. M. Ribe. Timescales for the evolution of seismic anisotropy in mantle flow. *Geochemistry, Geophysics, Geosystems*, 3(8):1–17, 2002.

E. Kaminski, N. M. Ribe, and J. T. Browaeys. D-Rex, a program for calculation of seismic anisotropy due to crystal lattice preferred orientation in the convective upper mantle. *Geophysical Journal International*, 158(2):744–752, 2004.

S. Kaneshima, M. Ando, and S. Kimura. Evidence from shear-wave splitting for the restriction of seismic anisotropy to the upper crust. *Nature*, 335(6191):627, 1988.

S. Karato. Rheology of the deep upper mantle and its implications for the preservation of the continental roots: A review. *Tectonophysics*, 481(1-4):82–98, 2010.

S. Karato and P. Wu. Rheology of the upper mantle: a synthesis. *Science*, 260(5109): 771–778, 1993.

S.-i. Karato. Importance of anelasticity in the interpretation of seismic tomography. *Geophysical Research Letters*, 20(15):1623–1626, 1993.

J.-M. Kendall. Teleseismic arrivals at a mid-ocean ridge: Effects of mantle melt and anisotropy. *Geophysical Research Letters*, 21(4):301–304, 1994.

J.-M. Kendall and C. Lithgow-Bertelloni. Why is africa rifting? *Geological Society, London, Special Publications*, 420(1):11–30, 2016.

S. D. King and D. L. Anderson. An alternative mechanism of flood basalt formation. *Earth and Planetary Science Letters*, 136(3-4):269–279, 1995.

S. D. King and D. L. Anderson. Edge-driven convection. *Earth and Planetary Science Letters*, 160(3):289–296, 1998.

Á. Király, C. P. Conrad, and L. N. Hansen. Evolving viscous anisotropy in the upper mantle and its geodynamic implications. *Geochemistry, Geophysics, Geosystems*, 21(10): e2020GC009159, 2020.

A. Koptev, E. Burov, T. Gerya, L. Le Pourhiet, S. Leroy, E. Calais, and L. Jolivet. Plume-induced continental rifting and break-up in ultra-slow extension context: Insights from 3d numerical modeling. *Tectonophysics*, 746:121–137, 2018a.

A. Koptev, E. Calais, E. Burov, S. Leroy, and T. Gerya. Along-axis variations of rift width in a coupled lithosphere-mantle system, application to east africa. *Geophysical Research Letters*, 45(11):5362–5370, 2018b.

M. Kronbichler, T. Heister, and W. Bangerth. High accuracy mantle convection simulation through modern numerical methods. *Geophysical Journal International*, 191(1):12–29, 2012.

T. M. Kusky, E. Toraman, T. Raharimahefa, and C. Rasoazanamparany. Active tectonics of the Alaotra–Ankay Graben System, Madagascar: possible extension of Somalian–African diffusive plate boundary? *Gondwana Research*, 18(2):274–294, 2010.

N. Kusznir and R. Park. Intraplate lithosphere deformation and the strength of the lithosphere. *Geophysical Journal International*, 79(2):513–538, 1984.

C. H. Langmuir, E. M. Klein, and T. Plank. Petrological systematics of mid-ocean ridge basalts: Constraints on melt generation beneath ocean ridges. *Mantle flow and melt generation at mid-ocean ridges*, 71:183–280, 1992.

G. Laske, Z. Ma, G. Masters, and M. Pasyanos. Crust 1.0: a new global crustal model at 1× 1 degrees, 2013.

M. D. Long and T. W. Becker. Mantle dynamics and seismic anisotropy. *Earth and Planetary Science Letters*, 297(3):341–354, 2010.

J.-E. Martelat, J.-M. Lardeaux, C. Nicollet, and R. Rakotondrazafy. Strain pattern and late Precambrian deformation history in southern Madagascar. *Precambrian research*, 102(1): 1–20, 2000.

G. Maruyama and T. Hiraga. Grain-to multiple-grain-scale deformation processes during diffusion creep of forsterite+ diopside aggregate: 1. direct observations. *Journal of Geophysical Research: Solid Earth*, 122(8):5890–5915, 2017.

J. Meert and E. Tamrat. Paleomagnetic evidence for a stationary marion hotspot: additional paleomagnetic data from madagascar. *Gondwana Research*, 10(3-4):340–348, 2006.

W. Menke and V. Levin. The cross-convolution method for interpreting SKS splitting observations, with application to one and two-layer anisotropic earth models. *Geophysical Journal International*, 154(2):379–392, 2003.

L. Michon. The volcanism of the Comoros archipelago integrated at a regional scale. In *Active Volcanoes of the Southwest Indian Ocean*, pages 333–344. Springer, 2016.

T. Miyazaki, K. Sueyoshi, and T. Hiraga. Olivine crystals align during diffusion creep of Earth's upper mantle. *Nature*, 502(7471):321, 2013.

R. Montelli, G. Nolet, F. Dahlen, and G. Masters. A catalogue of deep mantle plumes: New results from finite-frequency tomography. *Geochemistry, Geophysics, Geosystems*, 7(11), 2006.

R. Moucha and A. M. Forte. Changes in African topography driven by mantle convection. *Nature Geoscience*, 4(10):707, 2011.

J. Naliboff, C. Lithgow-Bertelloni, L. Ruff, and N. de Koker. The effects of lithospheric thickness and density structure on earth s stress field. *Geophysical Journal International*, 188(1):1–17, 2012.

J. Naliboff, A. Glerum, S. Brune, G. Péron-Pinvidic, and T. Wrona. Development of 3-d rift heterogeneity through fault network evolution. *Geophysical Research Letters*, 47(13): e2019GL086611, 2020.

A. Nicolas and N. I. Christensen. Formation of anisotropy in upper mantle peridotites-a review. *Composition, structure and dynamics of the lithosphere-asthenosphere system*, 16 (eds Fuchs, K. Froidevaux, C.):111–123 (Am. Geo– phys. Un., Washington D.C., 1987), 1987.

C. Nicollet. Crustal evolution of the granulites of Madagascar. In *Granulites and crustal evolution*, pages 291–310. Springer, 1990.

O. Nishizawa and K. Kanagawa. Seismic velocity anisotropy of phyllosilicate-rich rocks: characteristics inferred from experimental and crack-model studies of biotite-rich schist. *Geophysical Journal International*, 182(1):375–388, 2010.

E. A. Njinju, E. A. Atekwana, D. S. Stamps, M. G. Abdelsalam, E. A. Atekwana, K. L. Mickus, S. Fishwick, F. Kolawole, T. A. Rajaonarison, and V. N. Nyalugwe. Lithospheric structure of the malawi rift: Implications for magma-poor rifting processes. *Tectonics*, 38 (11):3835–3853, 2019a.

E. A. Njinju, F. Kolawole, E. A. Atekwana, D. S. Stamps, E. A. Atekwana, M. G. Abdelsalam, and K. L. Mickus. Terrestrial heat flow in the malawi rifted zone, east africa: Implications for tectono-thermal inheritance in continental rift basins. *Journal of Volcanology and Geothermal Research*, 387:106656, 2019b.

A. A. Nyblade. Heat flow and the structure of precambrian lithosphere. In *Developments in Geotectonics*, volume 24, pages 81–91. Elsevier, 1999.

A. A. Nyblade and S. W. Robinson. The african superswell. *Geophysical research letters*, 21 (9):765–768, 1994.

T. J. O. H. G. J. R. Nyblade, A. and C. A. Langston. *Seismic evidence for a deep upper mantle thermal anomaly beneath East Africa*, 2000.

M. E. Pasyanos. *A lithospheric attenuation model of North America*, 2013.

J. D. Paul and C. M. Eakin. Mantle upwelling beneath madagascar: evidence from receiver function analysis and shear wave splitting. *Journal of Seismology*, 21(4):825–836, 2017.

J. Perry-Houts and L. Karlstrom. Anisotropic viscosity and time-evolving lithospheric instabilities due to aligned igneous intrusions. *Geophysical Journal International*, 216(2): 794–802, 2019.

N. S. Podolefsky, S. Zhong, and A. K. McNamara. The anisotropic and rheological structure of the oceanic upper mantle from a simple model of plate shear. *Geophysical Journal International*, 158(1):287–296, 2004.

M. J. Pratt, M. E. Wysession, G. Aleqabi, D. A. Wiens, A. A. Nyblade, P. Shore, G. Rambolamanana, F. Andriampenomanana, T. Rakotondraibe, R. D. Tucker, et al. Shear velocity structure of the crust and upper mantle of Madagascar derived from surface wave tomography. *Earth and Planetary Science Letters*, 458:405–417, 2017.

T. Raharimahefa and T. M. Kusky. Structural and remote sensing studies of the southern Betsimisaraka Suture, Madagascar. *Gondwana Research*, 10(1-2):186–197, 2006.

T. Raharimahefa and T. M. Kusky. Structural and remote sensing analysis of the Betsimisaraka Suture in northeastern Madagascar. *Gondwana Research*, 15(1):14–27, 2009.

T. A. Rajaonarison, D. S. Stamps, S. Fishwick, S. Brune, A. Glerum, and J. Hu. Numerical modeling of mantle flow beneath madagascar to constrain upper mantle rheology beneath continental regions. *Journal of Geophysical Research. Solid Earth*, 125(2):Art–No, 2020.

G. Rambolamanana, P. Suhadolc, and G. Panza. Simultaneous inversion of hypocentral parameters and structure velocity of the central region of Madagascar as a premise for the mitigation of seismic hazard in Antananarivo. *Pure and Applied Geophysics*, 149(4): 707–730, 1997.

C. Ramirez, A. Nyblade, M. E. Wysession, M. Pratt, F. Andriampenomanana, and T. Rako-

tondraibe. Complex seismic anisotropy in Madagascar revealed by shear wave splitting measurements. *Geophysical Journal International*, 215(3):1718–1727, 2018.

T. Ramsay and R. Pysklywec. Anomalous bathymetry, 3D edge driven convection, and dynamic topography at the western Atlantic passive margin. *Journal of Geodynamics*, 52 (1):45–56, 2011.

M. Reiss, G. Rümpker, F. Tilmann, X. Yuan, J. Giese, and E. Rindraharisaona. Seismic anisotropy of the lithosphere and asthenosphere beneath southern Madagascar from teleseismic shear wave splitting analysis and waveform modeling. *Journal of Geophysical Research: Solid Earth*, 121(9):6627–6643, 2016.

N. M. Ribe. On the relation between seismic anisotropy and finite strain. *Journal of Geophysical Research: Solid Earth*, 97(B6):8737–8747, 1992.

N. M. Ribe and Y. Yu. A theory for plastic deformation and textural evolution of olivine polycrystals. *Journal of Geophysical Research: Solid Earth*, 96(B5):8325–8335, 1991.

E. J. Rindraharisaona, M. Guidarelli, A. Aoudia, and G. Rambolamanana. Earth structure and instrumental seismicity of Madagascar: Implications on the seismotectonics. *Tectonophysics*, 594:165–181, 2013.

J. Ritsema, H. J. van Heijst, and J. H. Woodhouse. Complex shear wave velocity structure imaged beneath africa and iceland. *Science*, 286(5446):1925–1928, 1999.

T. O. Rooney, C. Herzberg, and I. D. Bastow. Elevated mantle temperature beneath east africa. *Geology*, 40(1):27–30, 2012.

I. Rose, B. Buffett, and T. Heister. Stability and accuracy of free surface time integration in viscous flows. *Physics of the Earth and Planetary Interiors*, 262:90 – 100, 2017. ISSN

0031-9201. doi: 10.1016/j.pepi.2016.11.007. URL http://dx.doi.org/10.1016/j.pepi.2016.11.007.

E. Saria, E. Calais, D. Stamps, D. Delvaux, and C. Hartnady. Present-day kinematics of the east african rift. *Journal of Geophysical Research: Solid Earth*, 119(4):3584–3600, 2014.

M. Savage. Seismic anisotropy and mantle deformation: what have we learned from shear wave splitting? *Reviews of Geophysics*, 37(1):65–106, 1999.

J.-R. Scholz, G. Barruol, F. R. Fontaine, A. Mazzullo, J.-P. Montagner, E. Stutzmann, L. Michon, and K. Sigloch. SKS splitting in the Western Indian Ocean from land and seafloor seismometers: Plume, plate and ridge signatures. *Earth and Planetary Science Letters*, 498:169–184, 2018.

G. Schreurs, J. Giese, A. Berger, and E. Gnos. A new perspective on the significance of the Ranotsara Shear Zone in Madagascar. *International Journal of Earth Sciences*, 99(8): 1827–1847, 2010.

B. Schuberth, H.-P. Bunge, G. Steinle-Neumann, C. Moder, and J. Oeser. Thermal versus elastic heterogeneity in high-resolution mantle circulation models with pyrolite composition: High plume excess temperatures in the lowermost mantle. *Geochemistry, Geophysics, Geosystems*, 10(1), 2009.

D. Seward, D. Grujic, and G. Schreurs. An insight into the breakup of Gondwana: Identifying events through low–temperature thermochronology from the basement rocks of Madagascar. *Tectonics*, 23(3), 2004.

P. G. Silver. Seismic anisotropy beneath the continents: Probing the depths of geology. *Annual review of earth and planetary sciences*, 24(1):385–432, 1996.

P. G. Silver and W. W. Chan. Implications for continental structure and evolution from seismic anisotropy. *Nature*, 335(6185):34, 1988.

P. G. Silver and W. W. Chan. Shear wave splitting and subcontinental mantle deformation. *Journal of Geophysical Research: Solid Earth*, 96(B10):16429–16454, 1991.

N. A. Simmons, A. M. Forte, and S. P. Grand. Thermochemical structure and dynamics of the african superplume. *Geophysical Research Letters*, 34(2), 2007.

N. A. Simmons, A. M. Forte, and S. P. Grand. Joint seismic, geodynamic and mineral physical constraints on three-dimensional mantle heterogeneity: Implications for the relative importance of thermal versus compositional heterogeneity. *Geophysical Journal International*, 177(3):1284–1304, 2009.

D. Stamps, L. Flesch, E. Calais, and A. Ghosh. Current kinematics and dynamics of africa and the east african rift system. *Journal of Geophysical Research: Solid Earth*, 119(6): 5161–5186, 2014.

D. Stamps, G. Iaffaldano, and E. Calais. Role of mantle flow in nubia-somalia plate divergence. *Geophysical Research Letters*, 42(2):290–296, 2015.

D. Stamps, C. Kreemer, R. Fernandes, T. Rajaonarison, and G. Rambolamanana. Redefining east african rift system kinematics. *Geology*, 2020.

D. S. Stamps, E. Saria, and C. Kreemer. A geodetic strain rate model for the east african rift system. *Scientific reports*, 8(1):1–8, 2018.

B. Steinberger, E. Bredow, S. Lebedev, A. Schaeffer, and T. H. Torsvik. Widespread volcanism in the Greenland–North Atlantic region explained by the iceland plume. *Nature Geoscience*, 12(1):61, 2019.

L. Stixrude and C. Lithgow-Bertelloni. Influence of phase transformations on lateral heterogeneity and dynamics in Earth's mantle. *Earth and Planetary Science Letters*, 263(1-2): 45–55, 2007.

P. R. Stoddard and D. Abbott. Influence of the tectosphere upon plate motion. *Journal of Geophysical Research: Solid Earth*, 101(B3):5425–5433, 1996.

X. Tian and M. Santosh. Fossilized lithospheric deformation revealed by teleseismic shear wave splitting in eastern china. *GSA Today*, 25(2):4–10, 2015.

R. Tucker, S. Peters, J. Roig, H. Théveniaut, and C. Delor. Notice explicative des cartes géologique et métallogéniques de la république de Madagascar à 1/1,000,000. *Ministère des Mines, PGRM, Antananarivo, République de Madagascar*, 2012.

K. T. Walker, A. A. Nyblade, S. L. Klemperer, G. H. Bokelmann, and T. J. Owens. On the relationship between extension and anisotropy: Constraints from shear wave splitting across the east african plateau. *Journal of Geophysical Research: Solid Earth*, 109(B8), 2004.

J. D. West, M. J. Fouch, J. B. Roth, and L. T. Elkins-Tanton. Vertical mantle flow associated with a lithospheric drip beneath the great basin. *Nature Geoscience*, 2(6):439, 2009.

J. Wheeler. The preservation of seismic anisotropy in the Earth's mantle during diffusion creep. *Geophysical Journal International*, 178(3):1723–1732, 2009.

B. Windley, A. Razafiniparany, T. Razakamanana, and D. Ackermand. Tectonic framework of the Precambrian of Madagascar and its Gondwana connections: a review and reappraisal. *Geologische Rundschau*, 83(3):642–659, 1994.

S. Zhang and S. Karato. Lattice preferred orientation of olivine aggregates deformed in simple shear. *Nature*, 375(6534):774, 1995.

S. Zhang and C. O'Neill. The early geodynamic evolution of Mars-type planets. *Icarus*, 265: 187–208, 2016.

S. Zhong. Role of ocean-continent contrast and continental keels on plate motion, net rotation of lithosphere, and the geoid. *Journal of Geophysical Research: Solid Earth*, 106(B1):703–712, 2001.

Appendices

Appendix A

Governing Equations: Stokes System

Using ASPECT, We solve for velocity u and pressure p following the Boussinessq approximation for an incompressible fluid, where the equations for conservation of momentum and mass (e.g., Stokes equations) are:

$$-\nabla \cdot [2\eta\, \varepsilon(u)] + \nabla p = -\alpha \rho T \mathbf{g} \tag{A.1}$$

$$\nabla \cdot \mathbf{u} = 0 \tag{A.2}$$

Where $\mathbf{u}$ is the velocity, $\varepsilon(\mathbf{u})$ is the symmetric gradient of velocity, η is the viscosity, ρ is the density, p the pressure, and g is the gravitational acceleration. Parameters for the simulation are summarized in Table 1. Note that the density does not appear in the mass conservation Equation 1 because in the Boussinesq approximation the density is considered constant in all occurrences in the equations with the exception of the buoyancy term on the right hand side of E quation 1.

The sub-lithospheric mantle density in our simulations varies linearly with temperature:

$$\rho = \rho_0(1 - \alpha(T - T_0) \tag{A.3}$$

Where ρ_0 is the reference material density, α is the coefficient of thermal expansion and

Table A.1: Thermodynamic Material Properties in the Numerical Simulations

Parameter	Symbol	Value	Units
Mantle reference density	ρ_0	3300	$kg.m^{-3}$
Thermal conductivity	κ	3	$W.m^{-1}.K^{-1}$
Specific heat capacity	C_p	1250	$J.kg^{-1}.K^{-1}$
Intrinsic specific heat production	H	7.4×10^{-12}	$W.kg^{-1}$
Thermal expansion coefficient	α	2×10^{-5}	K^{-1}
Gravitation acceleration (radial constant)	g	9.8	$m.s^{-2}$
Reference temperature	T_0	298	K

T_0 is the temperature. While we also solve for the advection and diffusion of temperature and composition in our simulations, the initial time step only uses the temperature and compositional structure defined through the initial conditions. As a result, the solution of the advection-diffusion equation has no impact on our results as we only consider instantaneous deformation.

Appendix B

Calculating Temperature and Viscosity Field

B.1 Calculating Conductive Lithospheric Geothermal Gradients

The initial temperature structure throughout the lithosphere is calculated following the approach of Chapman (1986), which uses an analytical solution for a conductive geothermal profile to obtain temperatures throughout a layered lithosphere (upper crust, middle crust, lower crust, and mantle lithosphere). A key assumption to this approach is that each layer contains a constant and unique thermal conductivity and radiogenic heat production (Table 1). While the lithosphere-asthenosphere boundary is defined as an isotherm (1673 K), the main constraints on the lithospheric geothermal gradient are the surface heat flow, the lithospheric thickness, and the crustal thickness. The temperature $T_i(z)$ in the ith layer is given by:

$$T_i(z) = T_{i-1} + \frac{q_{i-1}z}{\kappa_i} - \frac{A_i z^2}{2\kappa_i} \tag{B.1}$$

$$q_i = q_{i-1} + A_i \Delta z_i \tag{B.2}$$

Table B.1: Lithospheric geothermal gradient parameters.

Parameter	Symbol	Craton	Mobile belts	Rifts	Units
Middle crust heat production	A	0.4×10^{-6}	0.4×10^{-6}	0.4×10^{-6}	$W.m^{-3}$
Lower crust heat production	A	0.2×10^{-6}	0.4×10^{-6}	0.4×10^{-6}	$W.m^{-3}$
Mantle lithosphere heat production	A	0.1×10^{-6}	0.1×10^{-6}	0.1×10^{-6}	$W.m^{-3}$
Surface heat flow	q	40	63	80	$W.m^{-2}$
Thermal conductivity	κ	3	3	3	$W.m^{-1}.K^{-1}$
Lithospheric thickness	-	150	100	$90^a - 70^b$	km
Crustal thickness	-	CRUST1.0	CRUST1.0	CRUST1.0	km

where T_{i-1} and q_{i-1} are the temperature and heat flow at the top of the layer. A_i and K_i are the heat production and thermal conductivity within the layer. Z is the depth measured positive from the surface. ΔZ_i is the thickness of each layer. q_i is the heat flow at the bottom of each layer. The temperature $T_i(z)$ is a function of depth and is calculated consecutively from the top layer (i.e. the upper crust) to the base of the lithosphere, using a surface temperature of 273 K and surface heat flow q_0, which varies laterally across the EAR (e.g. Njinju et al., 2019b; Nyblade and Langston, 2000). We constrain the surface heat flow in continental domains using regionally averaged values over the key tectonic regions based on terrestrial heat flow measurements reported by Nyblade (1999) and Nyblade (1997): mean heat flow of 40 mW/m^2 (4 mW/m^2 standard deviation) within the Tanzania Craton and the Congo Craton that is applied to all cratonic regions, mean heat flow of 64 mW/m2 (4 mW/m2 standard deviation) for the mobile belts, and 101 mW/m2 (20 mW/m2 standard deviation) for the rifts. The surface heat flow across the rifts may contain contributions from local hydrothermal circulation to the heat flow, therefore, we use the lower bound of 80 mW/m2. Parameters for the continental lithospheric geothermal gradient calculation in the simulation are summarized Table B.1. Figure B.1a-c show geothermal gradients defined for cratons (150 km), mobile belts between cratons and rifts (100 km), and rift domains (70 km), respectively. Outside of our main study area, we impose 80 mW/m2 at oceanic ridges and 64 mW/m2 for the rest of the oceanic lithosphere.

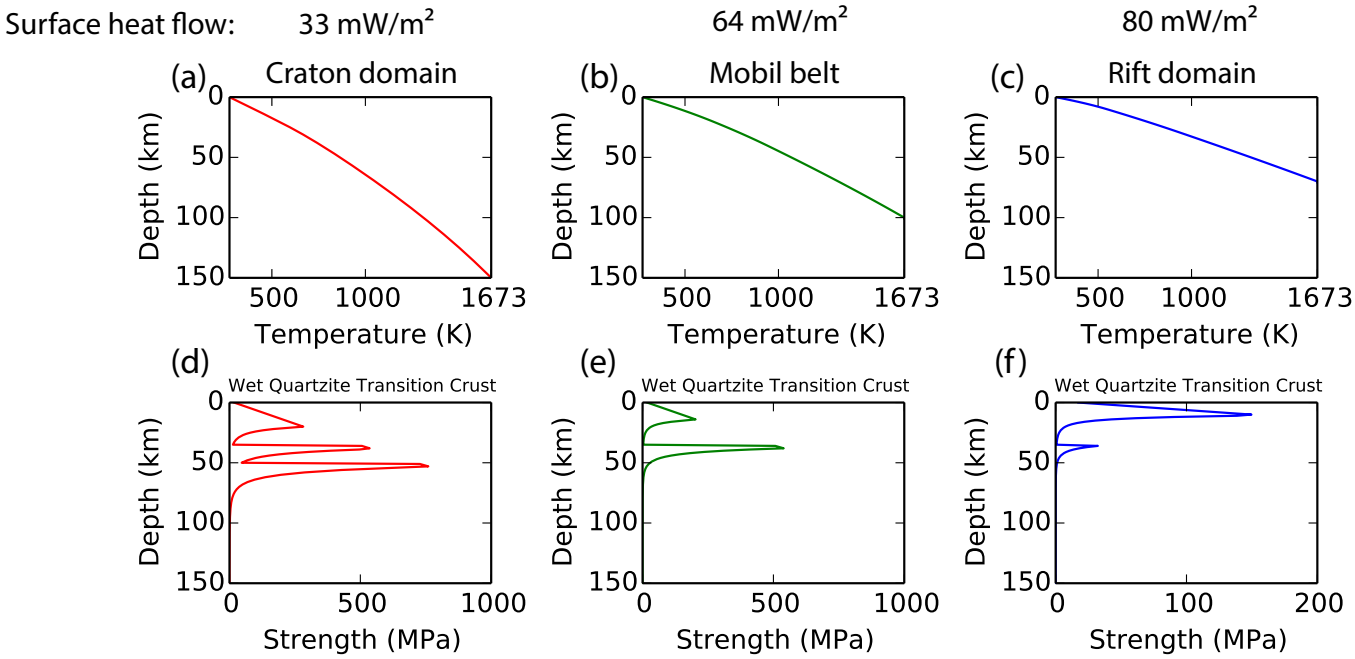

Figure B.1: Depth profile of geothermal gradients and strengths from different domain with varying lithospheric thicknesses: (a, b, c) geothermal gradients beneath craton (150 km), transition (100 km) and rift domains (70 km) assuming surface heat flow of 40 mW/m^2, 64 mW/m^2, and 80 mW/m^2, respectively. The lithosphere asthenosphere boundary is an isotherm 1673 K . (d, e ,f) strength profile profile beneath craton, transition and rift domains, respectively, assuming wet quartzite composition for the crust. All strength profiles are calculated with uniform 10^{-15} s^{-1}.

B.2 Calculating Rheology of the Lithosphere and Asthenosphere

The numerical experiments incorporate non-linear (non-Newtonian) rheological flow laws, which are needed to match first-order observations of solid Earth deformation and constraints from rock deformation experiments. In brittle (cold regions) of the crust and uppermost mantle, plasticity limits the stress and reduces viscosity, which is in accordance with a Drucker-Prager yield criterion (Alejano and Bobet, 2012; Glerum et al., 2018b). The viscous flow law for the crust is visco-plastic and dislocation creep for the mantle lithosphere. The crustal thickness and density are constrained by CRUST1.0. We assume that the dominant composition of the mantle is dry olivine, where the flow in the sub-lithospheric mantle is governed by composite rheology (Jadamec and Billen, 2010), which is a harmonic average of viscosity from diffusion creep and dislocation creep. The composite viscosity is given by:

$$\begin{aligned} \eta_{diff,disl} &= \frac{1}{2} A^{-\frac{1}{n}} d^{\frac{m}{n}} \dot{\epsilon}^{\frac{1-n}{n}} exp\left(\frac{E_a + V_a P}{nRT}\right) \\ \eta_{comp} &= \frac{\eta_{diff}\eta_{disl}}{\eta_{diff} + \eta_{disl}} \end{aligned}$$

η_{diff} and η_{disl} are the viscosity for diffusion creep and dislocation creep respectively. $\dot{\epsilon}$ is the square root of the second invariant of the strain rate tensor, T is the temperature, P is the pressure. E_a is activation energy, V_a is activation volume, n and m are respectively the stress and grain size exponents, A is pre-exponent factor and R is the gas constant. The parameters A, E_a, V_a, n and m are obtained from experimental studies of the olivine mineral from Hirth and Kohlstedt (2003). Brittle failure for the crust limits viscous strength through

a Drucker-Prager yield criterion (Alejano and Bobet, 2012):

$$\sigma_{yield} = P \sin \phi + C \cos(\phi)$$

where is the ϕ angle of internal friction and C is the material cohesion. If the effective brittle stress is larger than the viscous effective stress, the viscosity is reduced so that the two stresses are equal. All parameters for viscosity calculations are given in Table B.2. We evaluate continental geothermal gradients and strengths from different lithospheric thicknesses domains (Figure B.1c-d) because regions with relatively thick lithosphere with have colder geothermal gradients and relatively strong rheology while regions with thinner lithosphere have higher geothermal gradient and weaker lithosphere. We expect that most deformation is localized at regions where the lithosphere are relatively weak i.e. in the rift.

Table B.2: Parameters used for the viscosity flow law of the sublithospheric mantle for dry olivine.

Parameter	Symbol	Crust Viscoplastic (Wet Quartzite)			Mantle Dislocation creep (Dry olivine)	Mantle Diffusion creep (Dry olivine)	Units
		Upper	Middle	Lower			
Grain size	d	-	-	-	-	10×10^{3}	μm
Grain size exponent	m	-	-	-	-	3	-
Stress exponent	n	4	4	3	3.5	1.0	-
Activation energy	E_a	223×10^{3}	223×10^{3}	345×10^{3}	530×10^{3}	375×10^{3}	$J.mol^{-1}$
Activation volume	V_a	0	0	0	18×10^{-6}	6×10^{-6}	$m^3.mol^{-1}$
Prefactor	A	8.574×10^{-28}	8.574×10^{-28}	7.130×10^{-18}	6.52×10^{-16}	1.5×10^{-15}	-
Reference Strain rate	$\dot{\epsilon}$	10^{-15}	10^{-15}	10^{-15}	10^{-15}	10^{-15}	s^{-1}
Angle internal friction	ϕ	30	30	30	-	-	$^{\circ}$
Cohesion	C	20×10^{6}	20×10^{6}	20×10^{6}	-	-	Pa